The Fractional Quantum Anomalous Hall Effect in Twisted MoTe2

Heonjoon Park

A dissertation
submitted in partial fulfillment of the
requirements for the degree of

Doctor of Philosophy

University of Washington

2025

Reading Committee:

Xiaodong Xu, Chair

David Cobden

Matthew Yankowitz

Program Authorized to Offer Degree:
Physics

University of Washington

Abstract

The Fractional Quantum Anomalous Hall Effect
in Twisted MoTe2

Heonjoon Park

Chair of the Supervisory Committee:
Xiaodong Xu
Department of Physics

Emergent quantum phenomena in two-dimensional moiré superlattices, particularly twisted bilayer $MoTe_2$ ($tMoTe_2$), reveals a rich interplay between electronic correlations and band topology. Leveraging device fabrication, optical spectroscopy, local imaging techniques, and low-temperature electrical transport measurements, we have experimentally demonstrated robust integer and fractional quantum anomalous Hall (QAH) states without external magnetic fields. Fractionally quantized Hall conductance plateaus at fillings such as $\nu = -2/3$ and $-3/5$, accompanied by vanishing longitudinal resistance, provide definitive evidence for fractional Chern insulating (FCI) phases driven purely by electron-electron interactions. Additionally, local visualization of fractional edge states through microwave impedance microscopy has directly confirmed bulk-edge correspondence. Further exploration into higher Chern bands and dissipationless transport has expanded understanding of correlation-driven phenomena, uncovering potential pathways to non-Abelian fractional states relevant for quantum computing. These results collectively establish twisted $MoTe_2$ as an exceptional platform for exploring novel quantum states and highlight their potential for future topological quantum technologies.

TABLE OF CONTENTS

LIST OF FIGURES

GLOSSARY

ANYONIC STATISTICS: Quantum statistics describing particle-like excitations that differ from fermions and bosons, characterized by nontrivial phase factors acquired upon particle exchange, prevalent in fractional quantum Hall states.

CHERN NUMBER: An integer topological invariant representing the integral of the Berry curvature over the Brillouin zone, crucial for classifying quantum Hall and anomalous Hall states.

COMPOSITE FERMION: Quasiparticles formed from electrons bound to magnetic flux quanta, fundamental in describing fractional quantum Hall states.

DISSIPATIONLESS TRANSPORT: Electronic transport without energy loss, characterized by quantized Hall resistance and vanishing longitudinal resistance, hallmark of topological states.

EXCITON: A bound state of an electron-hole pair within semiconductors.

FRACTIONAL CHERN INSULATOR (FCI): A lattice-based analog of the fractional quantum Hall effect occurring in flat bands without an external magnetic field, arising from strong electron-electron interactions and topology.

FRACTIONAL QUANTUM ANOMALOUS HALL (FQAH) EFFECT: A phenomenon exhibiting fractional quantization of Hall resistance at zero external magnetic field, arising spontaneously from electron correlation and intrinsic band topology.

FRACTIONAL QUANTUM HALL (FQH) EFFECT: Quantum Hall states occurring at fractional Landau-level fillings, characterized by fractionalized excitations and quantized Hall conductance due to electron-electron correlations.

HARTREE-FOCK APPROXIMATION: An approximation method in quantum mechanics for solving many-body problems, frequently utilized to model electron interactions in moiré superlattices.

INTEGER QUANTUM ANOMALOUS HALL (QAH) EFFECT: Quantized Hall conductance states occurring at integer fillings without an external magnetic field, enabled by spontaneous magnetization and intrinsic topological band structures.

LANDAU LEVEL: Discrete energy levels formed by electrons confined in a two-dimensional system subjected to a perpendicular magnetic field, separated by the cyclotron energy.

LAUGHLIN WAVEFUNCTION: A trial wavefunction proposed by Robert Laughlin that accurately describes the fractional quantum Hall state at specific fractional fillings.

MOIRÉ PATTERN: Long-range interference patterns created when two periodic lattices are overlaid at slight rotational or lattice mismatch angles, resulting in superlattice potentials.

QUANTUM CAPACITANCE: Capacitance contributions arising from changes in electronic states at the Fermi level, providing insight into electronic correlations and density of states.

REFLECTIVE MAGNETIC CIRCULAR DICHROISM (RMCD): Optical spectroscopy method measuring differences in reflectance of circularly polarized light to probe magnetic properties.

STREDA FORMULA: A relation connecting Hall conductance to electron density and magnetic flux, used to determine topological invariants (Chern numbers) experimentally.

TOPOLOGICAL INSULATOR: Materials characterized by insulating bulk states and conducting edge or surface states protected by time-reversal symmetry and band topology.

TWISTRONICS: A research area focused on tuning electronic properties of layered materials through twist-angle-induced moiré superlattices, giving rise to novel correlated and topological phases.

ACKNOWLEDGMENTS

Joining the University of Washington to work with my advisor, Xiaodong Xu, was the best decision of my life. I owe my deepest gratitude to Xiaodong for his mentorship and support over the past five years. I first met him during my Ph.D. interview in the winter of 2020. At the time, I was uncertain about the long-term prospects of the field and hesitantly asked, "How long do you think this wave of 2D materials will last?" His response—"We're here to make waves, not ride them"—captured his pioneering spirit and unwavering conviction. That moment was decisive and it inspired me to join his group.

Throughout my Ph.D., Xiaodong has been a constant source of support, energy, and ideas. In the face of setbacks—when the twentieth device in a row failed, during grueling month-long 12-hour night shifts babysitting the cryostat, or amid deadline crunches and uncertainty—he had an almost superhuman ability to cut through the noise and identify the essential physics. He reminded me, again and again, of what mattered most. Under his mentorship, I began to internalize a fundamental question: What is the most important problem in our field? Xiaodong is the person I most look up to, and hope to emulate in my future.

I am deeply grateful to Jiaqi Cai—a brilliant collaborator, mentor, and friend. His intellectual depth, wide-ranging curiosity, and rare ability to grasp the core of a problem while remaining meticulous with instrumentation have always inspired me. Some of my most cherished memories are the late nights we spent discussing physics, philosophy, and life. His absence has been felt deeply ever since he left. I wish you continued success at MIT and beyond.

Eric Anderson—thank you for the late-night conversations (often with Jiaqi), full of depth and spontaneity. Your conscientious nature and thoughtful reflections, whether on science, coffee, literature, or art, were a breath of fresh air. I know you'll bring that same passion and vigor to your next chapter in France.

One of UW's greatest strengths is its collaborative spirit. I am thankful to the many faculty and

colleagues who have made this ecosystem so special. Dave Cobden, thank you for your mentorship and for always offering your honest advice—whether scientific or personal. Your guidance has shaped my path, and I hope to walk a trajectory similar to the one you've traced. Matt Yankowitz, I've always appreciated the stimulating physics discussions and the support that you've offered during my Ph.D. Di Xiao, your support—both as a theorist and as a friend—has been deeply appreciated. Your heartfelt humor and insightful guidance were always grounding. Ting Cao, I'm grateful for your candid advice and sharp insight. I've always admired your clarity of thought, and I hope to carry that standard forward.

In my early days learning optics, I was fortunate to be guided by many senior members of the lab. Kyle—learning optical measurements alongside you was a joy, and your judgment shaped the way I think as an experimentalist. The camaraderie we shared during dinners and late-night conversations sustained me through many challenging stretches. I hope our paths cross again in the Bay Area. John Cenker—your creative problem-solving and spirited approach left a lasting impression. Paul- thank you for all the initial training and collaborative work. You are truly one of the pillars that hold this ecosystem together. Xi—your discipline and work ethic set a standard in the lab that I continually aspired to meet. Yingqi—I remain deeply grateful for the long shifts we worked together and for the knowledge you shared on pressure measurements. Though time has flown, those days remain among my most cherished memories. Minhao—I owe most of my fabrication skills to you; your quiet resilience was a steady source of inspiration. Jiayi—your ever-smiling presence brightened the lab, and your ability to find humor in any situation lifted everyone's spirits.

I am also thankful to Zaiyao Fei, Dmitry Ovchinnikov, Geoffrey Diederich, Tiancheng Song, Jordan Fonseca, and Yinong Zhang for the physics discussions, encouragement, and life lessons we shared along the way.

To those who will carry the Xu Lab forward—I wish you the greatest success in your own journeys. Weijie—you are one of the kindest and most responsible people I have ever met. Your willingness to help others, your openness in discussion, and your remarkable resilience in adversity will carry you far. Yi-Fan—your work ethic has set a high bar, and your rapid growth since joining

the lab has been remarkable. I have no doubt that good fortune will find you soon. Shuai—your deep knowledge of instrumentation has been a cornerstone of the lab's success. James—though our time together was brief, the discussions and ideas we shared were precious to me. I have no doubt you will thrive. Godspeed. Chaowei—I have always been grateful for the beautiful crystals you grew for us; without them, much of the work in this thesis would not have been possible. Mai—you brought both a cheerful spirit to the lab and a sharp intellect, impressive linguistic talent, and vibrant energy. I will certainly miss your love for cats and will do my best to keep my promise when I'm at Stanford.

I was also fortunate to work with Courtney Baier, Jack Barlow, Ren Pumulo, Dhan Bautista, Julian Stewart, Essance Ray, and Christiano Beach—thank you all.

To my family—you are the reason I never gave up, even when the path felt impossible. Mom—your spirit, work ethic, and guidance have shaped every part of who I am. How you raised me, I still cannot fully comprehend; but thanks to you, I have the courage to follow what I believe in. Dad—your level-headed, realistic advice has been an anchor in my life, and I know you will always be there, no matter the circumstances. My sister—looking back, the moments we shared growing up have become some of my dearest memories. Now that we've grown, I wish you a life filled with happiness and fulfillment.

Most of all, I thank my wife, Yeajee. I am blessed beyond measure to have shared over eleven years with you, despite seven of them being across a great distance. Through my darkest and most difficult moments, you never wavered. I promise to stand by you—until the day I take my last breath. Thank you.

DEDICATION

to my wife, Yeajee

Chapter 1

INTRODUCTION

1.1 Pillars of Modern Condensed Matter Physics

Over the past several decades, condensed matter physics has evolved from a discipline focused primarily on classifying crystalline solids into a vast and interconnected field that explores the emergent properties of quantum matter. This evolution has been driven by several overarching themes—conceptual "pillars"—that not only define the modern research landscape but also guide the search for new materials and phenomena. Among these, a few of the most influential for current frontiers are *band topology*, *strong electronic correlations*, *magnetism*, and *superconductivity* [1, 2].

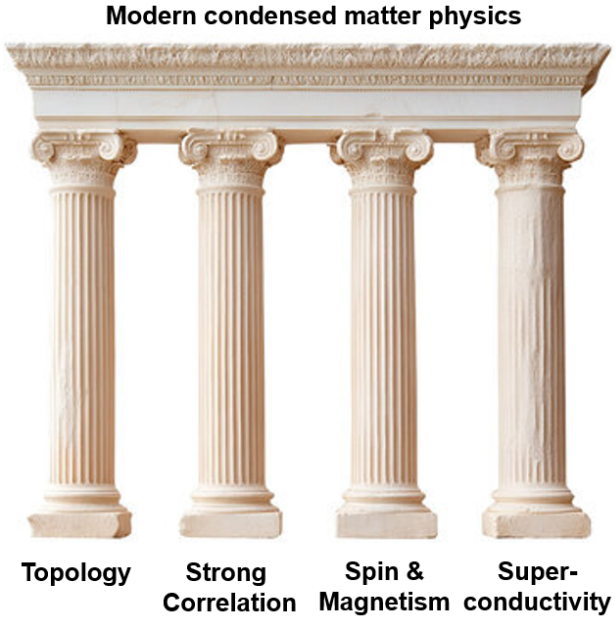

Figure 1.1: Pillars of modern condensed matter physics

Topology: Geometry in Quantum Bands

Topological phases of matter represent a profound shift in the way we classify materials. Unlike conventional phases, which are distinguished by local order parameters and symmetry breaking, topological phases are characterized by global, quantized invariants that remain unchanged under continuous deformations of the system's parameters [3, 4]. This invariance is akin to the genus of a surface in mathematics: a coffee mug and a donut share a genus of one because each has a single hole, and no smooth transformation can change this number without tearing the surface. In a crystalline solid, the equivalent "holes" reside not in real space but in the momentum-space structure of the electronic wave functions, encoded in the Berry curvature and related geometrical quantities of the energy bands. These topological characteristics give rise to robust physical responses—such as quantized Hall conductance—that are immune to weak disorder or local perturbations.

Strong Correlations and Emergence

While topology captures global constraints on the wave function, strong electron–electron interactions add another layer of complexity. In many quantum materials, the Coulomb interaction energy can rival or exceed the kinetic energy scale, forcing electrons to move in a highly correlated fashion. When the number of interacting electrons approaches Avogadro's number, the system's collective behavior can no longer be deduced from the properties of individual particles. This phenomenon, known as *emergence*, produces rich many-body states such as Mott insulators, unconventional superconductors, and fractional quantum Hall liquids [5, 6].

Magnetism and Its Quantum Origins

Magnetism is a particularly striking example of correlation-driven order. While ferromagnetism in elemental metals like iron can be partially understood within a semiclassical framework, many magnetic phenomena—especially those arising in low-dimensional systems—require a fully quantum-mechanical description [7]. In two-dimensional materials, the discovery of intrinsic magnetism [8, 9] has reinvigorated this field, enabling studies of spin physics, magnetic anisotropy, and coupling to topological band structures in a clean and highly tunable setting.

The most exciting frontier emerges when these pillars intersect. Quantum materials in which strong correlations coexist with nontrivial band topology can host unconventional states such as fractional Chern insulators (FCIs), correlated Chern ferromagnets, and interaction-driven topological superconductors. Realizing such phases typically requires stringent material conditions: nearly flat electronic bands to enhance correlations, topological band character to enable quantized responses, and broken time-reversal symmetry to produce chiral edge modes. Few natural materials meet all these criteria simultaneously.

A breakthrough came with the development of moiré superlattices in two-dimensional (2D) van der Waals heterostructures [10]. By stacking two atomically thin layers with a small relative twist, one can engineer electronic minibands with controllable flatness, topology, and interaction strength. In particular, twisted transition-metal dichalcogenides (TMDs) have emerged as an exceptionally versatile platform, offering access to strongly correlated, topologically nontrivial, and magnetic regimes within the same device. This tunability has opened the door to experimental realizations of the fractional quantum anomalous Hall (FQAH) effect—a zero-field analog of the fractional quantum Hall effect driven entirely by band topology and electron interactions [11, 12, 13, 14].

This thesis explores these intertwined domains in the context of twisted bilayer $MoTe_2$, a moiré TMD system that unites flat-band physics, topological band structure, and interaction-driven magnetism in a single material platform. Leveraging state-of-the-art nanofabrication, optical spectroscopy, and cryogenic transport techniques, the work builds on recent advances demonstrating integer and fractional quantum anomalous Hall states, real-space imaging of chiral edge channels, and dissipationless transport in fractional Chern insulators. By investigating the mechanisms, stability, and tunability of these phases, this study aims to deepen our understanding of how the foundational pillars of condensed matter physics converge to create new states of quantum matter.

1.2 The Integer Quantum Hall Effect

The discovery of the integer quantum Hall effect (IQHE) in 1980 by von Klitzing [15] marked a paradigm shift in condensed matter physics, providing the first clear demonstration that topological concepts—previously confined to abstract mathematics—could dictate measurable electronic transport properties. In the IQHE, the Hall conductance is quantized in integer multiples of e^2/h, with the integer corresponding to a topological invariant known as the first Chern number. This

quantization is remarkably precise, insensitive to microscopic disorder, and has since become a metrological standard for resistance.

The effect was first observed in a high-mobility two-dimensional electron gas (2DEG) at cryogenic temperatures under a strong perpendicular magnetic field. Classically, an electron in such a field undergoes cyclotron motion with frequency $\omega_c = eB/m^*$, where m^* is the effective mass, and a corresponding length scale known as the magnetic length,

$$\ell_B = \sqrt{\frac{\hbar}{eB}}. \tag{1.1}$$

Quantum mechanically, this motion leads to the formation of highly degenerate, perfectly flat energy levels—the Landau levels—given by

$$E_n = \hbar\omega_c \left(n + \frac{1}{2}\right), \quad n \in \mathbb{Z}_{\geq 0}. \tag{1.2}$$

Because each Landau level accommodates a fixed number of states proportional to the applied magnetic flux, tuning the electron density relative to this degeneracy leads to a sequence of gapped, incompressible ground states.

In a finite sample, the story changes near the boundaries. While electrons in the bulk execute closed cyclotron orbits, electrons near the edge cannot complete these loops and instead follow *skipping orbits*—semiclassical trajectories that drift unidirectionally along the sample edge. This physical picture underpins the concept of *bulk–boundary correspondence*: the gapped bulk is topologically nontrivial, and the gapless edge modes are a direct consequence of that topology [16]. These chiral edge channels are immune to backscattering in the absence of processes that connect opposite edges, leading to dissipationless transport.

Experimentally, the IQHE manifests as a vanishing longitudinal conductance $\sigma_{xx} \to 0$ and quantized Hall conductance

$$\sigma_{xy} = \nu \frac{e^2}{h}, \quad \nu \in \mathbb{Z}, \tag{1.3}$$

where ν is the filling factor. At first glance, the conductance tensor

$$\hat{\sigma} = \begin{pmatrix} 0 & \nu e^2/h \\ -\nu e^2/h & 0 \end{pmatrix} \tag{1.4}$$

describes a perfect bulk insulator. However, converting to resistivity via $\hat{\rho} = \hat{\sigma}^{-1}$ yields $R_{xx} = 0$, characteristic of a perfect conductor. The resolution lies in the fact that the *bulk* is indeed

incompressible and insulating, but all current is carried by the *edge* in perfectly conducting chiral channels.

The link to topology was formalized by Thouless, Kohmoto, Nightingale, and den Nijs (TKNN) [17], who showed that the Hall conductance is proportional to an integer-valued invariant—the first Chern number—of the filled electronic bands:

$$\sigma_{xy} = C\frac{e^2}{h}, \quad C = \frac{1}{2\pi}\int_{\mathrm{BZ}} \Omega(\mathbf{k})\, d^2k, \tag{1.5}$$

where $\Omega(\mathbf{k})$ is the Berry curvature in momentum space and the integral runs over the Brillouin zone (BZ). Crucially, C depends only on the global topology of the Bloch wave functions and not on microscopic details. This explains why the quantization is so robust: small perturbations cannot change C unless the bulk gap closes.

1.3 Haldane and Kane-Mele model

The TKNN formalism makes no explicit reference to magnetic fields or Landau levels, suggesting that topology-driven Hall conductance might be realizable without an external B-field. Motivated by this, Haldane proposed a seminal lattice model [18] on a honeycomb lattice of spinless fermions, incorporating real nearest-neighbor hopping t and complex next-nearest-neighbor hopping $t_2 e^{\pm i\phi}$. This pattern of hoppings breaks time-reversal symmetry (via the phase ϕ) and sublattice symmetry, generating a topological band gap characterized by a nonzero Chern number. When the parameters are tuned such that the gap closes and reopens at one Dirac point, chiral edge states emerge, realizing a *Chern insulator*—a quantum anomalous Hall state without Landau levels.

Implementing the Haldane model in real materials proved challenging. The first experimental observation of the quantum anomalous Hall effect (QAHE) came from magnetically doping thin films of the 3D topological insulator $(Bi,Sb)_2Te_3$ with transition metals such as Cr or V [19]. The magnetic dopants break time-reversal symmetry, while the topological surface states provide the necessary band structure. At sufficiently low temperatures, this leads to a quantized Hall conductance with $R_{xx} \to 0$ in the absence of an applied magnetic field.

A natural question following the quantum anomalous Hall paradigm is what becomes of the edge physics when time-reversal symmetry is preserved. In such systems, the gapless boundary modes occur in *helical* pairs: one spin orientation propagates in a given direction, while the opposite spin

counter-propagates along the same edge. Because these modes are related by time-reversal symmetry, elastic backscattering between them is forbidden in the absence of magnetic perturbations, leading to robust, dissipationless transport channels.

Kane and Mele [3] demonstrated that adding intrinsic spin–orbit coupling to a spinful honeycomb lattice transforms each spin sector into a Haldane model with opposite Chern numbers. This construction yields a time-reversal-symmetric topological insulator whose boundary supports helical edge states protected by Kramers degeneracy. Unlike Chern insulators, which are classified by an integer Chern number, these phases are described by a $\mathbb{Z}_2$ topological invariant that distinguishes them from trivial band insulators. The experimental realization of this physics in HgTe/CdTe quantum wells [20] confirmed the existence of the quantum spin Hall effect and established it as a distinct and experimentally accessible class of topological matter.

In summary, the IQHE provided the first bridge between topology and transport, the Haldane model revealed that this connection is not limited to magnetic fields, and the Kane-Mele model has extended the paradigm to time-reversal-symmetric topological phases. These insights underpin much of the modern understanding of topological quantum matter.

1.4 The Fractional Quantum Hall Effect

Returning to the setting of a high-mobility two-dimensional electron gas (2DEG) in a strong perpendicular magnetic field, we now consider the regime where electron–electron interactions dominate the physics. In the noninteracting picture, the integer quantum Hall effect (IQHE) arises when Landau levels are filled by an integer number of electrons per flux quantum. However, in 1982 Tsui, Stormer, and Gossard [21] discovered a qualitatively new phenomenon: at certain *fractional* Landau-level fillings, the Hall resistance R_{xy} remained perfectly quantized, while the longitudinal resistance R_{xx} vanished. The quantization took the form

$$R_{xy} = \frac{h}{\nu e^2}, \quad \nu = \frac{p}{q} \ \text{(fractional)}, \tag{1.6}$$

where ν is the Landau level filling factor. This was the first experimental evidence of a correlated many-body quantum state with no counterpart in the single-particle theory.

Shortly after this discovery, Laughlin [6] proposed a variational many-body wavefunction that

captures the essential correlations at filling $\nu = 1/(2m+1)$:

$$\Psi_m(z_1, \ldots, z_N) = \prod_{i<j} (z_i - z_j)^{2m+1} \exp\left(-\sum_k \frac{|z_k|^2}{4\ell_B^2} \right), \tag{1.7}$$

where $z_j = x_j + iy_j$ are complex coordinates in the 2D plane, m is a nonnegative integer, and ℓ_B is the magnetic length. This Jastrow factor enforces strong correlations by forcing electrons to avoid each other, thereby minimizing Coulomb repulsion. From a gauge-invariance argument, Laughlin further showed that quasiparticle excitations above this ground state carry an *exactly fractional* electric charge $e^* = e/(2m+1)$.

While Laughlin's construction elegantly explains the $\nu = 1/(2m+1)$ states, a more general framework was introduced by Jain [22] to capture the rich hierarchy of observed filling fractions. The central idea is that an electron in a magnetic field can bind to an *even* number $2m$ of fictitious flux quanta to form a new quasiparticle—the *composite fermion* (CF). This flux attachment modifies the effective magnetic field seen by the CFs:

$$B^* = B - 2mn_{\mathrm{e}}\phi_0, \tag{1.8}$$

where n_{e} is the electron density and $\phi_0 = h/e$ is the flux quantum. Remarkably, the strongly interacting electrons in B can then be reinterpreted as *weakly* interacting CFs in B^*. Whenever the CFs fill an integer number p of their own Landau levels, the system realizes a fractional quantum Hall (FQH) state at electron filling

$$\nu = \frac{p}{2mp \pm 1}. \tag{1.9}$$

This sequence of fractions—$\nu = 1/3, 2/5, 3/7, \ldots$ for $m = 1$—is known as the *Jain sequence* and matches a large set of experimentally observed plateaus.

A defining feature of the FQH state is that its quasiparticles are neither bosons nor fermions, but *anyons*. Exchanging two Abelian anyons multiplies the many-body wavefunction by a phase factor $e^{i\theta}$ with θ not equal to 0 or π [23, 24, 25]. In the Laughlin $\nu = 1/(2m+1)$ state, $\theta = \pi/(2m+1)$, reflecting the braiding statistics of these excitations in two dimensions. Experimental detection of this fractional statistics has been pursued via interferometric measurements, in which the interference phase is sensitive to both the Aharonov–Bohm contribution and the anyonic statistical angle [26, 27].

Just as the IQHE has a zero-field cousin in the integer quantum anomalous Hall effect (QAHE), one can ask whether fractional quantum Hall states can exist without an external magnetic field. Theoretically, this is possible if a partially filled, topologically nontrivial band is sufficiently flat and hosts strong electron–electron interactions. In such a setting, the kinetic energy is quenched much like in a Landau level, allowing interactions to stabilize *fractional Chern insulator* (FCI) phases [28, 29, 30, 31, 32]. The key requirement is to engineer a nearly flat band with nonzero Chern number, so that the Berry curvature mimics the role of a magnetic field.

The concept of FCIs, firmly established around 2011 by several theoretical groups, has since motivated an extensive search for suitable material platforms, from optical lattices to moiré superlattices. In such systems, strong electronic correlations at fractional fillings of a topologically nontrivial Chern band can give rise to topologically ordered phases—lattice analogues of the fractional quantum Hall effect (FQHE) that emerge without Landau level quantization. In their transport manifestation, these phases realize the *fractional quantum anomalous Hall* (FQAH) effect. The experimental realization and detailed characterization of FCIs and FQAH states—particularly in moiré transition-metal dichalcogenide bilayers—constitute the central focus of this thesis.

1.5 Two-Dimensional van der Waals Materials

Atomically thin, two-dimensional (2D) materials—most famously graphene and the family of transition metal dichalcogenides (TMDs)—offer an exceptional platform for realizing and probing strongly correlated topological phases of matter. These materials consist of covalently bonded atomic planes stacked together via weak van der Waals (vdW) forces, enabling their mechanical exfoliation from bulk crystals down to the monolayer limit [33, 34]. The absence of dangling bonds at the surfaces allows disparate 2D crystals to be stacked with atomically sharp interfaces, forming *vdW heterostructures* with designer properties [35].

Several intrinsic advantages make 2D vdW materials particularly well-suited for the study of strongly correlated topological matter:

(1) Unprecedented Tunability

One of the defining strengths of 2D materials is their extraordinary degree of in situ tunability. In a typical device geometry, a metallic gate electrode separated by a dielectric layer allows the carrier

density in the 2D channel to be tuned continuously by electrostatic gating—effectively shifting the Fermi level over a broad range without the need for chemical substitution. This is in stark contrast to bulk three-dimensional crystals, where modifying the carrier density generally requires chemical doping, often necessitating the synthesis of entirely new crystals for each doping level.

Moreover, employing a dual-gate configuration—top and bottom gates separated by insulating layers—enables independent control of both the carrier density and the perpendicular displacement field D. This field can modify the band structure and adjust the bandwidth. Such control is particularly crucial in correlated systems, where the competition between kinetic energy and Coulomb repulsion can be tuned to access distinct quantum phases.

A further transformative capability arises from the ability to assemble heterostructures with precise rotational alignment or intentional twist angles between layers. A small twist or slight lattice mismatch produces a long-wavelength interference pattern known as a moiré superlattice [10, 36]. This emergent periodicity dramatically alters the electronic structure—quenching the kinetic energy, generating flat minibands, and introducing nontrivial topology—thereby enabling correlated and topological phases absent in the constituent layers.

(2) Exceptional Cleanliness and Interface Quality

Reducing a material to a single or few atomic layers can substantially suppress bulk defect scattering simply by virtue of removing the volume in which such defects reside. More importantly, 2D materials can be encapsulated between pristine layers of hexagonal boron nitride (hBN), a wide-bandgap insulator with atomically flat surfaces and low charge trap density [37]. This encapsulation both shields the active layer from environmental contamination and screens charge disorder from the substrate, enabling ultra-clean electronic transport.

In the cleanest devices—such as hBN-encapsulated monolayer graphene—quantum mobilities can exceed 10^7 cm^2/Vs at low temperatures [38], surpassing even those of the highest-quality GaAs/AlGaAs semiconductor heterostructures. Defect densities can be as low as a few 10^7 cm^{-2}, enabling the appearance of quantum Hall plateaus at magnetic fields below 5 mT and supporting quasiparticle mean free paths on the order of 10 μm. This extreme reduction in disorder is essential for stabilizing fragile correlated phases, including the fractional quantum Hall effect, superconduc-

tivity in moiré flat bands, and Chern insulating states.

(3) Scalability and Device Integration

The deterministic assembly of vdW heterostructures offers unparalleled flexibility in device design. Layers of different materials can be stacked, patterned, and contacted with conventional lithographic techniques, allowing integration with standard electronic circuitry. The ability to precisely define edge terminations, construct multiterminal geometries, and interface with optical or microwave probes greatly expands the experimental toolkit for studying quantum phenomena.

Looking ahead, advances in large-area growth techniques, such as chemical vapor deposition (CVD) and molecular beam epitaxy (MBE), are steadily improving the scalability of high-quality 2D materials. As synthesis methods mature, it is plausible that vdW heterostructures could become the building blocks of next-generation electronics and quantum technologies [39, 40]—combining the tunability and cleanliness of exfoliated flakes with wafer-scale fabrication compatibility.

1.6 Moiré Flat Bands in Graphene and Transition Metal Dichalcogenides

The realization of moiré flat bands in van der Waals heterostructures has opened a new frontier for engineering correlated and topological quantum phases. The most widely publicized example is magic-angle twisted bilayer graphene (MATBG), in which the interlayer hybridization between two slightly rotated graphene sheets produces extremely flat bands at specific "magic" twist angles near $\theta \approx 1.1^\circ$ [41]. In a flat band, the kinetic energy is strongly quenched, and the Coulomb interaction energy dominates, leading to a fertile ground for correlated electron physics.

Transport experiments in MATBG [42, 10] revealed correlated insulating states at integer moiré fillings—including half filling—where a simple band picture would predict metallic behavior. Upon doping away from certain insulating states, the system exhibited superconductivity, highlighting the role of electronic correlations enabled by the flat moiré band. Furthermore, Berry curvature calculations have shown that the flat bands in MATBG can carry nontrivial topology [43, 44], although the combined twofold rotation and time-reversal symmetry (C_2T) enforces a net Chern number of zero unless broken by effects such as ferromagnetism or alignment with hexagonal boron nitride (hBN). Under such symmetry breaking, quantized anomalous Hall states have been observed [45, 46].

While MATBG served as the initial platform for moiré flat-band physics, the concept of engineering strongly correlated bands is far more general and extends naturally to other two-dimensional materials. In recent years, twisted homo- and heterobilayers of semiconducting transition metal dichalcogenides (TMDs) have emerged as an exceptionally rich arena for exploring correlated and topological phenomena [36, 47].

Semiconducting TMD monolayers (e.g., WSe_2, WS_2, $MoTe_2$) are well described at low energies by a massive Dirac model, with conduction and valence bands separated by a direct gap of $\sim$1–2 eV at the $\pm K$ points [48, 49]. Strong intrinsic spin–orbit coupling in TMDs—hundreds of meV in the valence band—locks spin and valley degrees of freedom: carriers at $+K$ are spin-up, and those at $-K$ are spin-down [50]. This spin–valley locking effectively reduces the internal degrees of freedom compared to graphene, simplifying the low-energy manifold and giving rise to valley-contrasting optical selection rules that allow direct optical probing of individual valleys.

Due to the existence of multiple TMD species, either homobilayer and heterobilayer moiré superlattices can be created by stacking them together. Homobilayers can be created by twisting two layers of the same material, while heterobilayers combine two different TMDs—such as WSe_2/WS_2 or $MoTe_2/WSe_2$—stacked at relative twist angles near 0° or 60°. The study of correlated excitonic lattices in WSe_2/WS_2 is the topic of the second chapter of this thesis. In heterobilayers, the moiré periodicity is largely determined by the intrinsic lattice mismatch, making the system less sensitive to twist-angle disorder.

One practical advantage of TMD moirés is that, unlike magic-angle twisted bilayer graphene, the emergence of flat minibands does not require a finely tuned "magic" twist angle. The combination of large carrier effective masses and a deep moiré potential ensures that narrow bands form over a wide range of twist angles [36]. This robustness significantly relaxes device fabrication tolerances, enabling systematic exploration of correlated phases without the stringent angular precision demanded in graphene-based moirés.

The reduced kinetic energy in these flat bands enhances the role of electron–electron interactions, driving the formation of correlated insulating states at commensurate band fillings. Transport experiments have identified incompressible phases at both integer and fractional occupancies of the moiré superlattice. Optical sensing techniques have provided a complementary, highly sensitive probe: in one approach [51], a monolayer WSe_2 "sensor" placed adjacent to the active moiré layer is

monitored via its excitonic resonances. The local dielectric environment changes when a correlated insulating state forms in the neighboring moiré layer, shifting the energy of the WSe_2 exciton. This method has revealed clear signatures of insulating states not only at integer fillings but also at fractional fillings associated with generalized Wigner crystals and candidate fractional Chern insulators.

Beyond correlation-driven insulating behavior, TMD moiré systems can also host topologically nontrivial phases. A notable example is provided by near-60° $MoTe_2/WSe_2$ heterobilayers, where transport measurements have observed a quantum anomalous Hall (QAH) effect at $\nu = -1$ under a large perpendicular displacement field [52]. In this case, the applied field drives a band inversion in the valence moiré minibands, producing a Chern band with $C = \pm 1$. The resulting ground state supports chiral edge channels and quantized Hall conductance in the absence of an external magnetic field—demonstrating that moiré engineering can stabilize topological order purely from band structure and interactions.

The combination of robust flat-band formation, tunable interaction strength, and access to both correlation-driven and topological phases underscores the power of TMD moiré systems as a platform for exploring exotic quantum matter. In the context of this thesis, these properties are particularly significant for realizing and probing fractional Chern insulator states in twisted $MoTe_2$ bilayers.

1.7 Unresolved Questions and Research Directions

The past few years have seen remarkable experimental advances in the study of correlated and topological phases in moiré materials, including the observation of fractional Chern insulators and quantum anomalous Hall states in twisted transition metal dichalcogenide (TMD) bilayers [53, 12, 13, 14]. Yet, despite this progress, many fundamental questions remain unanswered—both at the level of microscopic mechanisms and in the development of reliable methods for detection and control.

(1) Excitation Gaps and Their Dependence on External Parameters

A central issue is the quantitative evolution of spin and charge excitation gaps as a function of twist angle, magnetic field, and temperature. These gaps govern the robustness of correlated states

to disorder and thermal fluctuations, and their scaling can reveal the underlying quasiparticle structure. For example, determining whether the lowest-energy excitations in an FCI are spin-polarized (spinless) or involve complex spin–valley textures remains an open challenge. Precise mapping of these dependencies requires a combination of transport measurements, compressibility probes, and local spectroscopic techniques.

(2) Role of Band Geometry and Quantum Metric

Beyond the Chern number, the fine details of band geometry—including the Berry curvature distribution and the quantum metric—are predicted to strongly influence the stability of FCIs [54, 55, 56, 57]. In lattice systems, unlike in Landau levels, the Berry curvature can be highly nonuniform across the Brillouin zone, potentially weakening FCI gaps. The quantum metric, which quantifies the "distance" between Bloch states in momentum space, has been proposed as a key ingredient in optimizing interaction-driven topological order. Experimental access to these quantities, potentially through momentum-resolved optical probes or angle-resolved photoemission spectroscopy, remains limited and constitutes an important frontier.

(3) Probing Anyonic Statistics and Edge-Mode Structure

While transport quantization provides indirect evidence for topological order, a definitive demonstration of fractionalized statistics requires direct detection of anyonic braiding phases. In traditional GaAs-based fractional quantum Hall systems, this has been pursued using electronic interferometry [26]. In moiré systems, the challenge is to design interferometric or local scanning-probe platforms capable of resolving the fractional exchange phase at the micron scale. Equally important is characterizing the edge-mode structure of FCIs [58], which may differ from the continuum fractional quantum Hall case due to lattice effects and valley degrees of freedom.

(4) Connection Between FCIs and Correlated Superconductivity

Another unresolved question is whether FCIs and correlated superconductivity in moiré materials share a common origin in the underlying interaction physics. Both phenomena emerge from flat-band electronic structures, yet one corresponds to an incompressible topological phase while the

other is a compressible paired state. Understanding whether they compete, coexist, or arise from proximate phases in the same phase diagram could shed light on the broader relationship between strong correlations and topology.

Here, we attempt to address these questions at least partially, through a combination of device fabrication, magneto-transport and optical spectroscopy, and close interplay with theoretical modeling. Our goal is to clarify how topology and electron–electron interactions conspire to produce novel quantum phases in moiré TMDs, and to establish pathways for their manipulation in future quantum electronic and quantum information technologies.

1.8 Outline of dissertation

The overarching aim of this thesis is to explore how strong electron–electron interactions, when combined with topologically nontrivial band structures, give rise to new quantum phases in moiré transition metal dichalcogenide (TMD) heterostructures. The body of work presented here spans multiple device platforms, experimental techniques, and conceptual themes, but is unified by a focus on correlated and topological states in flat moiré minibands.

The chapters are organized to reflect both the scientific narrative and the chronological progression of the research. Chapter 2 differs somewhat from the rest in that it focuses on optical spectroscopy of excitonic states in WSe_2/WS_2, whereas Chapters 3–6 are centered on electronic transport and scanning probe studies of twisted $MoTe_2$. Nevertheless, all chapters address the broader question of how strong correlations manifest in moiré-engineered systems.

Chapter 2 reports on work published in [59], in which we sought to emulate Bose–Hubbard model physics using interlayer excitons in WSe_2/WS_2 heterobilayer moiré superlattices. The long lifetimes and large dipole-dipole interactions of these excitons, combined with the periodic moiré potential, provide a promising platform for realizing strongly interacting bosonic lattice systems. Using gate- and power- dependent photoluminescence spectroscopy, we probed exciton density dependent energy shifts consistent with exciton–exciton interactions in a periodic potential landscape.

Chapter 3 describes the first observation of the fractional quantum anomalous Hall (FQAH) effect in a solid-state system, achieved in twisted $MoTe_2$ bilayers [13]. At fractional fillings of a topologically nontrivial Chern band, we observed vanishing longitudinal resistance and quantized Hall resistance at $R_{xy} = \pm h/(C\nu e^2)$ without an external magnetic field. This discovery provided

direct evidence that moiré TMDs can host lattice analogues of the fractional quantum Hall effect—fractional Chern insulators (FCIs)—driven purely by interactions in a flat Chern band.

In Chapter 4, we move from bulk transport signatures to direct spatial imaging. Using microwave impedance microscopy (MIM) at cryogenic temperatures, we visualized the chiral edge channels of both integer and fractional QAH states in twisted $MoTe_2$ [58]. This work constitutes the first real-space imaging of fractional edge states in any material platform. The measurements revealed not only the presence of narrow, well-defined fractional edge channels, but also provided insight into their spatial confinement, robustness, and relation to bulk incompressibility.

Chapter 5 extends the exploration of twisted $MoTe_2$ into higher-energy moiré minibands with larger Chern numbers [60]. Motivated by analogies to higher Landau levels in the continuum, we investigated whether these higher Chern bands could support exotic correlated states, potentially distinct from those in the first Chern bands. The results shed light on how the interplay between band topology, moiré potential, and twist angle shapes the stability of such phases.

The final chapter, Chapter 6, presents the realization of a dissipationless FCI in twisted $MoTe_2$, reported in [61]. This work not only demonstrated vanishing R_{xx} in the fractional regime over a broad temperature range, but also provided the first systematic study of activation gaps in a moiré FCI. By mapping the gap's dependence on filling factor and magnetic field, we obtained quantitative insight into the quasiparticle excitation spectrum and the roles of spinful and spinless excitations in stabilizing the fractional phase.

Together, these chapters chart a progression from excitonic correlations in bosonic moiré systems, through the discovery of fractional topological order in twisted $MoTe_2$, to spatially resolved studies of edge states and higher Chern bands, culminating in the demonstration of a dissipationless fractional Chern insulator. The results highlight the versatility of moiré TMD heterostructures as a laboratory for exploring the interplay of strong correlations, topology, and reduced dimensionality, and lay the groundwork for future experiments aimed at probing anyonic statistics, non-Abelian excitations, and topological quantum computation.

Chapter 2

EXCITONIC DIPOLAR INTERACTIONS IN MOIRÉ SUPERLATTICES

The moiré potential landscape formed in twisted heterostructures of transition metal dichalcogenides (TMDs) introduces a spatially periodic modulation of the electronic band structure, effectively creating an artificial lattice of quantum dots [62, 63, 64, 65, 51, 66, 67, 68, 69, 70, 71]. These moiré superlattices have enabled the emergence of correlated charge textures and diverse magnetic ground states across various filling regimes. When excitons—bound electron-hole pairs—are photoexcited in such systems, they become trapped in these periodic potentials, forming what are known as moiré excitons.

In heterobilayer configurations such as $WSe_2/MoSe_2$ and WSe_2/WS_2, the band alignment is of type-II character, spatially separating the electron and hole into opposite layers (Fig. 2.1a)[63, 72]. This layer separation imparts a permanent out-of-plane electric dipole moment to the resulting interlayer excitons (IXs), leading to notable dipolar interactions between them. Prior studies on $MoSe_2/WSe_2$ systems have demonstrated that such repulsive dipole-dipole interactions are significant even at nanometer-scale separations, with an estimated interaction energy of roughly 2 meV between IXs spaced by $\sim$7 nm [73, 74].

Furthermore, exchange interactions tied to the valley degree of freedom have been proposed to induce intriguing polarization textures—such as ring-like patterns—in the spatial diffusion of IXs [75]. These interaction phenomena underscore the strong onsite interactions among excitons in moiré lattices [76, 77], drawing a close analogy to the onsite Coulomb repulsion that underpins Mott-like physics in correlated electron systems (Fig. 2.1b). Such strong bosonic interactions offer fertile ground for exploring quantum phases of light-matter composites.

In this chapter, I discuss the observation of a giant on-site interaction energy—interpreted as a Hubbard U for excitons—arising from dipole-dipole repulsion within a moiré-trapped IX lattice in WSe_2/WS_2 heterostructures. Our experiments further reveal its complex interplay with generalized Wigner crystallization and the emergence of interaction-driven local magnetic textures.

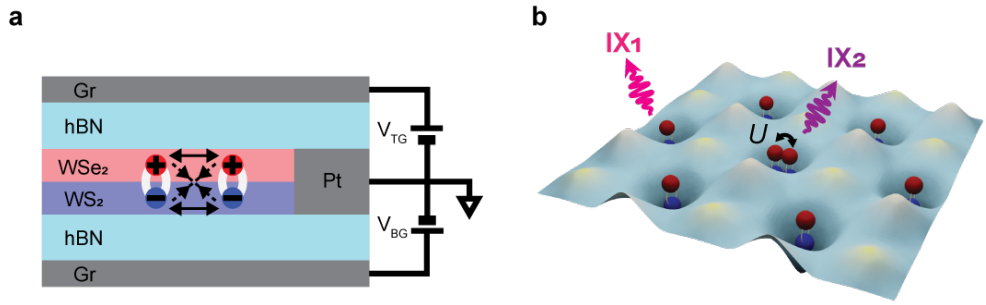

Figure 2.1: Device Schematic. **a,** Dual-gated WSe_2/WS_2 heterobilayer structure illustrating interlayer exciton dipoles and their dipole–dipole and exchange interactions. **b,** Moiré exciton lattice, highlighting double exciton occupancy.

To probe these phenomena, we employ spatially and spectrally resolved photoluminescence (PL) measurements of IXs in dual-gated heterobilayer devices (Fig. 2.1a). The stacking order and relative twist angle of each sample are precisely characterized using piezoresponse force microscopy and second harmonic generation. All data presented here were acquired at a base temperature of 15 K, with continuous-wave optical excitation tuned to 1.685 eV—resonant with the WSe_2 A-exciton transition—unless stated otherwise. The out-of-plane electric displacement field is maintained at zero.

Our findings are based on multiple devices with both R-type (0° twist) and H-type (60° twist) layer stackings, demonstrating high reproducibility across samples. Unless otherwise specified, the results discussed herein are from a representative R-stacked heterobilayer device (denoted DR-1) with a twist angle of approximately 0.8°, yielding a moiré periodicity of 8.0 nm.

2.1 Fabrication and Photoluminescence spectroscopy

In order to fabricate the devices, I began by pre-patterning a bottom gate consisting of a graphite flake encapsulated in hexagonal boron nitride (hBN), contacted by lithographically defined platinum electrodes. Monolayer flakes of WS_2 and WSe_2 were isolated via mechanical exfoliation, and their crystal orientations were verified using second harmonic generation (SHG) microscopy.

A deterministic dry-transfer technique utilizing a polycarbonate (PC) film mounted on a polydimethylsiloxane (PDMS) stamp was used to sequentially pick up the exfoliated monolayers. The

assembled heterostructure was then laminated onto the pre-fabricated bottom gate. To ensure clean interfaces, the stack was subjected to contact-mode atomic force microscopy (AFM) cleaning using a Bruker Dimension Icon system.[78]

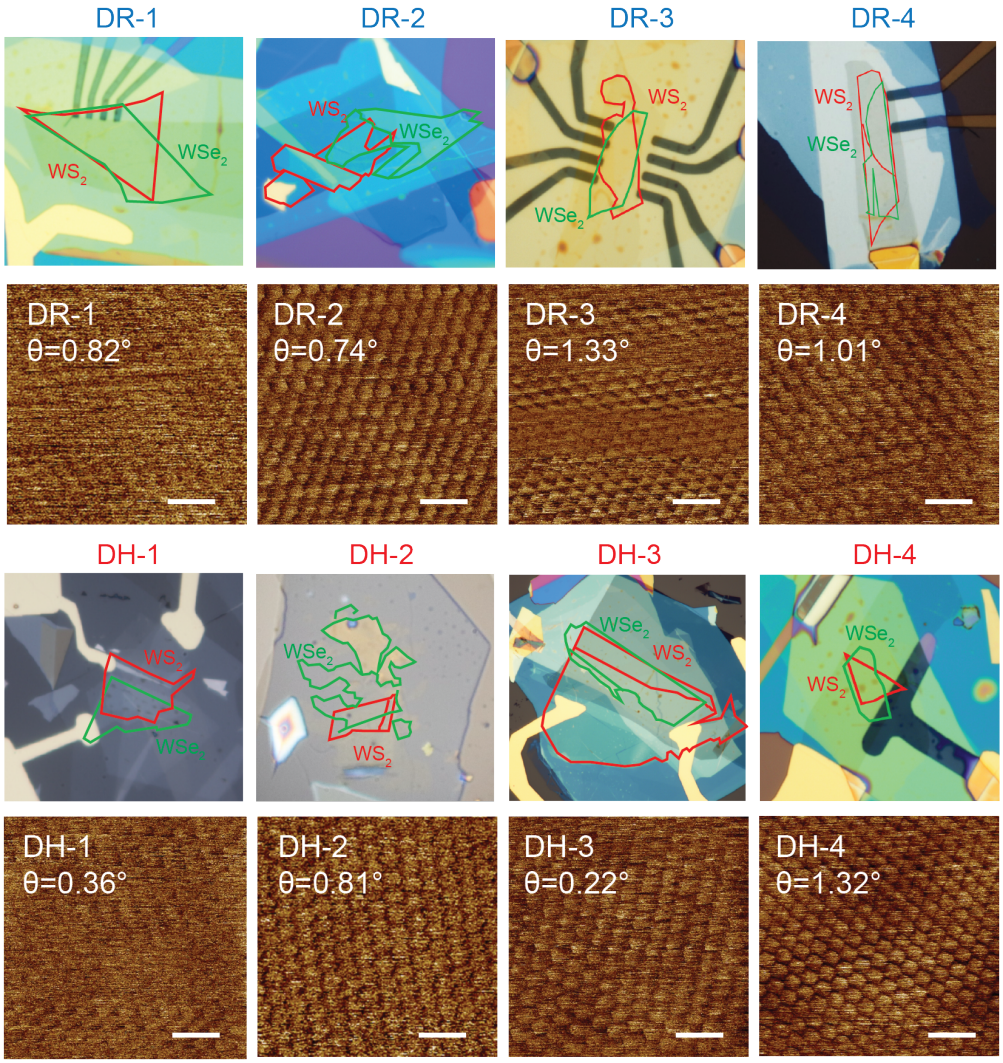

Figure 2.2: Device images and twist angle determination. **P**iezoresponse force microscopy (PFM) images of both R- and H-stacked samples. Scale bar: 20 nm.

The twist angle and resulting moiré periodicity were characterized through piezoresponse force microscopy (PFM), as described in Ref. [66, 79]. Representative PFM maps across multiple devices are shown in Fig. 2.2. Finally, a top gate composed of graphite encapsulated by hBN was aligned

and transferred to complete the dual-gated structure.

All optical measurements were performed using a home-built confocal microscope mounted in an exchange-gas cryostat (attoDRY 2100). Unless otherwise noted, the sample temperature was stabilized at 15 K. For steady-state photoluminescence (PL), the device was excited under normal incidence by a tunable continuous-wave Ti:sapphire laser ($M^{squared}$ SolsTiS), which was tuned to the A-exciton resonance of WSe_2. Polarization control was implemented using linear polarizers, half-wave plates, and quarter-wave plates to allow for circularly polarized excitation and detection.

To suppress laser background, a 750 nm long-pass filter was placed before the collection optics. The PL signal was dispersed with a 600 grooves/mm diffraction grating in an Andor Solis spectrometer and detected with a Si CCD. The laser power incident on the sample was precisely controlled using a combination of a half-wave plate and polarizers.

RMCD measurements were performed using the same SolsTiS laser, fixed at a wavelength of 745.5 nm. The incident beam was modulated in intensity at 1 kHz using an optical chopper. Circular polarization modulation at 50.1 kHz was achieved by sending the beam through a linear polarizer oriented 45° relative to the fast axis of a photoelastic modulator (PEM) operating at quarter-wave retardation.

The reflected signal was collected with an avalanche photodiode and demodulated using lock-in amplifiers referenced to both modulation frequencies. The circular dichroism signal was extracted by normalizing the polarization-dependent modulation amplitude to the total intensity modulation, allowing for accurate removal of baseline reflectivity variations.

2.2 Density-Dependence of Dipole Ladder States

At low optical excitation power densities ($P = 20$ nW/μm^2), the photoluminescence (PL) spectra of interlayer excitons (IXs) exhibit pronounced signatures of moiré miniband filling (Fig. 2.3). Notably, the PL intensity is enhanced at fractional fillings of the moiré superlattice, reflecting the presence of correlated electronic states previously reported in similar systems.[65, 80, 81, 82] These features indicate excellent sample quality, allowing resolution of intricate charge-order effects.

Upon increasing P, in addition to clear emission features at integer band fillings, a distinct PL peak (labeled IX2) emerges approximately 34 meV above the primary IX1 transition, most prominently near charge neutrality (see the $P = 2$ μW/μm^2 spectrum in Fig. 2.3). Across ten inde-

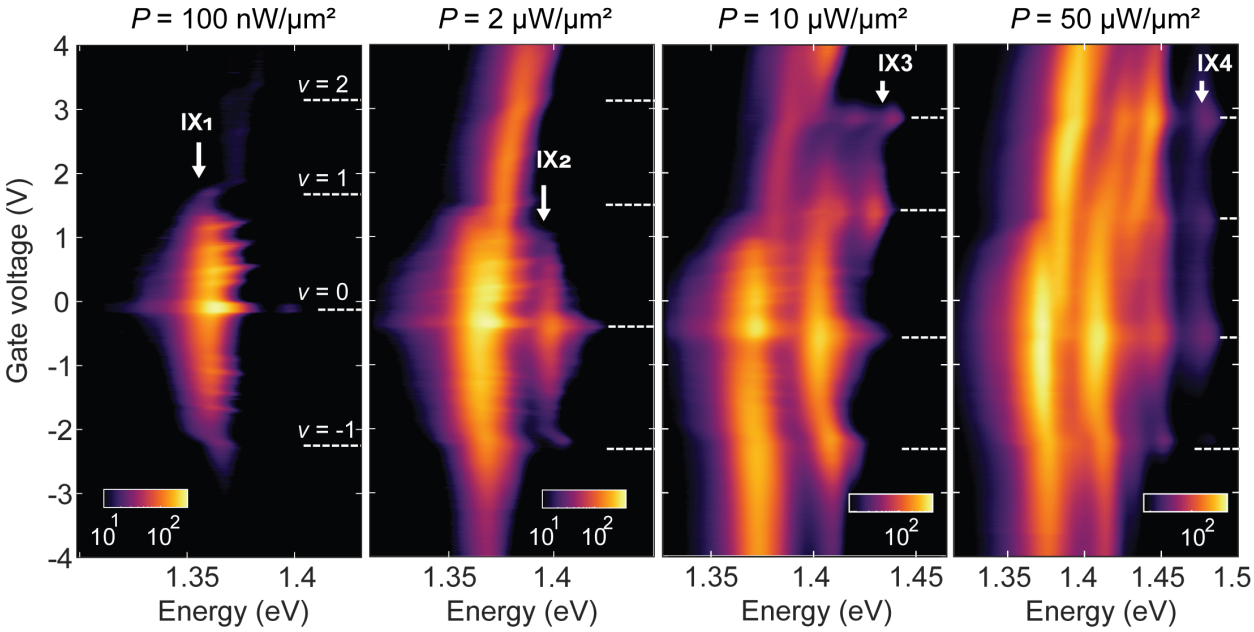

Figure 2.3: Excitation-dependent photoluminescence. Interlayer exciton PL intensity versus doping and emission energy at selected optical excitation powers P. Integer moiré band fillings are marked. At higher P, additional PL peaks (IX_2, IX_3, IX_4) emerge above the ground state emission (IX_1).

pendently fabricated devices, this energy splitting between IX2 and IX1, denoted ΔE_{21}, consistently falls within the 30–37 meV range (Fig. 2.4), highlighting the robustness of the phenomenon. As P is further increased, IX2 becomes observable over a broader doping window. At $P = 2\ \mu\mathrm{W}/\mu\mathrm{m}^2$, for instance, IX2 mirrors IX1 across a full filling range $|\nu| < 1$, and correlated features such as fractional band fillings remain evident in its PL signal. These observations suggest that the local excitonic energy spectrum within a moiré unit cell is strongly modulated by exciton occupation density.

To elucidate the physical origin of IX2, we conduct a power-dependent PL measurement while holding the filling factor fixed at $\nu = 0$. Figure 2.5a displays the spectra acquired under co-circular excitation and detection. The integrated PL intensities of IX1 and IX2 are extracted and plotted against P in Fig. 2.5b. The IX1 signal shows a pronounced saturation behavior with increasing excitation power, consistent with a long-lived population. In contrast, IX2 appears only beyond a finite excitation threshold ($P_{\mathrm{th}} = 0.4\ \mu\mathrm{W}/\mu\mathrm{m}^2$) and increases approximately linearly with P

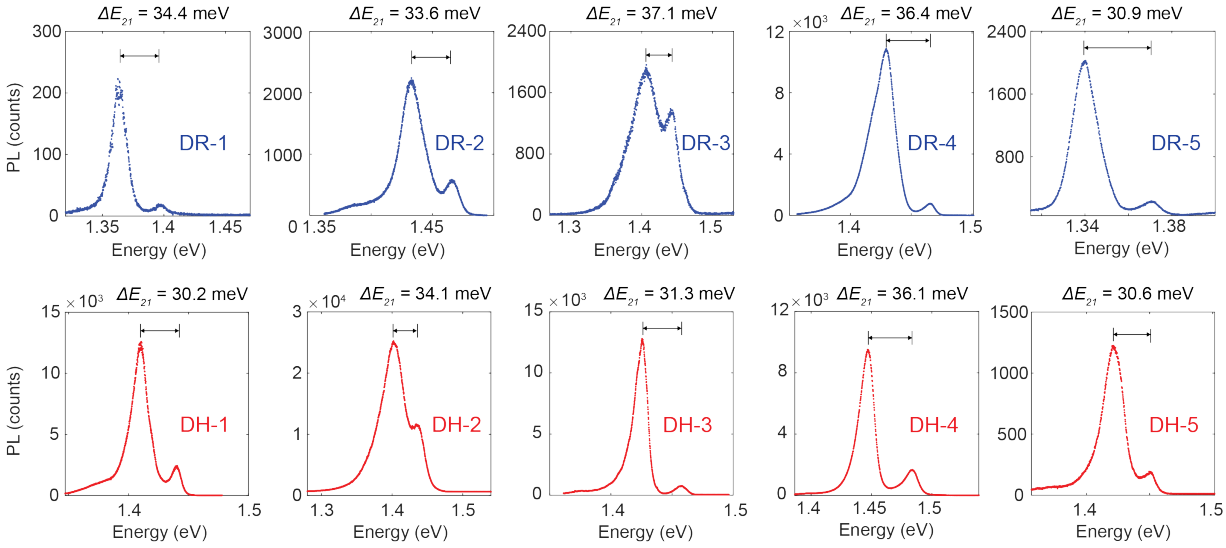

Figure 2.4: Interlayer exciton spectra for differnt devices. PL spectra of interlayer excitons IX_1 and IX_2 at charge neutrality for each device. The IX_1–IX_2 energy separation ranges consistently from 30–37 meV.

beyond this point.

Using an independent calibration of exciton density versus excitation power, we estimate that the onset of IX2 corresponds to an exciton density near 10^{12} cm^{-2}. This value is on the order of one exciton per moiré unit cell, reinforcing the interpretation that excitons populate the moiré potential in a lattice-like manner akin to electrons in a crystalline potential.

2.3 Exciton Filling, Onsite Interactions, and Spin-Valley Dynamics

The power-dependent emergence of the IX2 emission peak provides direct evidence for strong onsite repulsion between excitons confined in a moiré-trapped lattice. At low optical excitation power, the interlayer excitons (IXs) are sparsely distributed, occupying isolated moiré sites. As the excitation power increases, the overall exciton population grows approximately according to a power-law scaling [83], gradually filling more lattice sites across the superlattice. In this dilute regime, IX1 emission shows only a weak and continuous blue shift, attributed to long-range dipolar repulsion between excitons occupying neighboring cells—double occupancy remains energetically prohibited.

Once the exciton density reaches a critical threshold—corresponding to one exciton per moiré

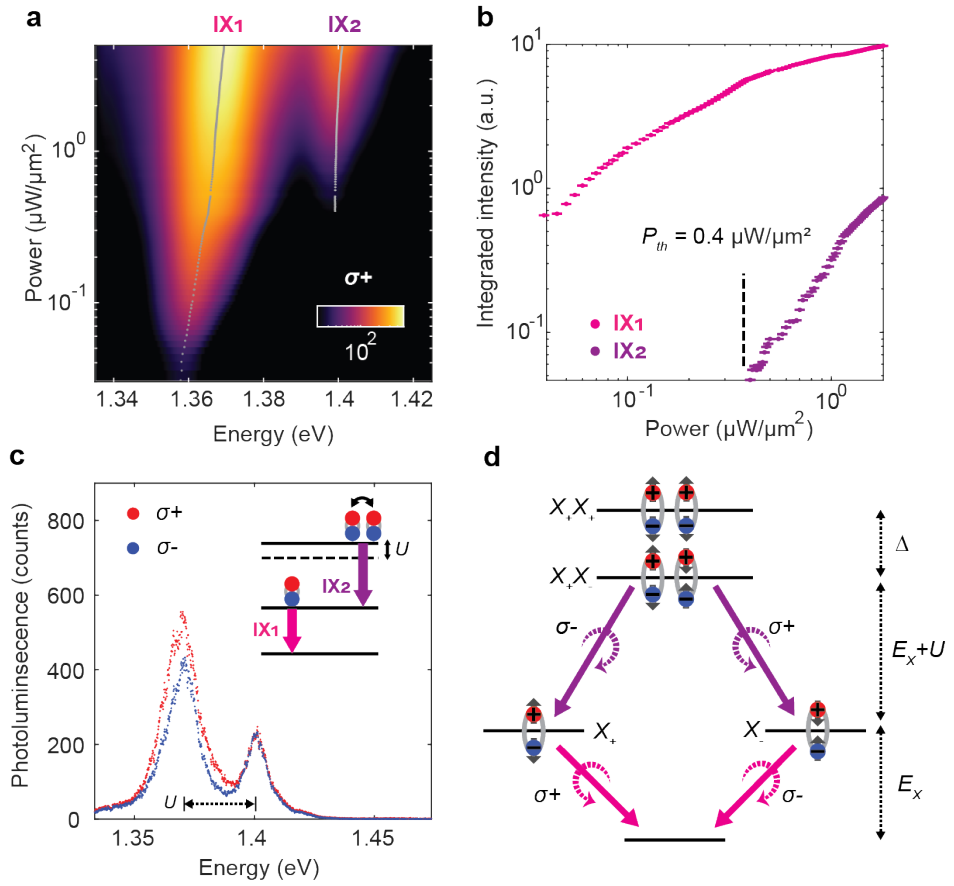

Figure 2.5: Spin-dependent IX photoluminescence. **a,** Polarization-resolved PL spectra at charge neutrality under σ^+ excitation and detection while varying excitation intensity P. **b,** Integrated PL intensity versus P, revealing a threshold-like onset for the IX_2 emission. **c,** σ^+-excited polarization-resolved PL spectrum at $P = 5\ \mu W{\cdot}\mu m^{-2}$. Inset: schematic energy level diagram for two exciton dipoles confined within the same moiré potential minimum, showing repulsive dipole–dipole and exchange interactions. **d,** Energy level schematic for a two-dipole state confined in one moiré site. Two indistinguishable decay pathways may emit photon pairs at energies $E_X + U$ and E_X, potentially resulting in polarization-entangled, unpolarized photons

unit cell—states with two excitons localized within the same potential minimum begin to form (see Fig. 2.1b). This regime reveals a new PL peak, IX2, offset in energy from IX1. We define the single-exciton emission energy as E_X and the onsite dipole-dipole repulsion energy as the excitonic Hubbard interaction U. A two-exciton state confined to the same moiré site therefore has a total energy $E_{2X} = 2E_X + U$ (inset of Fig. 2.5c). Radiative recombination from this doubly occupied state proceeds via a cascade process, producing two photons: one at $E_X + U$ (IX2) and another at E_X (IX1).

Experimental measurements reveal that the interaction energy U lies in the range of 30–37 meV near charge neutrality, depending on the local exciton density. This value is nearly an order of magnitude larger than the long-range excitonic dipole repulsion previously observed in $MoSe_2/WSe_2$ systems [73, 74]. A theoretical estimate for a localized exciton wavefunction confined to a $\sim$2 nm radius [84, 85, 86] yields $U \approx 34$ meV, in good agreement with experiment.

We also observe a clear trend across devices with varying twist angles: the excitonic Hubbard U systematically increases with increasing twist angle (Fig. 2.6a). A natural interpretation is that larger twist angles reduce the moiré superlattice constant, effectively compressing the spatial extent of each trap and bringing the excitons in closer proximity—thereby enhancing the strength of onsite dipolar interactions (Fig. 2.6b).

In addition to this dipolar repulsion, excitons confined to the same moiré cell can also experience a strong exchange interaction if they share the same spin-valley configuration [75]. This leads to a splitting of the two-exciton manifold into singlet and triplet states, with the spin-anti-aligned singlet always being energetically favored. Due to optical selection rules in monolayer TMDs [76], the recombination cascade from this singlet state produces photon polarization patterns that encode the spin-valley structure of the emitter.

Fig. 2.5c presents PL spectra acquired at $P = 5\ \mu\text{W}/\mu\text{m}^2$ under co- and cross-circular polarization configurations. The IX1 emission exhibits strong co-circular polarization, consistent with valley-polarized emission from singly occupied moiré traps [64, 65, 75, 81]. In contrast, the IX2 peak is unpolarized, aligning with theoretical predictions for radiative decay from a spin-singlet two-exciton state [76]. The energy level diagram in Fig. 2.5d outlines two degenerate decay pathways: one where the first photon ($E_X + U$) is emitted with σ^- polarization followed by a σ^+ photon at E_X, and the reverse configuration where the helicities are swapped. These two channels are en-

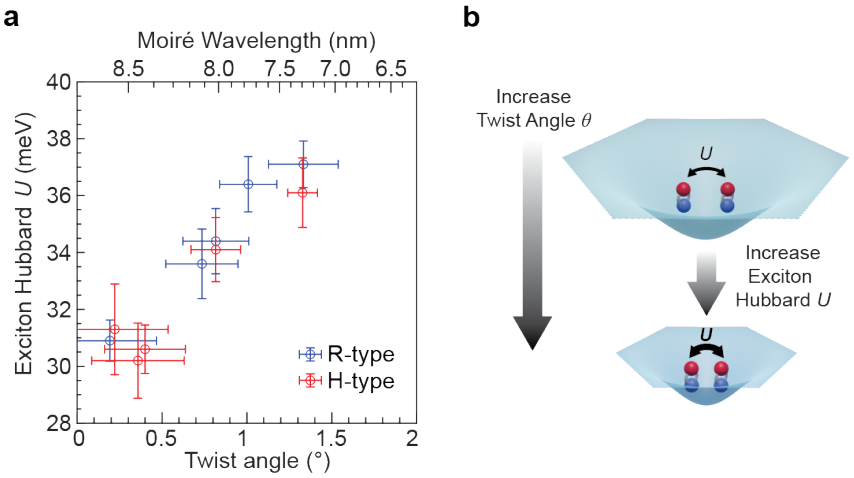

Figure 2.6: Twist angle dependent exciton Hubbard interaction. **a,** Extracted exciton Hubbard U plotted versus twist angle (or equivalently, moiré wavelength). **b,** Illustration of two excitons occupying a moiré trap. As the moiré wavelength decreases, increased spatial confinement enhances dipole–dipole repulsion, leading to larger U.

ergetically indistinguishable and, assuming coherence is maintained during emission, may result in a maximally entangled photon pair:

$$|\Psi\rangle = \frac{1}{\sqrt{2}}(|\sigma^+, \sigma^-\rangle + |\sigma^-, \sigma^+\rangle).$$

While our observation of unpolarized IX2 emission is consistent with the formation of singlet states and potential photon entanglement, further investigation is required to unambiguously establish quantum correlations. Realizing and controlling such a two-exciton moiré-based quantum emitter could pave the way for integrated quantum photonics using 2D materials.

We note, however, that IX1 remains partially polarized even at high power, contrary to expectations if all moiré traps were doubly occupied. This discrepancy arises from the spatial variation of the excitation density due to the Gaussian profile of the laser beam, leading to a mixture of singly and doubly occupied sites across the illuminated region. Additionally, the observed increase in IX1 valley polarization with excitation power (Fig. 2.7a) suggests an as-yet-unexplored mechanism potentially linked to population dynamics or exchange-enhanced valley filtering, motivating further systematic studies.

2.4 *Higher Occupation States and Evidence for Moiré Orbital Multiplicity*

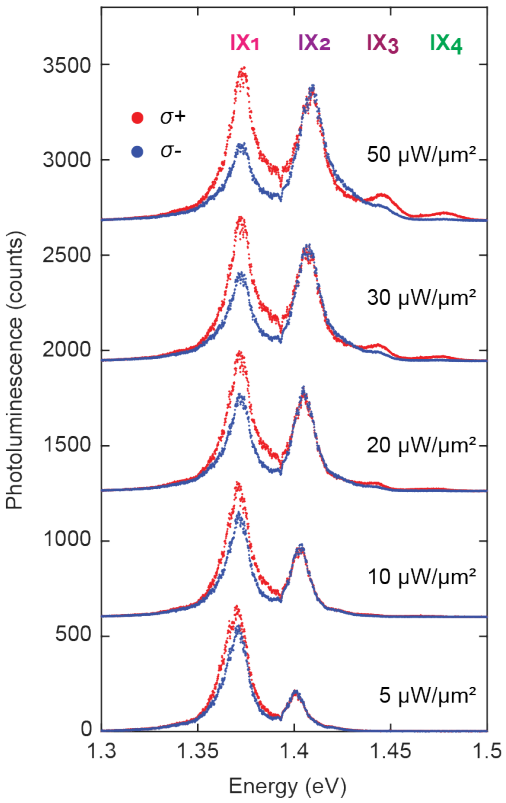

Figure 2.7: Emergence of high-energy excitons under increasing excitation power. Circular polarization-resolved PL spectra under σ^+ excitation at selected optical intensities P.

At elevated excitation densities, additional photoluminescence features emerge, indicative of multiexciton states within a single moiré unit cell. As shown in Fig. 2.3 and Fig. 2.7, at excitation powers exceeding 13 μW/μm^2 and 23 μW/μm^2, two additional peaks—labeled IX3 and IX4—become visible. The presence of four distinct emission peaks implies the system supports up to four excitons per moiré site under strong optical pumping.

To understand the energetic structure of these multioccupancy states, we model the system using the bosonic Hubbard framework. The total energy of n excitons occupying the same orbital is given by

$$E_n = nE_X + \frac{1}{2}U\,n(n-1),$$

where E_X is the energy of a single IX and U is the on-site exciton-exciton repulsion. Radiative decay from these multiexciton states proceeds via cascaded emission processes, with expected photon energies:

$$E_X, \quad E_X + U, \quad E_X + 2U, \quad E_X + 3U,$$

for the first through fourth exciton emissions, respectively (see energy ladder diagram, Fig. 2.8a). This model predicts approximately uniform energy spacing between adjacent peaks, each separated by U. However, at higher exciton numbers, phase-space filling and Pauli exclusion effects are expected to slightly enhance U, thereby modifying the energy spacings.

In agreement with this picture, we extract the energy difference $\Delta E_{32} \approx 36$ meV, marginally larger than $\Delta E_{21} \approx 34$ meV, suggesting a mild increase in U with exciton number. These results support the assignment of IX3 as the next ladder rung in the same moiré orbital as IX1 and IX2. By

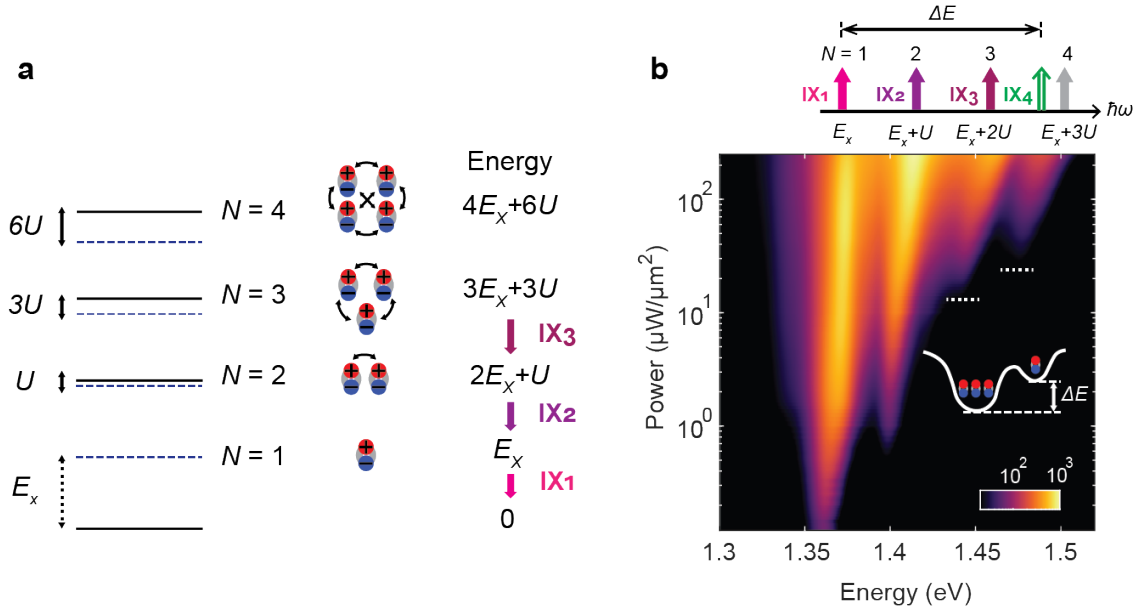

Figure 2.8: Dipole Ladder. **a,** Energy level diagram for a single moiré site with multiple exciton occupancy. Solid and dashed lines represent energy levels with and without dipole–dipole interaction, respectively; total energy for n excitons is labeled. **b,** Top: Schematic PL spectrum from a dipole energy ladder with uniform spacing between IX_1 and IX_3. Bottom: Integrated PL intensity versus excitation power P, showing threshold behavior of IX_3 and IX_4. IX_4 appears at lower energy with co-circular polarization, originating from a fourth exciton in a nearby moiré orbital (see inset).

contrast, the energy spacing $\Delta E_{43} \approx 33$ meV is anomalously small and inconsistent with continued population of the same orbital under the same U scaling.

Crucially, we observe strong co-circular polarization in IX3 and IX4 emissions (Fig. 2.7), indicating the preservation of valley contrast. If all four excitons occupied the same orbital, strong exchange interactions would favor spin-singlet states, leading to depolarized PL. The observed polarization of IX4 therefore suggests that the fourth exciton is likely localized in a distinct excited orbital of the moiré potential (see inset of Fig. 2.8b). Based on this assignment, we estimate the energy offset between the lowest and first excited moiré orbitals to be approximately 100 meV. This includes contributions from both electron and hole confinement potentials.

This interpretation is further supported by the regular spacing of the dipole ladder states (IX1–IX3) and the polarization behavior of IX4, which together rule out alternative origins such as defect-localized excitons [87], or emission from other high-symmetry k-points within the moiré

mini-Brillouin zone [88]. Notably, large-scale density functional theory calculations [89, 90] predict an inter-orbital energy separation of ∼100 meV for WSe_2/WS_2, consistent with our experimental estimate.

To further investigate the presence of multiple moiré orbitals, we turn to magnetic response measurements of the correlated hole ground states. In a triangular moiré lattice with a single orbital per site, half-filling ($\nu = -1$) typically stabilizes a Mott insulator with antiferromagnetic exchange interactions [62], while full-filling ($\nu = -2$) should lead to a band insulator with spin singlet character and vanishing net moment.

However, if two moiré orbitals exist per unit cell, full-filling may result in two holes occupying different orbitals with unpaired spins, producing a net magnetic response. To probe this, we performed reflective magnetic circular dichroism (RMCD) measurements as a function of filling. As shown in Fig. 2.9a, strong RMCD signals are observed near both $\nu = -1$ and $\nu = -2$. The electron-doped side shows no detectable signal and is thus omitted.

RMCD traces versus magnetic field for these fillings are plotted in Fig. 2.9b. While the saturation fields differ, both curves exhibit behavior consistent with paramagnetism, confirming the existence of localized spin moments at both half and full fillings. These findings lend strong support to a two-orbital moiré model (inset, Fig. 2.9b), and align with ab initio predictions for WSe_2/WS_2 heterostructures [89, 90].

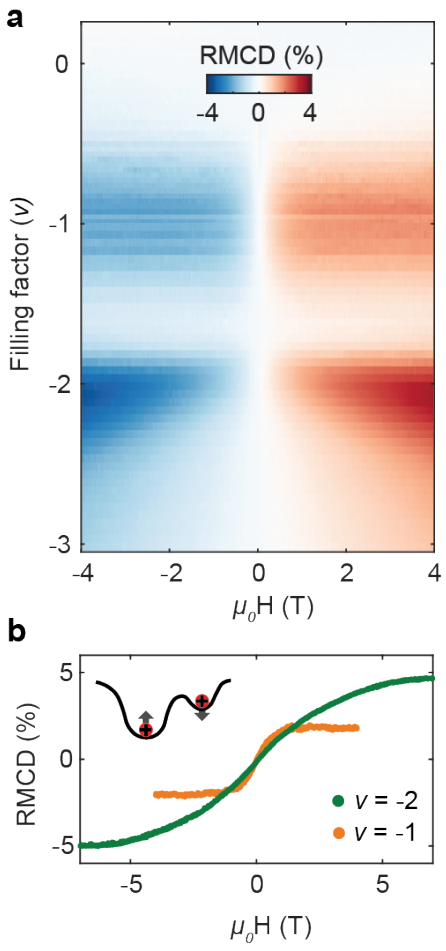

Figure 2.9: RMCD signatures of local moments at integer fillings. **a,** RMCD intensity map as a function of filling factor ν and magnetic field $\mu_0 H$, showing strong signals near $\nu = -1$ and -2. **b,** Line cuts of RMCD versus $\mu_0 H$.

2.5 Excitons in the Presence of Correlated Electronic Order

The tunable interplay between optically injected interlayer excitons and strongly correlated charge states in TMD moiré lattices presents a unique platform for

exploring many-body quantum dynamics. In particular, excitons introduced into a pre-ordered electronic background provide a rich testing ground for interaction-driven phenomena.

Figure 2.10 displays the PL intensity map as a function of carrier filling ν and emission energy, acquired under high excitation power ($P = 50\ \mu\mathrm{W}/\mu\mathrm{m}^2$). At this elevated power, higher-energy IX peaks (IX2–IX4) become prominent near integer-filled correlated insulating states. These enhanced PL features arise from increased exciton lifetimes at these insulating fillings, which enable the exciton density to reach the critical threshold for forming multiply occupied moiré traps—up to the fourth rung of the excitonic dipole ladder.

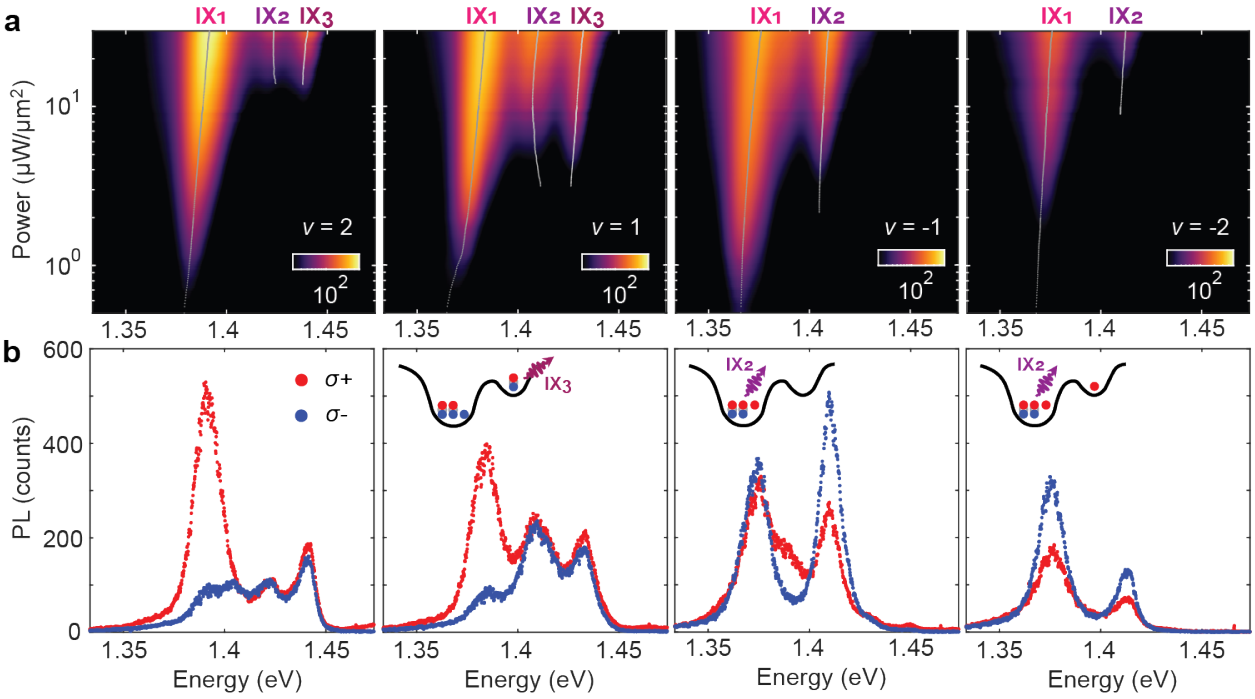

Figure 2.10: Dipole Interaction among correlated states. **a,** PL intensity as a function of excitation power P at integer-filled correlated states. **b,** Circular polarization-resolved PL spectra under σ^+ excitation at $P = 30\ \mu\mathrm{W}\cdot\mu\mathrm{m}^{-2}$. Insets: Schematic depiction of carrier and exciton distribution in a two-orbital moiré model (red: holes, blue: electrons).

Notably, the energy separation between IX1 and IX2 (ΔE_{21}) remains relatively uniform across all doping levels. However, the spacing between IX2 and IX3 (ΔE_{32}) shows a distinct dependence on ν. For $|\nu| \leq 1$, $\Delta E_{32} \approx \Delta E_{21}$, indicating that the third exciton continues to occupy the primary

moiré orbital alongside IX1 and IX2, maintaining a ladder-like progression. In contrast, for $\nu > 1$, ΔE_{32} decreases by 10–15 meV, suggesting that the third exciton transitions into an excited moiré orbital (see schematic in Fig. 2.10b inset). These results show that exciton orbital configurations are highly sensitive to the underlying charge environment.

Finally, we examine how magnetic order in the charge background modifies excitonic optical selection rules using polarization-resolved PL. Figure 2.10b shows spectra collected under co- and cross-circularly polarized configurations at $P = 30\ \mu\mathrm{W}/\mu\mathrm{m}^2$ across several integer fillings. On the electron-doped side ($\nu = 1, 2$), the polarization behavior resembles that observed near charge neutrality: IX1 and IX3 exhibit co-circularly polarized emission, while IX2 remains unpolarized—consistent with prior assignments of singlet and triplet configurations[81].

The hole-doped regime, however, displays markedly different behavior. At $\nu = -1$ and -2, where strong local magnetic moments have been observed (Fig. 2.9), both IX1 and IX2 exhibit robust cross-circularly polarized PL. The reversal of IX1 polarization under hole doping has been previously linked to chiral phonon-assisted spin-valley relaxation processes [81, 91] The appearance of cross-circular polarization in IX2, however, is particularly striking. At these fillings, the doubly occupied moiré site hosts a five-particle bound state—three holes and two electrons. In the cascade recombination process, the polarization of the emitted IX2 photon is influenced by the spin orientation of the majority hole population.

Because the measured IX2 signal is an ensemble average across many moiré sites, the observed polarization implies the presence of a net spin polarization among the hole background, selectively induced by circularly polarized excitation. One plausible mechanism is an RKKY-type ferromagnetic interaction, where itinerant excitons mediate spin alignment of localized holes [66, 92]. These results suggest that moiré excitons not only interact with the charge degrees of freedom, but also serve as probes and potential drivers of spin order in correlated quantum materials.

2.6 Conclusion

We have demonstrated the emergence of a remarkably strong onsite dipole-dipole repulsion between interlayer excitons in WSe_2/WS_2 moiré heterostructures, signaling the realization of a bosonic Hubbard regime in a solid-state material platform. This discovery establishes moiré exciton lattices as a compelling alternative to conventional systems used for exploring the Bose-Hubbard model,

such as ultracold atomic gases [93, 94, 95, 96] and double quantum well structures with engineered traps [97, 98, 99]. In contrast to those platforms, moiré superlattices offer full electrical tunability, atomically sharp interfaces, and access to novel quantum degrees of freedom, such as spin, valley, and layer pseudospins.

The large exciton Hubbard interaction U, combined with the small lattice constant ($\sim$8 nm), suggests that correlated bosonic phases may persist to elevated temperatures, opening the door to strongly interacting regimes accessible under practical conditions. Furthermore, the presence of valley-contrasting physics and nearly flat moiré minibands introduces opportunities for realizing topological exciton condensates, engineered entangled photon sources, and interaction-enabled optoelectronic devices.

Perhaps most intriguingly, moiré heterostructures support a rich landscape of gate-tunable charge and spin orders, enabling the controlled coexistence of bosonic and fermionic particles within the same lattice—an ideal setting for studying correlated Bose–Fermi mixtures and emergent many-body phases beyond conventional frameworks.

Looking ahead, several avenues emerge as promising directions. Although our results suggest the formation of ordered exciton configurations at integer fillings, direct identification of their quantum nature remains an open challenge. A key next step is to investigate possible exciton dipole crystal phases at fractional moiré fillings, which are likely invisible to conventional PL spectroscopy. To detect such subtle ordering, combined approaches involving optical probes and thermodynamic measurements—such as local compressibility or quantum capacitance mapping—may be required [63, 100].

Another important direction is to explore the time-domain response of these excitonic states. Ultrafast optical techniques and photon-correlation measurements could reveal their coherence times, recombination cascades, and entanglement properties. In particular, quantum optical probes of individual moiré emitters will be crucial for testing whether the two-exciton cascades serve as entangled photon sources.

Finally, our observation of distinct moiré orbital levels within each unit cell points to an expanded design space for future quantum materials. Understanding how these multiple orbitals influence many-body interactions and phase formation will be essential for advancing the microscopic control of correlated states in van der Waals moiré systems [36]. Our results thus lay the

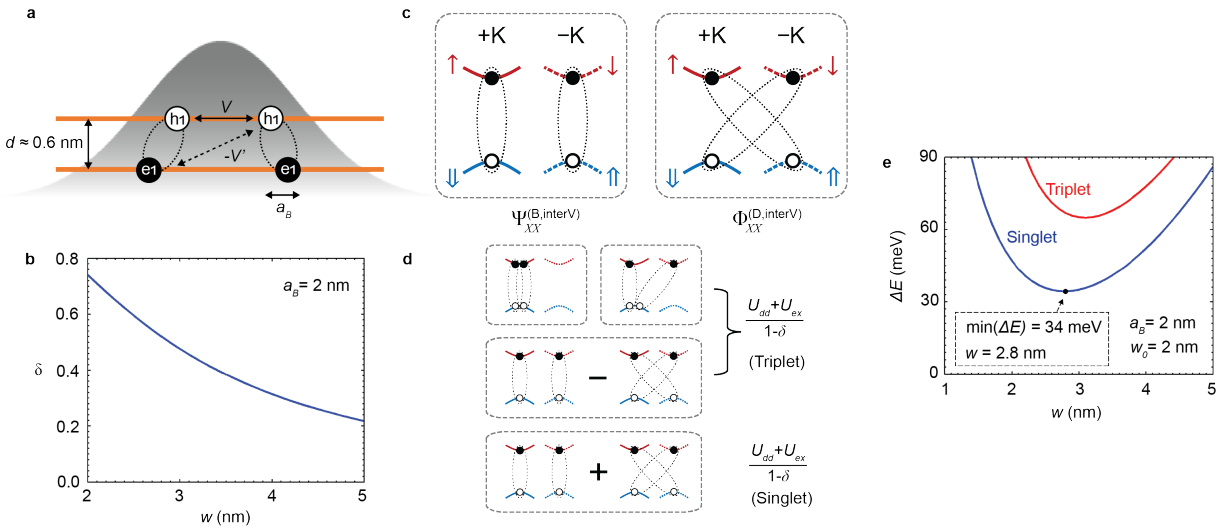

Figure 2.11: Spin–valley dependent interactions between interlayer excitons. **a,** Schematic of two interlayer exciton wave packets localized within the same moiré unit cell. V and V' denote intra- and interlayer Coulomb interactions, respectively. **b,** Computed wavefunction overlap δ as a function of wave packet width w, assuming Bohr radius $a_B = 2$ nm. **c,** Spin and valley configuration of an intervalley exciton pair. **d,** Interaction energy summary for singlet and triplet exciton pairs based on their spin–valley states. **e,** Variational energies of singlet and triplet configurations calculated for $\varepsilon = 5$, $a_B = 2$ nm, and $w_0 = 2$ nm. The minimum energy occurs for a singlet state with $w = 2.8$ nm.

foundation for an excitonic platform in which interaction-driven bosonic, fermionic, and hybrid quantum phases can be discovered, manipulated, and integrated into quantum technologies.

2.7 Supplementary Information: Modeling Exciton–Exciton Dipolar and Exchange Interactions

To analyze the effective interaction between interlayer excitons localized in moiré potentials, we model the system using variational wavefunctions that incorporate both center-of-mass (COM) localization and electron–hole binding. Given that the electron and hole effective masses are approximately equal in WSe_2/WS_2, we adopt relative and COM coordinates: $\mathbf{r} = \mathbf{r}_e - \mathbf{r}_h$ and $\mathbf{R} = (\mathbf{r}_e + \mathbf{r}_h)/2$, respectively.

The single-exciton ground state wavefunction is written as:

$$\Psi^{(0)}(\mathbf{r}_e, \mathbf{r}_h)\,|\sigma_e\rangle\,|\sigma_h\rangle = \phi_{\mathrm{eh}}(\mathbf{r})\,\phi^{(0)}_{\mathrm{COM}}(\mathbf{R})\,|\sigma_e\rangle\,|\sigma_h\rangle,$$

where $\sigma_e \in \{\uparrow, \downarrow\}$ and $\sigma_h \in \{\Uparrow, \Downarrow\}$ label the electron and hole spin/valley states.

The relative-motion wavefunction is taken as the 2D hydrogenic form:

$$\phi_{\mathrm{eh}}(\mathbf{r}) = \frac{2}{\sqrt{2\pi}a_B} e^{-|\mathbf{r}|/a_B},$$

with Bohr radius a_B, while the COM motion is modeled by a Gaussian envelope:

$$\phi^{(0)}_{\mathrm{COM}}(\mathbf{R}) = \frac{1}{\sqrt{\pi}w_0} e^{-|\mathbf{R}|^2/(2w_0^2)},$$

reflecting localization within the moiré potential. Experiments [85] have found a root-mean-square electron–hole separation of $\sqrt{6}/2\, a_B \approx 2.6$ nm, and COM widths ranging from $w_0 \approx 1$–2 nm depending on the system and stacking configuration [86].

For a pair of excitons, labeled by $(\mathbf{r}_{e1}, \mathbf{r}_{h1})$ and $(\mathbf{r}_{e2}, \mathbf{r}_{h2})$, we approximate that the relative wavefunction $\phi_{\mathrm{eh}}(\mathbf{r})$ remains fixed, and treat the COM motion variationally:

$$\phi_{\mathrm{COM}}(\mathbf{R}) = \frac{1}{\sqrt{\pi}w} e^{-|\mathbf{R}|^2/(2w^2)},$$

where w is the variational parameter controlling the exciton size.

To construct the two-exciton states, we apply antisymmetrization to the orbital component to ensure fermionic statistics. We analyze three representative spin/valley configurations:

1. **Intravalley bright–bright pair**: $(\sigma_e, \sigma_h) = (\sigma'_e, \sigma'_h)$. The antisymmetric wavefunction is:

$$\Psi^{(\mathrm{B,intra})}_{\mathrm{XX}} = \frac{\psi(\mathbf{r}_{e1}, \mathbf{r}_{h1})\psi(\mathbf{r}_{e2}, \mathbf{r}_{h2}) - \psi(\mathbf{r}_{e1}, \mathbf{r}_{h2})\psi(\mathbf{r}_{e2}, \mathbf{r}_{h1})}{\sqrt{2(1-\delta)}} \, |\sigma_e\sigma_e\rangle \, |\sigma_h\sigma_h\rangle,$$

where δ denotes the wavefunction overlap:

$$\delta = \int d^2\mathbf{r}_{e1}\, d^2\mathbf{h}_{h1}\, d^2\mathbf{r}_{e2}\, d^2\mathbf{r}_{h2}\, \psi^*(\mathbf{r}_{e2}, \mathbf{r}_{h2})\psi^*(\mathbf{r}_{e1}, \mathbf{r}_{h1})\psi(\mathbf{r}_{e1}, \mathbf{r}_{h2})\psi(\mathbf{r}_{e2}, \mathbf{r}_{h1}).$$

2. **Bright–dark mixed valley pair**: with identical hole spin but opposite electron spin. The antisymmetric wavefunction is:

$$\Psi^{(\mathrm{BD})}_{\mathrm{XX}} = \frac{\psi(\mathbf{r}_{e1}, \mathbf{r}_{h1})\psi(\mathbf{r}_{e2}, \mathbf{r}_{h2}) - \psi(\mathbf{r}_{e1}, \mathbf{r}_{h2})\psi(\mathbf{r}_{e2}, \mathbf{r}_{h1})}{\sqrt{2(1-\delta)}} \, |\sigma_h\sigma_h\rangle \, \frac{|\downarrow_1\uparrow_2\rangle + |\uparrow_1\downarrow_2\rangle}{\sqrt{2}}.$$

3. **Intervalley bright–bright or dark–dark pair**: For bright–bright, e.g., $(\uparrow, \Downarrow)$ and $(\downarrow, \Uparrow)$, and for dark–dark, e.g., $(\uparrow, \Uparrow)$ and $(\downarrow, \Downarrow)$. We define orthogonalized singlet and triplet combinations:

$$\Psi^{(\mathrm{S,inter})}_{\mathrm{XX}} = \frac{\Psi^{(\mathrm{B,inter})}_{\mathrm{XX}} + \Psi^{(\mathrm{D,inter})}_{\mathrm{XX}}}{\sqrt{2(1+\delta)}}, \quad \Psi^{(\mathrm{T,inter})}_{\mathrm{XX}} = \frac{\Psi^{(\mathrm{B,inter})}_{\mathrm{XX}} - \Psi^{(\mathrm{D,inter})}_{\mathrm{XX}}}{\sqrt{2(1-\delta)}},$$

where each Ψ includes orbital symmetrization/antisymmetrization and spin/valley components (see Fig. 2.11).

We now evaluate the variational energy of these exciton pairs. The total energy of a singlet or triplet state is given by:

$$E_{\mathrm{XX}}^{(T)} = 2E_X^{(T)} + \frac{U_{\mathrm{dd}} + U_{\mathrm{ex}}}{1-\delta}, \quad E_{\mathrm{XX}}^{(S)} = 2E_X^{(S)} + \frac{U_{\mathrm{dd}} - U_{\mathrm{ex}}}{1+\delta},$$

where $E_X^{(T/S)}$ is the variational single-exciton energy within the pair configuration, differing from the isolated eigenenergy E_X if $w \neq w_0$. The interaction terms are:

$$U_{\mathrm{dd}} = \int d\mathbf{x}_1 d\mathbf{x}_2 \, \psi^*(\mathbf{x}_1)\psi^*(\mathbf{x}_2)\, \hat{V}_{\mathrm{XX}}\, \psi(\mathbf{x}_1)\psi(\mathbf{x}_2),$$
$$U_{\mathrm{ex}} = -\int d\mathbf{x}_1 d\mathbf{x}_2 \, \psi^*(\mathbf{x}_1)\psi^*(\mathbf{x}_2)\, \hat{V}_{\mathrm{XX}}\, \psi(\mathbf{x}_1')\psi(\mathbf{x}_2'),$$

with $\hat{V}_{\mathrm{XX}}$ containing all pairwise Coulomb interactions:

$$\hat{V}_{\mathrm{XX}} = V(\mathbf{r}_{e1} - \mathbf{r}_{e2}) + V(\mathbf{r}_{h1} - \mathbf{r}_{h2}) - V'(\mathbf{r}_{e1} - \mathbf{r}_{h2}) - V'(\mathbf{r}_{h1} - \mathbf{r}_{e2}),$$

where $V(r) = \frac{e^2}{\epsilon r}$ (intralayer) and $V'(r) = \frac{e^2}{\epsilon\sqrt{r^2+d^2}}$ (interlayer), with dielectric constant $\epsilon \approx 5$ and interlayer spacing $d \approx 0.6$ nm for hBN-encapsulated heterostructures.

Fig. 2.11 summarizes the spin-valley pairings and corresponding interaction energies. The three triplet configurations yield nearly identical variational energies. In Fig. 2.11e, we show the computed interaction energy $\Delta E = E_{\mathrm{XX}} - 2E_X$ versus the variational width w for parameters $a_B = 2$ nm, $w_0 = 2$ nm, and $\epsilon = 5$. The singlet state is energetically favored, with the minimum energy occurring at $w = 2.8$ nm, yielding $\Delta E \approx 34$ meV—closely matching experimental values.

Chapter 3

FRACTIONAL QUANTUM ANOMALOUS HALL EFFECT IN TWISTED BILAYER $MoTe_2$

Topological phases of matter are distinguished by global invariants encoded in the electronic band structure, leading to robust physical phenomena tied to the system's topology. A paradigmatic example is the integer quantum Hall (IQH) effect, where a two-dimensional electron gas under a strong perpendicular magnetic field develops quantized Landau levels [15]. The resulting state exhibits quantized Hall conductance governed by a topological invariant—the Chern number C—as originally described by Thouless and collaborators [17]. This invariant determines the number of chiral edge modes protected against backscattering by topological constraints.

When electron-electron interactions are sufficiently strong, the system can enter more exotic correlated phases such as the fractional quantum Hall (FQH) effect. These fractionalized states support quasiparticles with anyonic statistics [6, 21, 25, 101, 102, 103, 104, 26, 27], offering a route toward topological quantum computation. However, both IQH and FQH states fundamentally require explicit time-reversal symmetry breaking through an applied magnetic field.

In a seminal theoretical advance, Haldane proposed that quantum Hall-like physics could arise in lattice systems without net magnetic flux [18]. This gave rise to the concept of the quantum anomalous Hall (QAH) effect [105], where nontrivial band topology emerges in the absence of external fields. The first experimental realization of the QAH effect was achieved in magnetically doped thin films of topological insulators [19], and subsequent work has extended this to systems with intrinsic magnetism [106] and moiré heterostructures [45, 46, 52, 11, 107].

Building on this foundation, theoretical studies predicted that fractional QAH (FQAH) states—interaction-driven analogues of the FQH effect in topological bands—could also emerge in the presence of strong correlations and suitable band geometry [28, 29, 30, 31, 108, 109]. Yet, unambiguous experimental evidence of such states remained elusive until recent breakthroughs in twisted bilayer $MoTe_2$ [11, 53, 12].

Rhombohedral (R-type) stacked bilayer $MoTe_2$, when twisted at small angles, has proven to be a rich platform for correlated topological phenomena. The system hosts ferromagnetic insulating states at multiple integer and fractional moiré fillings, with the magnetism providing the necessary spontaneous time-reversal symmetry breaking. These features enable the emergence of both integer and fractional QAH phases. Using a trion-based magneto-optical probe [11], a magnetic field–density phase diagram ("fan diagram") was mapped, revealing three gapped states at $\nu = -1$, $-2/3$, and $-3/5$. The trajectories of these states in the $(\mu_0 H, \nu)$ plane follow slopes corresponding to Chern numbers $C = -1$, $-2/3$, and $-3/5$, respectively, as predicted by the Středa formula.

These findings have since been validated by independent exciton-based probes [12], strengthening the case that twisted $MoTe_2$ is a robust material platform for realizing interaction-enabled topological phases. However, the defining experimental hallmark of QAH and FQAH phases remains the observation of quantized Hall resistance R_{xy} accompanied by a vanishing longitudinal resistance R_{xx} at zero magnetic field. In this work, we present direct transport measurements demonstrating this quantization, thereby establishing both the integer and fractional QAH effects in this moiré system.

3.1 Continuum model for twisted TMD homobilayers

We now focus on the theoretical framework for understanding twisted homobilayer TMD systems, with an emphasis on rhombohedrally stacked $MoTe_2$ bilayers near small twist angles. These structures form long-wavelength moiré superlattices that host flat, topologically nontrivial bands. Similar to twisted bilayer graphene (TBG), a continuum model provides an effective low-energy description [41], though key differences arise due to the massive Dirac dispersion and strong spin–orbit coupling intrinsic to TMDs [47].

The starting point is the continuum Hamiltonian describing hole motion in the top and bottom layers near the K valley. Unlike TBG's linear dispersion, here the valence bands exhibit quadratic (massive) dispersion. The interlayer potential, tunneling, and twist-induced momentum shifts are incorporated as:

$$H_K(\mathbf{k}, \mathbf{r}) = \begin{pmatrix} -\frac{\hbar^2(\mathbf{k}-\mathbf{K}_t)^2}{2m^*} + \Delta_t(\mathbf{r}) & T(\mathbf{r}) \\ T^\dagger(\mathbf{r}) & -\frac{\hbar^2(\mathbf{k}-\mathbf{K}_b)^2}{2m^*} + \Delta_b(\mathbf{r}) \end{pmatrix}, \tag{3.1}$$

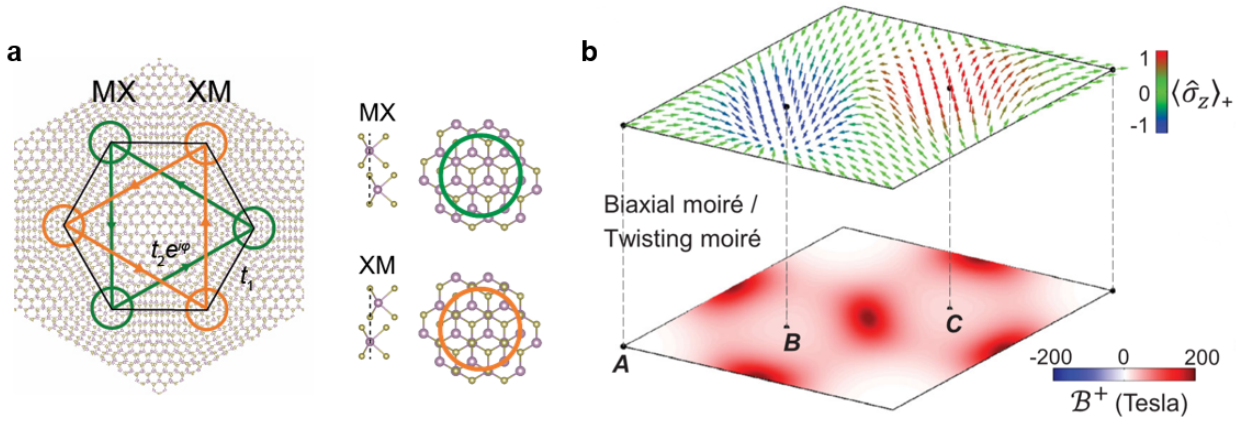

Figure 3.1: Twisted $MoTe_2$ lattice and skyrmion texture. **a**, R-stacked homobilayer $MoTe_2$ has two degenerate energy minima at MX and XM sites. Complex next-nearest-neighbor hopping implements the Haldane model. **b**, Skyrmion lattice of layer pseudospins (top) and corresponding real-space effective magnetic field (bottom). Figure adapted from Ref. [110]

where $\mathbf{K}_{t,b}$ denote the layer-rotated Brillouin zone corners, m^* is the effective mass, and $\Delta_{t,b}(\mathbf{r})$ represent layer-dependent moiré potentials arising from local stacking. The tunneling matrix $T(\mathbf{r})$ captures interlayer hybridization, with its symmetry constrained form derived in analogy to twisted graphene [41]. A convenient way to interpret Eq. 3.1 is by organizing the off-diagonal and on-site potential terms into an effective pseudospin magnetic field acting on the layer degree of freedom.

The layer pseudospin structure is encoded in a real-space field:

$$\mathbf{\Delta}(\mathbf{r}) = (\Delta_x, \Delta_y, \Delta_z) = \left(\mathrm{Re}[T^\dagger(\mathbf{r})],\ \mathrm{Im}[T^\dagger(\mathbf{r})],\ \frac{\Delta_b(\mathbf{r}) - \Delta_t(\mathbf{r})}{2}\right), \tag{3.2}$$

which defines a local pseudospin Zeeman field varying over the moiré unit cell. The in-plane components $\Delta_{x,y}$ govern tunneling between layers, while Δ_z controls layer localization. Importantly, this texture $\mathbf{\Delta}(\mathbf{r})$ forms a skyrmion lattice, characterized by a non-zero winding number across the moiré cell, as shown schematically in Fig. 3.1b. This real-space topological texture generates a spatially varying Berry curvature and acts as an emergent magnetic field for the layer pseudospin.

Symmetry considerations constrain the form of $\mathbf{\Delta}(\mathbf{r})$. For instance, inversion-symmetric stacking configurations such as MM enforce $\Delta_z = 0$, while $C_{2y}T$ symmetry forces wavefunction localization on opposite layers at the XM and MX sites. As a result, the valence band maxima tend to localize

at these symmetry points, forming a honeycomb lattice of orbital centers.

The presence of a skyrmion lattice in $\mathbf{\Delta}(\mathbf{r})$ modifies next-nearest-neighbor hopping amplitudes between orbital centers. For example, carriers hopping between two neighboring MX sites acquire a phase factor $\exp(\pm 2\pi i/3)$ due to the underlying pseudospin winding [47], as illustrated in Fig. 3.1a. This complex phase structure gives rise to an effective Kane–Mele model for each spin–valley flavor—a time-reversed pair of Haldane models:

$$H_{\text{eff}} \sim \sum_{\langle i,j \rangle} t\, c_i^\dagger c_j + \sum_{\langle\langle i,j \rangle\rangle} t'\, e^{i\phi_{ij}} c_i^\dagger c_j, \tag{3.3}$$

with $\phi_{ij} = \pm 2\pi/3$ depending on the hopping direction. This produces flat bands with quantized Chern numbers $C = \pm 1$ per spin–valley sector. Notably, the bandwidth and hopping parameters depend sensitively on the twist angle θ.

The emergence of Chern numbers in these moiré bands can be traced to the winding of $\mathbf{h}_{\text{eff}}(\mathbf{r})$, the layer pseudospin field. When kinetic energy is negligible, i.e.,

$$\frac{\hbar^2 |\kappa|^2}{m^*} \ll |\mathbf{h}_{\text{eff}}|, \tag{3.4}$$

the Chern number is approximately given by the Brouwer degree of the pseudospin texture:

$$\deg(\mathbf{h}_{\text{eff}}) = \frac{1}{4\pi} \int \frac{\mathbf{h}_{\text{eff}} \cdot (\partial_x \mathbf{h}_{\text{eff}} \times \partial_y \mathbf{h}_{\text{eff}})}{|\mathbf{h}_{\text{eff}}|^3}\, dxdy, \tag{3.5}$$

where the integration spans the moiré unit cell. This expression provides a microscopic origin for the Chern number in the limit of strong moiré potential.

In dual-gated geometries, an out-of-plane electric field can be applied to control the layer polarization of carriers. This field introduces an imbalance between the top and bottom layer potentials, which appears as a pseudospin Zeeman term along the z-axis:

$$H_K(\mathbf{k}, D) = h_0(\mathbf{k}) + \mathbf{h}_{\text{eff}}(\mathbf{r}) \cdot \boldsymbol{\sigma} + D\sigma_z, \tag{3.6}$$

where D is linearly proportional to the electric displacement field. This term tunes the system across different symmetry-breaking and topological regimes, enabling electric-field-driven transitions between Chern insulators, trivial insulators, and metallic phases.

3.2 Středa Formalism and Bulk-Edge Correspondence

The presence of nontrivial topology in a gapped electronic system is encoded not only in its edge modes but also in its thermodynamic and transport response functions. One particularly powerful tool for diagnosing such topological phases is the Středa formula, which links the quantized Hall conductivity to the derivative of carrier density with respect to magnetic field. This connection provides a fundamental bridge between the bulk response and the underlying Chern number.

We begin by considering a two-dimensional electron system in thermodynamic equilibrium, subject to a perpendicular magnetic field B, and with a well-defined chemical potential μ. In the absence of low-energy excitations (i.e., within a bulk gap), particle transport is dominated by topologically protected edge channels. Nonetheless, the bulk thermodynamic response retains signatures of topology.

The Středa relation expresses the Hall conductivity σ_{xy} in terms of the particle density n and magnetic field B [111]:

$$\sigma_{xy} = e \left(\frac{\partial n}{\partial B} \right)_{\mu}. \tag{3.7}$$

This identity emerges from multiple routes—Kubo linear response, semiclassical wave packet dynamics, and equilibrium thermodynamics. We follow a thermodynamic argument, starting with the continuity equation and the definition of current in the presence of a gapped Hall response:

$$\mathbf{j} = \sigma_{xy}\, \hat{z} \times \mathbf{E}. \tag{3.8}$$

Taking the divergence and using Maxwell's relation $\nabla \times \mathbf{E} = -\partial \mathbf{B}/\partial t$, the time derivative of charge density satisfies:

$$\frac{\partial n}{\partial t} = -\nabla \cdot \mathbf{j} = \sigma_{xy} \frac{\partial B}{\partial t}. \tag{3.9}$$

By equating the coefficients of time derivatives, we arrive at Eq. 3.7, which reveals that a finite σ_{xy} implies a linear evolution of carrier density with magnetic field, governed by the topological invariant.

In the presence of an energy gap, the quantized Hall conductivity is directly related to the Chern number C of the occupied band:

$$\sigma_{xy} = C\frac{e^2}{h}. \tag{3.10}$$

Substituting into Eq. 3.7, we obtain:

$$C = \frac{h}{e}\left(\frac{\partial n}{\partial B}\right)_{\mu} = \frac{1}{\phi_0}\left(\frac{\partial n}{\partial B}\right), \tag{3.11}$$

where $\phi_0 = h/e$ is the magnetic flux quantum. This version of the Středa formula provides a practical method to extract the topological index from experimental measurements, such as Landau fan diagrams. In such measurements, the positions of gapped states shift linearly with magnetic field, and their slope directly reflects the underlying Chern number.

In moiré systems with graphene and TMDs, the Středa formula has been extensively employed to characterize integer and fractional Chern insulator states [109, 108]. Recent experiments have leveraged non-invasive optical probes—such as trion photoluminescence (PL)—to detect density gaps via changes in dielectric screening [11, 12]. Since excitons are sensitive to the local electronic compressibility, their PL response provides a proxy for the opening of many-body gaps, including Wigner crystals and fractional quantum Hall phases. Thus, the slope of PL features in a (n, B) map can reveal the underlying Chern index via Eq. 3.11.

While the fractional Středa dispersion data are highly suggestive, they do not in themselves constitute the definitive hallmark of a fractional Chern insulator: a fractionally quantized Hall conductance. Obtaining this "smoking gun" requires direct electrical transport measurements—a task that has long been technically challenging in semiconducting TMDs due to contact resistance and disorder. As described in the following section, the development of a new device architecture overcame these limitations, enabling high-fidelity transport studies in twisted $MoTe_2$. The resulting measurements revealed unambiguous quantization of the Hall resistance at fractional values, providing conclusive evidence that moiré $MoTe_2$ hosts a fractional quantum anomalous Hall effect.

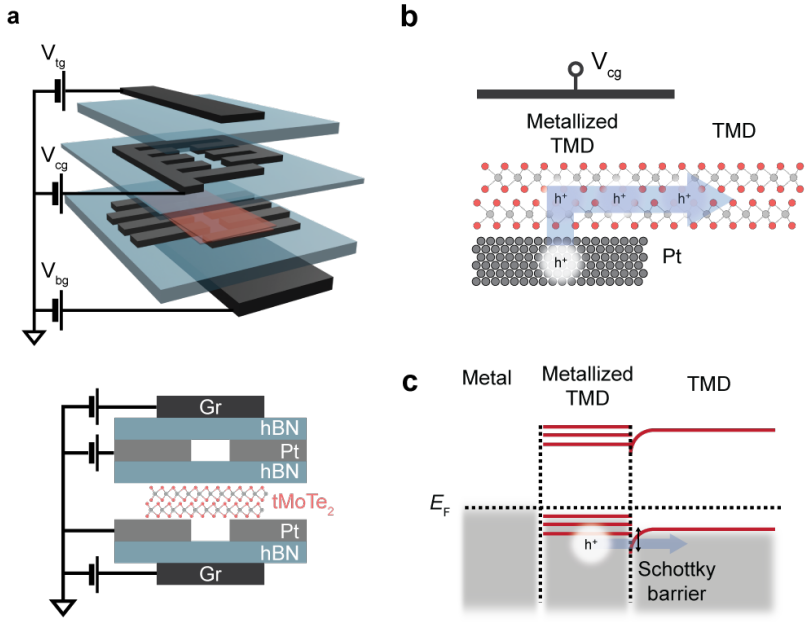

Figure 3.2: Contact engineering and device structure. **a**, Schematic of dual-gated device with top, bottom, and contact gates. **b**, Illustration of the Pt–TMD contact interface. Holes flow from Pt to the metallized TMD and into the intrinsic TMD Hall bar. **c**, Energy diagram of the three regions. Strain in the metallized TMD (due to ∼8 nm contact step height) induces defect-like bands and a Schottky barrier, which is suppressed by heavy hole doping via V_{cg}.

3.3 Device Fabrication and Electrical Measurements

A central challenge in twisted 2D semiconductor devices has been minimizing contact resistance at zero perpendicular electric field [112, 113]. For the first time, we addressed this by incorporating additional local gates to heavily hole-dope the contact regions (carrier density $\sim 10^{13}$ cm^{-2}), enabling low-resistance injection (Fig. 3.2).

The fabrication procedure is as follows. All constituent flakes—hBN, 2H-$MoTe_2$, and graphite—were exfoliated onto heavily doped Si substrates with a thermally grown SiO_2 layer. Candidate flakes were identified under an optical microscope or using AFM and selected based on thickness and cleanliness. The bottom gate stack was assembled using a standard dry polycarbonate (PC) transfer technique. First, an hBN dielectric layer was picked up, followed by a thin graphite bottom gate, and then transferred onto the substrate. Platinum electrodes (8 nm) were patterned via e-beam lithography and deposited using e-beam evaporation to define the Hall bar.

The bottom gate structure underwent contact-mode AFM cleaning before being transferred to a nitrogen-filled glovebox (O_2, $H_2O < 0.1$ ppm). Inside the glovebox, monolayer $MoTe_2$ was mechanically exfoliated and cut with an AFM tip to prepare two halves. A twisted bilayer was then assembled by sequentially picking up one half of the flake, rotating the stage to the desired angle, and collecting the other half using an hBN flake. The twisted bilayer stack was transferred onto the bottom gate stack. Polymer residues were dissolved using molecular-sieve-cleaned chloroform and dichloromethane within the glovebox.

Post-assembly, the device was AFM-cleaned again. Local contact gates (Pt, 8 nm) were patterned to enhance injection efficiency. Additional lithography steps were used to deposit Cr/Au (5/70 nm) for bonding pads. Following another round of AFM cleaning, a graphite/hBN top gate was added and polymer residue was removed in ambient conditions using chloroform.

Following such procedure, we were able to minimize the contact resistance in transition metal dichalcogenide (TMD) moiré heterostructures. As shown in Fig. 3.2c, a Schottky barriers are formed at the interface between metallic contacts and the intrinsic semiconducting TMD channel. These barriers introduce substantial contact resistance, which in turn increases noise in transport measurements and restricts reliable access to low-carrier-density regimes. This limitation is particularly acute near charge neutrality, where most topological and strongly correlated phases emerge in TMD homobilayer systems.

The local contact gate design enables us to tune the electrostatic doping of the TMD beneath the contacts. By applying a large negative voltage to the contact gates (see Fig. 3.2b), the region between the metallized electrode and the intrinsic $MoTe_2$ channel can be selectively hole-doped. This local doping suppresses the Schottky barrier and facilitates the formation of low-resistance, nearly ohmic contacts that remain effective down to dilution refrigerator temperatures ($T \sim 10$ mK).

To evaluate the performance of the contacts, we measured the two-terminal resistance between adjacent electrodes while keeping all other contacts floating, and have reached contact resistance of approximately 10 $k\Omega$ per contact. Although this configuration does not yield the precise contact resistance, it provides an upper bound—approximately twice the actual contact resistance. We found that the two-terminal resistance increases at low hole doping levels, which we attribute to defect-induced scattering in the crystal.

Experiments were carried out in a Bluefors dilution refrigerator equipped with a 9 T supercon-

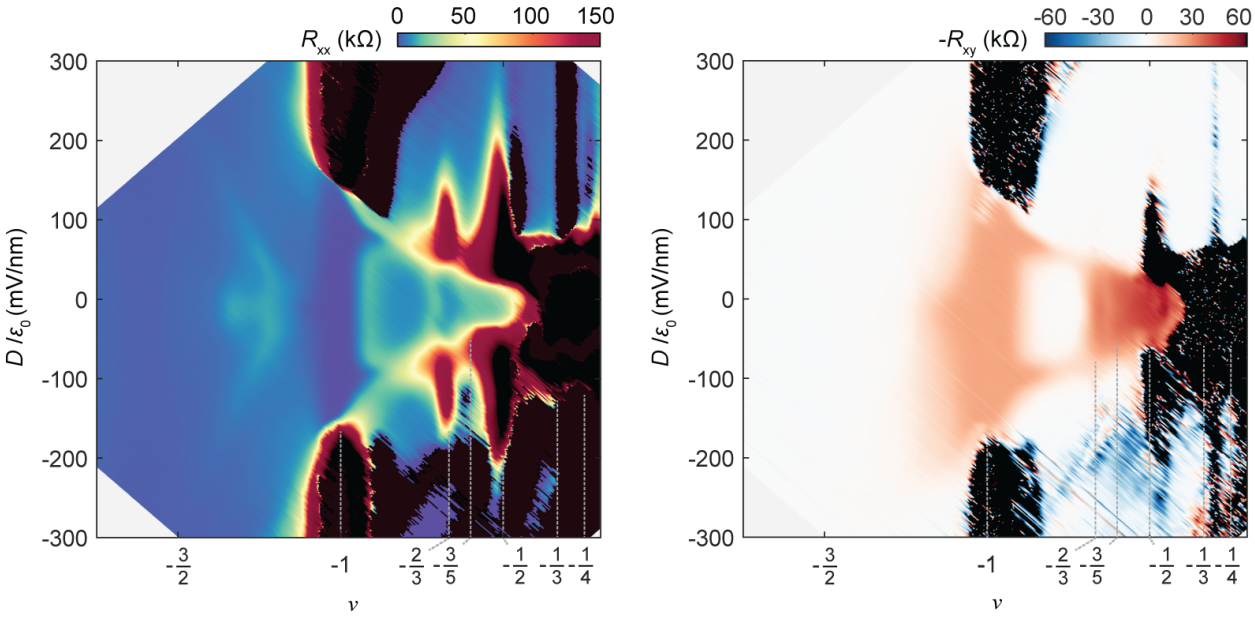

Figure 3.3: Transport Phase Diagram of D(3.7°) **a,** Longitudinal resistance R_{xx} and **b,** Hall resistance R_{xy} at 100 mK as functions of displacement field D/ε_0 and filling factor ν, symmetrized and antisymmetrized with respect to $|\mu_0 H| = 200$ mT .

ducting magnet. The base phonon temperature was approximately 20 mK, while the electronic temperature was estimated to be 80 mK using calibration from graphene devices of comparable geometry.

A Stanford SR830 lock-in amplifier was used to generate and detect all AC signals. Measurements were performed under constant current bias (∼0.2–0.5 nA), applied via a 100 MΩ series resistor. The actual current was monitored using a DL1211 current preamplifier. This approach led to improved magnetic state stability compared to constant voltage configurations.

Four-terminal resistances R_{xx} and R_{xy} were measured using SR560 preamplifiers (input resistance ∼100 MΩ), significantly larger than the typical contact resistance. For two-terminal measurements, an AC voltage of 200–500 μV was applied, and the current was monitored through the drain.

For thermal activation measurements above 4 K, a resistive heater located near the sample was incrementally powered. The local temperature was monitored using a Cernox sensor positioned close to the device. Control experiments using a carbon film sensor mounted on the chip carrier

confirmed that the sample stage temperature differed by no more than 50 mK from the sensor reading.

3.4 Phase Diagram of twisted $MoTe_2$

Figures 3.3a and 3.3b display maps of longitudinal resistance R_{xx} and Hall resistance R_{xy} from device D(3.7°), measured at $T = 100$ mK as functions of carrier density n and displacement field D/ε_0. To reduce hysteresis from gate sweeps, a small out-of-plane magnetic field $\mu_0 H = \pm 200$ mT is applied, with R_{xx} and R_{xy} symmetrized and antisymmetrized accordingly. Regions of high resistance ($R > 1$ MΩ) are marked in black. Several gate-tunable correlated states emerge, notably around $\nu = -1$, $-2/3$, and $-1/2$ near $D/\varepsilon_0 = 0$, where suppressed R_{xx} and enhanced $|R_{xy}|$ signal the presence of topological ground states.

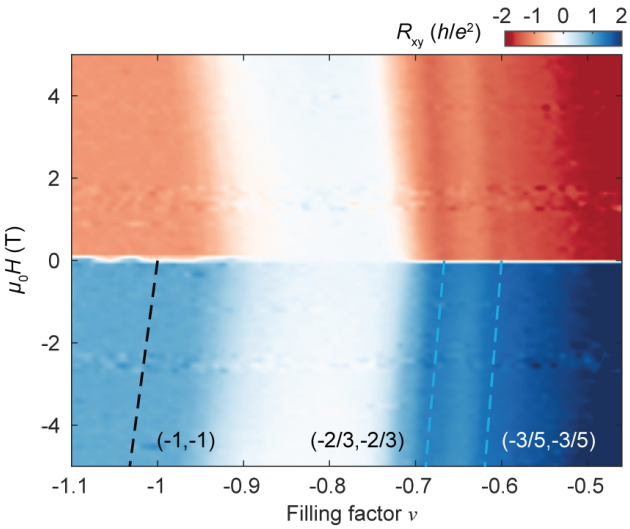

Figure 3.4: Landau fan of R_{xy} at 100 mK. Unsymmetrized Hall resistance R_{xy} plotted as a function of filling factor. The black line marks a $|C| = 1$ quantum anomalous Hall (QAH) state at $\nu = -1$, while the blue lines trace fractional QAH states with $|C| = 2/3$ at $\nu = -2/3$ and $|C| = 3/5$ at $\nu = -3/5$.

The topological nature of these features becomes evident in the field dependence of R_{xy} (Fig. 3.4). The Hall resistance evolves linearly with $\mu_0 H$ for each filling factor, with slopes that match theoretical expectations from the Středa formula for states with Chern numbers $C = -1$, $-2/3$, and $-3/5$. The state at $\nu = -1$ exhibits a broad quantized R_{xy} plateau with slope corresponding to $|C| = 1$, characteristic of a quantum anomalous Hall (QAH) phase. Narrower peaks at $\nu = -2/3$ and $-3/5$ also disperse linearly with magnetic field, consistent with fractional QAH (FQAH) states with $|C| = 2/3$ and $3/5$, respectively. Reversing the sign of $\mu_0 H$ inverts the slope due to magnetization reversal, confirming the Chern nature of these states. These observations are in agreement with earlier trion-based magnetic sensing studies [11].

3.5 *Integer Quantum Anomalous Hall Effect*

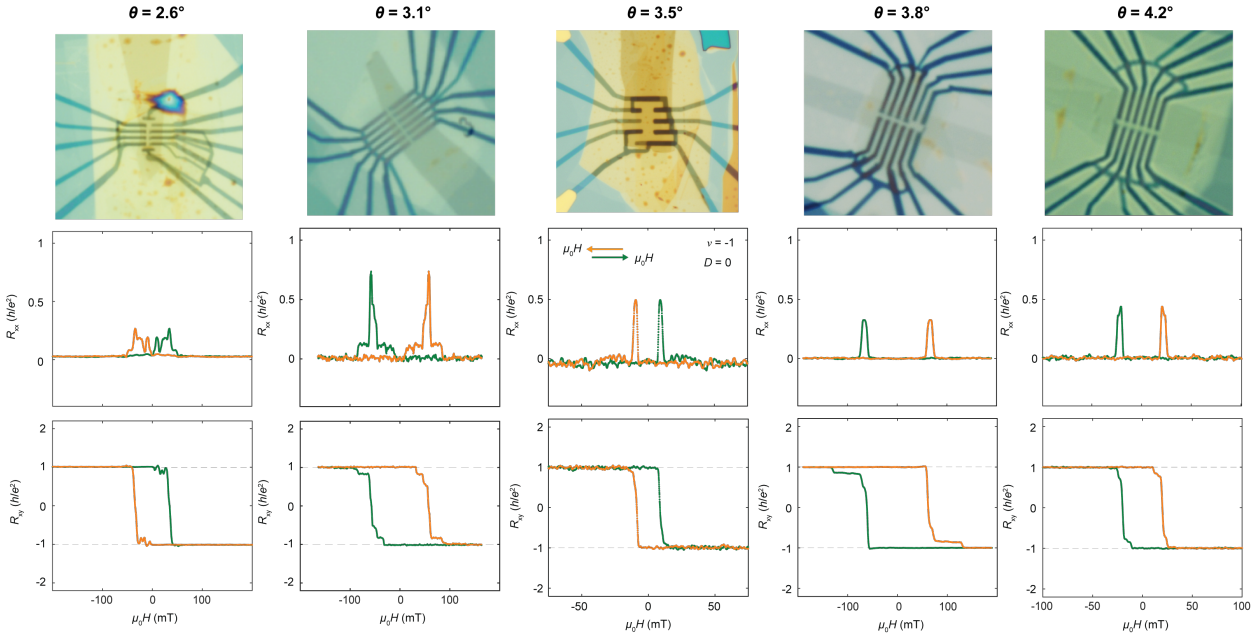

Figure 3.5: Quantum Anomalous Hall Effect at different twist angles Top: Optical images of devices with twist angles ranging from 2.6° to 4.2°. Middle: Longitudinal resistance R_{xx} versus out-of-plane magnetic field $\mu_0 H$ measured at $\nu = -1$ and $D/\varepsilon_0 = 0$, showing sharp domain wall resistance peaks during magnetization reversal. Bottom: Corresponding Hall resistance R_{xy} traces display clear hysteresis and near-quantized plateaus at $\pm h/e^2$.

Figure 3.6 explores the electric-field and temperature dependence of the quantum anomalous Hall (QAH) effect at $\nu = -1$ in device D(3.9°). Panel 3.6c displays R_{xy} and R_{xx} as functions of out-of-plane magnetic field $\mu_0 H$ for several electric field values D/ε_0 at $T = 100$ mK. At $D/\varepsilon_0 = 0$, a clear hysteresis loop is observed in R_{xy}, quantized at $\pm h/e^2$ (with measured value $0.9998 \pm 0.0136 \times h/e^2$ at $\mu_0 H = 0$), and accompanied by a vanishing R_{xx}. Sharp resistance peaks in R_{xx}, occurring when R_{xy} switches sign, mark the coercive field $\mu_0 H_c \approx 84$ mT. These are definitive signatures of a QAH state. The QAH phase is robust over a wide range of twist angles (2.6°–4.2°) (Fig. 3.5).

As D/ε_0 increases, the QAH plateau weakens and eventually collapses beyond a critical electric field D_c/ε_0. To quantify this, panel 3.6b shows antisymmetrized R_{xy} and symmetrized R_{xx} at fixed $|\mu_0 H| = 200$ mT as a function of D/ε_0. A sharp transition is seen near $D_c/\varepsilon_0 \approx 150$ mV/nm, where

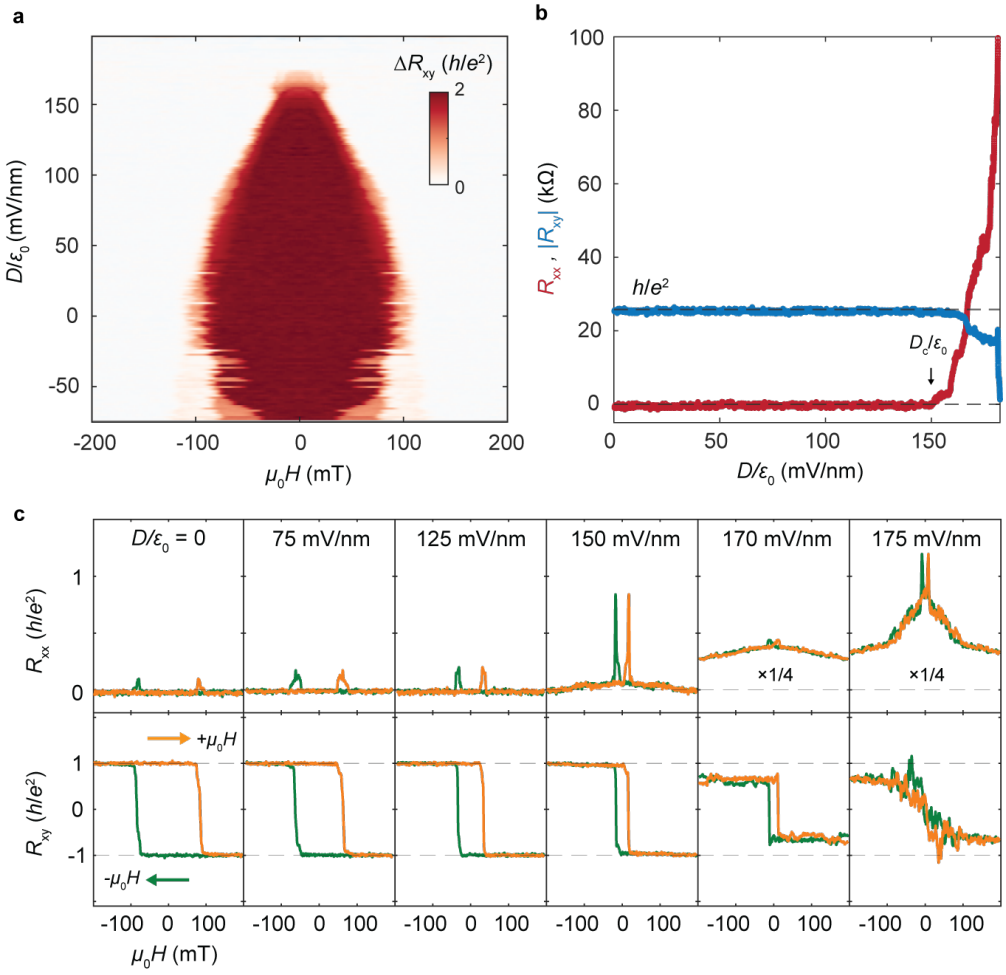

Figure 3.6: Electric-field dependence of QAHE at $\nu = -1$ in D(3.9°). **a,** ΔR_{xy} vs magnetic field and electric displacement field D/ε_0. The ΔR_{xy} signal diminishes near 150 mV/nm, indicating a transition out of the QAH regime. **b,** $|R_{xy}|$ (blue) and R_{xx} (red) versus D/ε_0 at 100 mK, extracted at $|\mu_0 H| = 200$ mT after antisymmetrization and symmetrization, respectively. **c,** Magnetic field sweeps of R_{xx} and R_{xy} at selected D/ε_0 values.

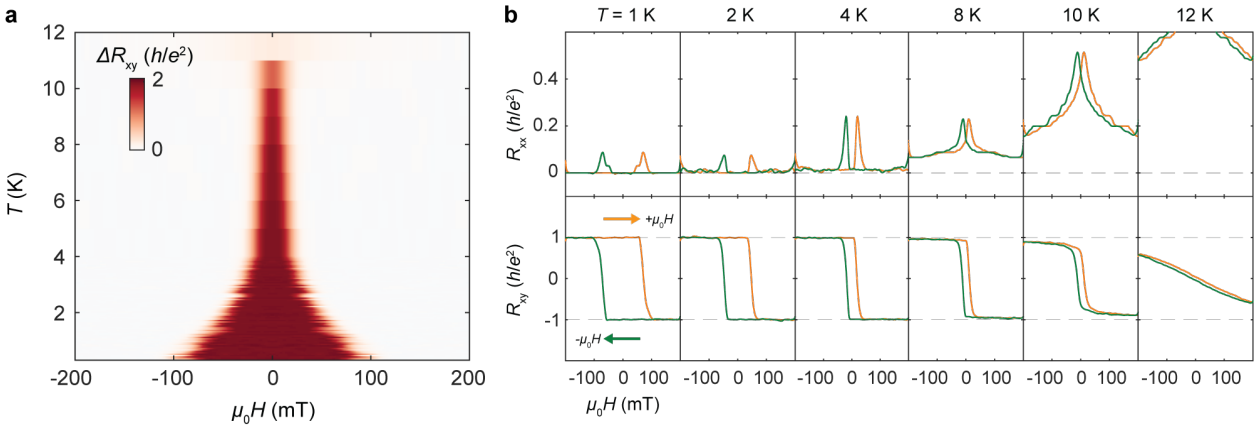

Figure 3.7: Thermal robustness of the QAH effect at $\nu = -1$. **a,** Hysteretic Hall resistance ΔR_{xy} as a function of temperature and magnetic field. **b,** Magnetic field sweeps of R_{xx} and R_{xy} at selected temperatures. The signal remains close to the quantized value h/e^2 up to 8 K, indicating strong thermal stability of the QAH phase.

R_{xy} drops and R_{xx} rises steeply, signaling a transition to a topologically trivial insulating phase. Similar behavior is confirmed in D(3.52°), including persistent ferromagnetism in the trivial phase from RMCD measurements, and is further supported by Hartree-Fock calculations and theoretical studies [54, 114].

Panel 3.7a plots the hysteresis amplitude ΔR_{xy} as a function of temperature and magnetic field. Notably, ΔR_{xy} remains nearly quantized up to 8 K, suggesting a Curie temperature around 12 K. The temperature-electric field map of R_{xx} in panel 3.8a, c highlights the transition near $D_c/\varepsilon_0 \approx 150$ mV/nm, with the resistance rising sharply in the trivial regime.

We extract the thermal activation gap Δ from Arrhenius fits to the R_{xx} data, shown in panel 3.8d. In the QAH regime ($D/\varepsilon_0 < D_c/\varepsilon_0$), R_{xx} follows $R \propto e^{-\Delta/2k_BT}$ at low temperatures. In contrast, beyond the transition, in the trivial insulator, R_{xx} follows $R \propto e^{+\Delta/2k_BT}$, reflecting thermally activated conductivity. Near the critical point, R_{xx} is temperature-independent and of order h/e^2, consistent with behavior expected at topological phase transitions [115, 116].

The extracted gap Δ decreases gradually with increasing D/ε_0 within the QAH state and then closes and reopens across the transition, indicating a topological phase transition driven by electric field. Additional gap analysis from R_{xy} data is presented in Fig. 3.8b,e,f.

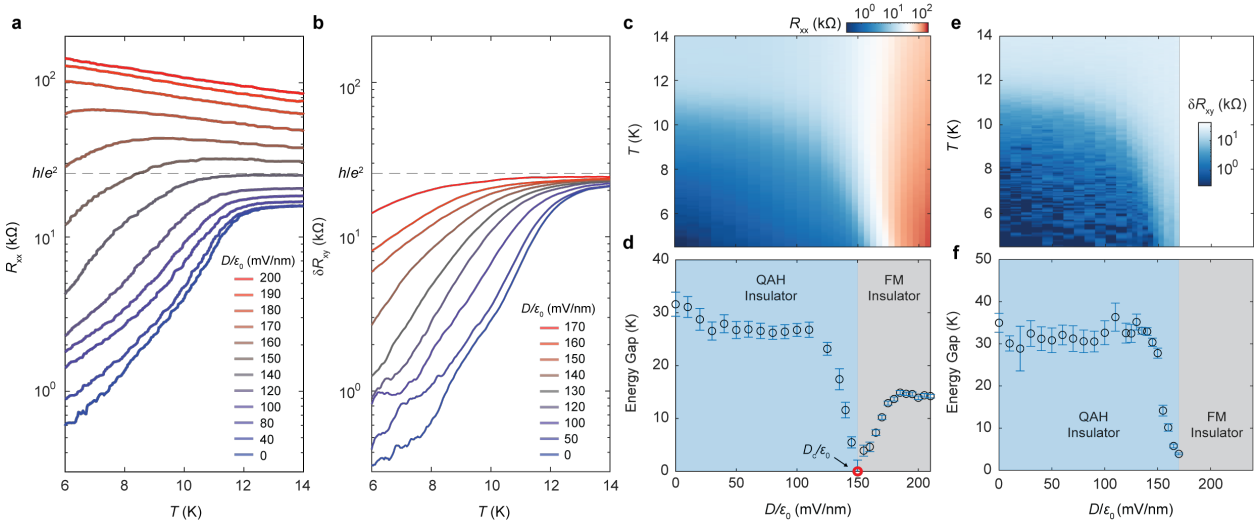

Figure 3.8: Electric-field-driven topological phase transition at $\nu = -1$. **a,** Temperature dependence of unsymmetrized R_{xx} at selected D/ε_0, measured at $\mu_0 H = 100$ mT to suppress domain fluctuations. **b,** Temperature evolution of $\delta R_{xy} = |h/e^2 - R_{xy}|$ from antisymmetrized Hall data at ±100 mT. **c,** Color map of R_{xx} as a function of temperature and D/ε_0, showing a transition from a QAH to a trivial insulator beyond ∼150 mV/nm. **d,** Activation gap extracted from R_{xx} in (c) reveals a closing and reopening of the energy gap, indicative of a continuous topological transition. **e,** Map of δR_{xy} corroborates a transition near 150 mV/nm. **f,** Activation gap derived from (e), peaking at ∼35(2) K near $D/\varepsilon_0 = 0$, consistent with the R_{xx}-derived estimate of 32(2) K.

3.6 Fractional Quantum Anomalous Hall States

We next examine the fractional quantum anomalous Hall (FQAH) states, with all measurements taken from device D(3.7°). Figure 3.9a presents R_{xx} and R_{xy} as functions of out-of-plane magnetic field $\mu_0 H$ at $\nu = -2/3$, measured at $T = 500$ mK and $D/\varepsilon_0 = 0$. The Hall resistance R_{xy} shows a hysteresis loop centered at $\mu_0 H = 0$, quantized within 1% to $\pm 3h/2e^2$, with a coercive field $\mu_0 H_c \approx 20$ mT. The longitudinal resistance R_{xx} remains below 1 kΩ, aside from small peaks coinciding with magnetization reversal. These features confirm the realization of a Chern number $C = -2/3$ FQAH phase.

Figure 3.9b displays analogous behavior at $\nu = -3/5$, where R_{xy} transitions between $\pm 5h/3e^2$ within 3% accuracy, again accompanied by low R_{xx}. This identifies a $C = -3/5$ FQAH state.

These FQAH phases are tunable with vertical electric field. For clarity, we focus on the $-2/3$

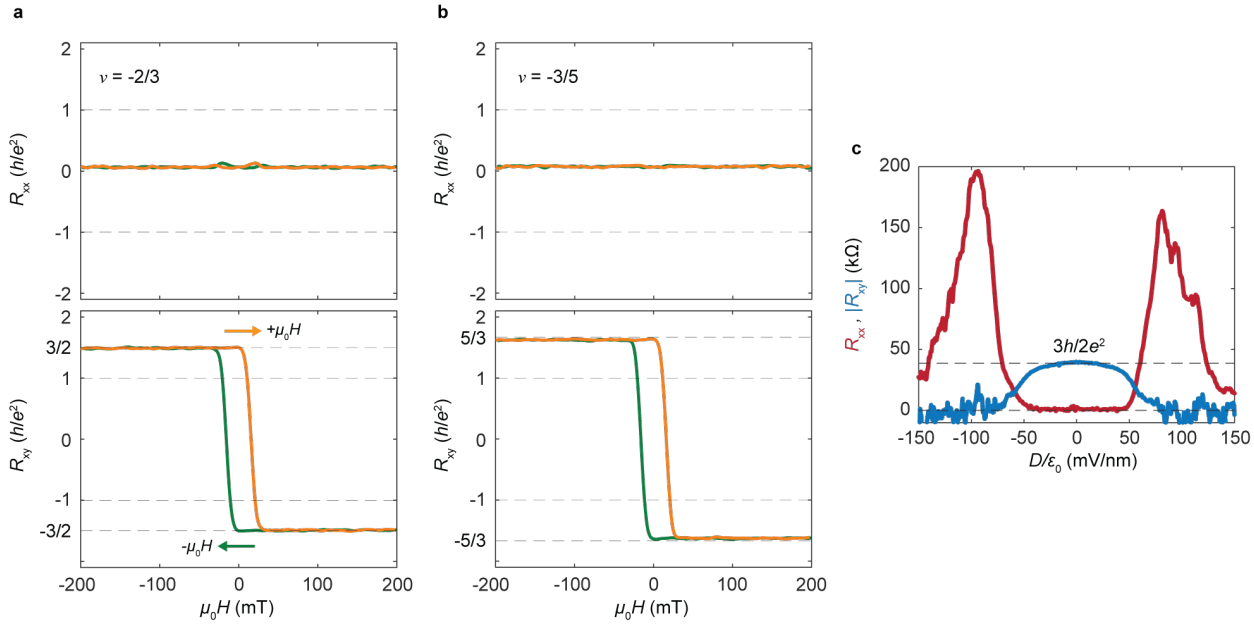

Figure 3.9: Fractional Quantum Anomalous Hall Effect in D(3.7°). **a,b,** R_{xx} and R_{xy} versus $\mu_0 H$ at $\nu = -2/3$ (a) and $-3/5$ (b), measured at $T = 500$ mK and $D/\varepsilon_0 = 0$. **c,** Symmetrized R_{xx} (red) and antisymmetrized $|R_{xy}|$ (blue) at $\mu_0 H = \pm 50$ mT as functions of D/ε_0 at $T = 100$ mK.

state. In Fig. 3.9c, R_{xy} and R_{xx} are shown as functions of D/ε_0 at fixed $|\mu_0 H| = 50$ mT and $T = 100$ mK. A sharp degradation of the quantized R_{xy} is observed beyond $|D_c/\varepsilon_0| \approx 20$ mV / nm, with complete suppression by $|D/\varepsilon_0| \gtrsim 80$ mV/nm. Simultaneously, R_{xx} rises from near zero, reaching a peak ($\sim$ 100–200 kΩ) in the intermediate region, before decreasing to 20–30 kΩ as D/ε_0 increases past 150 mV/nm. This evolution implies an electric-field-induced transition from the FQAH phase to a trivial insulating regime, followed by a crossover to a more conductive (metallic) state. These transitions are also discernible in Fig. 3.3. Further theoretical modeling is needed to clarify the nature of these field-driven phases.

To extract the energy gap of the $-2/3$ FQAH state, we study its temperature dependence. Figure 3.10a shows the evolution of R_{xx} and R_{xy} with $\mu_0 H$ at various temperatures. Figure 3.10b plots the hysteresis amplitude ΔR_{xy} as a function of field and temperature. As temperature rises above 1 K, the zero-field quantization weakens, though R_{xy} remains quantized under small finite field ($>$ 20 mT) up to approximately 2 K. Above this, quantization rapidly degrades and the

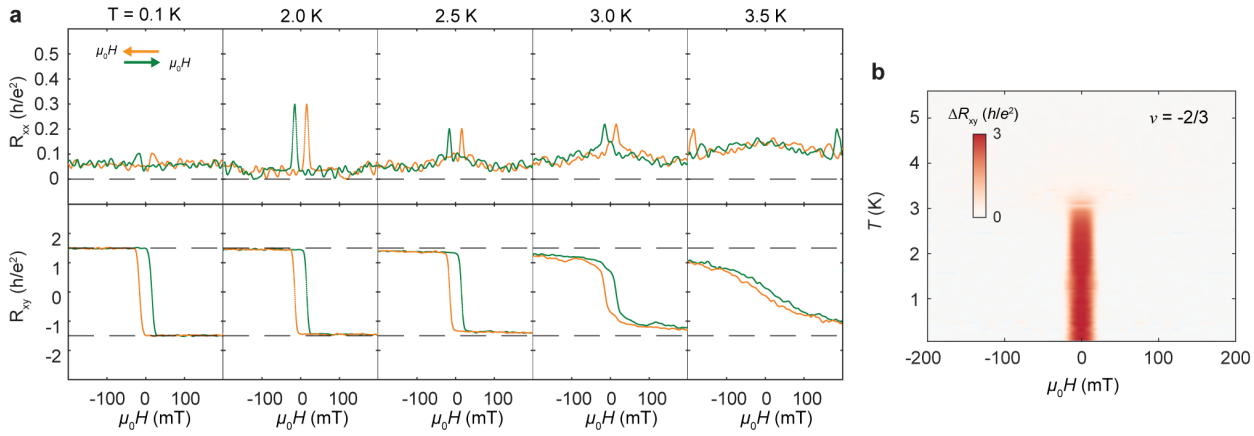

Figure 3.10: Temperature dependence of $\nu = -2/3$ state. **a,** R_{xx} and R_{xy} versus $\mu_0 H$ at selected T, showing persistent quantization of R_{xy} near 2 K. **b,** Hysteretic Hall signal ΔR_{xy} as a function of temperature and magnetic field.

hysteresis vanishes beyond 4 K.

We estimate the thermal activation gap Δ using Arrhenius fits to R_{xx} (Fig. 3.11), modeled as $R(T) = R_0 e^{-Delta/2k_BT}$. For $\nu = -2/3$, we obtain $\Delta = 23(7)$ K. A consistent gap value is extracted from the temperature dependence of $\delta R_{xy} = |3h/2e^2 - R_{xy}|$. Applying the same analysis to the $-3/5$ state (Fig. 3.11) yields a smaller gap of $\Delta = 15(3)$ K. These results align well with previous optical spectroscopy [11] and exact diagonalization calculations [117].

3.7 Anomalous Hall State at Half-Filling

We now focus on the transport characteristics near half-filling, using data from device D(3.7°). Similar results were obtained from device D(3.9°). Figures 3.12a and b display R_{xx} and R_{xy} as functions of out-of-plane magnetic field $\mu_0 H$, measured at $\nu \approx -1/2$, temperature $T = 500$ mK, and zero displacement field ($D/\varepsilon_0 = 0$). The Hall resistance R_{xy} exhibits a hysteretic loop with a coercive field $\mu_0 H_c \approx 16$ mT, and reaches values near $\pm 2h/e^2$ at $\mu_0 H = 0$, while R_{xx} remains low, around 2 kΩ.

Figure 3.12c presents the temperature dependence of R_{xx} and R_{xy} near $\nu = -1/2$ (symmetrized and antisymmetrized at $|\mu_0 H| = 50$ mT, respectively). As temperature increases, the R_{xy} value near $2h/e^2$ progressively diminishes, vanishing above $T \approx 4$ K. At the same time, R_{xx}, which initially

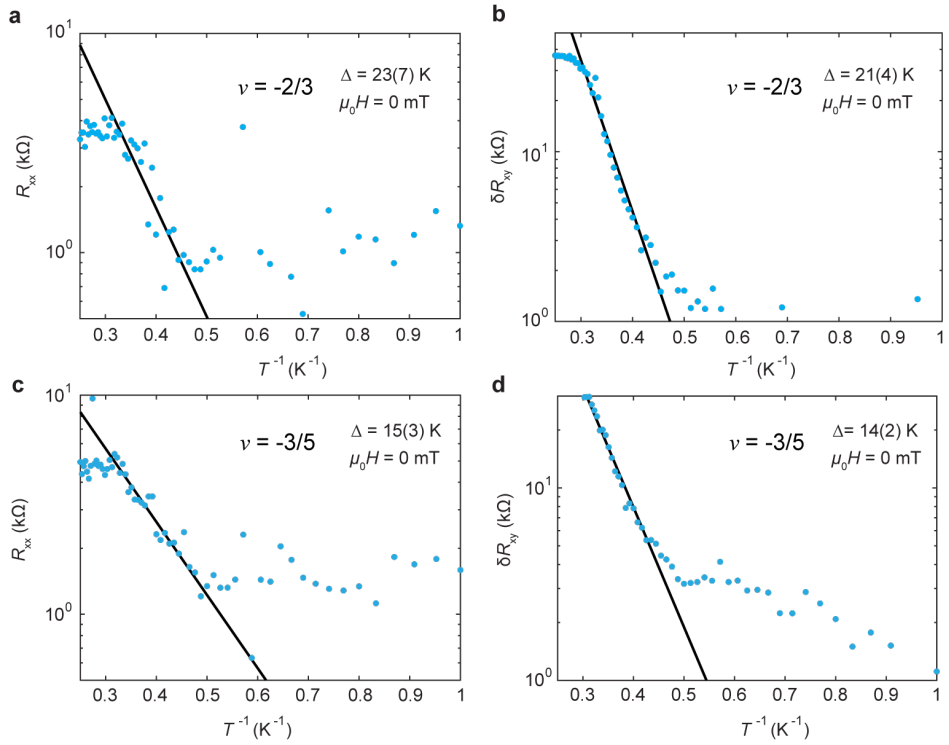

Figure 3.11: Activation gap analysis of FQAH states in D(3.7°). **a**, Arrhenius plot of R_{xx} at $\nu = -2/3$ with an exponential fit $R = R_0 e^{-\Delta/2k_B T}$. **b**, Corresponding fit of $\delta R_{xy} = (3h/2e^2 - R_{xy})$ yields a comparable gap. Extracted activation energies from R_{xx} and R_{xy} are 23(7) K and 21(4) K, respectively. **c**, Similar analysis for $\nu = -3/5$ using R_{xx} and $\delta R_{xy} = (5h/3e^2 - R_{xy})$, giving energy gaps of 15(3) K and 14(2) K.

sits near 2 kΩ, begins to rise significantly around 2 K. These observations point to a temperature-driven crossover from a spontaneously polarized anomalous Hall phase to a topologically trivial high-temperature regime. The hysteretic component ΔR_{xy}, also fades out above 4 K, further supporting this conclusion.

To examine the density dependence, Fig. 3.13 shows symmetrized R_{xx} and antisymmetrized R_{xy} versus ν at $T = 100$ mK, using a fixed field of $|\mu_0 H| = 50$ mT. Clear plateaus in R_{xy} are observed at $\nu = -2/3$ and $-3/5$, consistent with quantization at $3h/2e^2$ and $5h/3e^2$, respectively. Notably, these quantized values occur at the peaks of broad humps in $R_{xy}(\nu)$, while near $\nu = -1/2$, R_{xy} exhibits a linear evolution with ν, crossing approximately $2h/e^2$. Across this region, R_{xx} remains low, typically below a few kΩ.

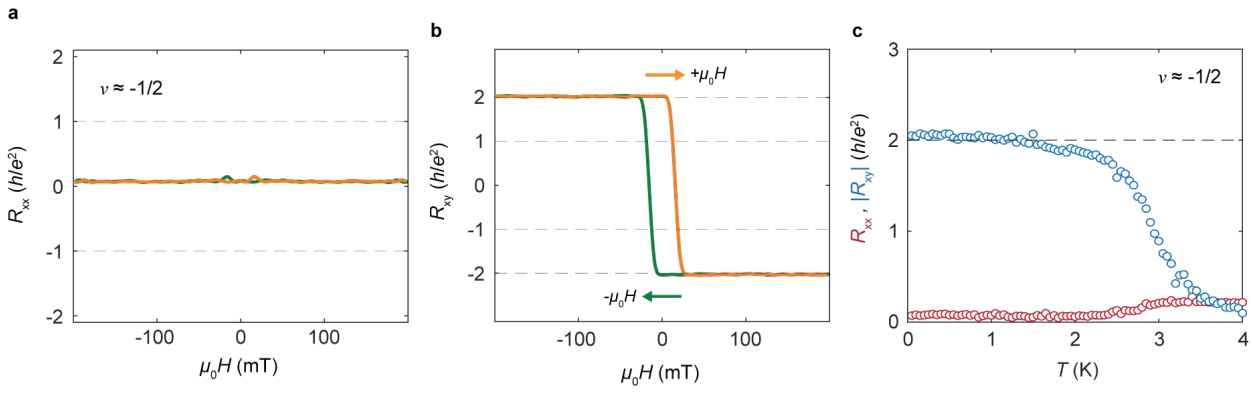

Figure 3.12: Anomalous Hall response near half-filling in device D(3.7°). All measurements were performed at $D/\varepsilon_0 = 0$. **a,b,** R_{xx} (a) and R_{xy} (b) as functions of $\mu_0 H$ at $\nu \approx -1/2$ and $T = 500$ mK. **c,** Temperature-dependent R_{xx} (symmetrized) and R_{xy} (antisymmetrized) at ±50 mT show a phase transition between 2–4 K.

The approximately linear dependence of R_{xy} on filling near $\nu = -1/2$, combined with the absence of an insulating signature in R_{xx}, indicates a compressible electronic phase. This interpretation is reinforced by the absence of any optical gap features in earlier trion sensing experiments [11]. The observed behavior is reminiscent of composite Fermi liquid (CFL) phases near half-filling in the lowest Landau level of conventional two-dimensional electron gases [118, 22, 119, 120], and aligns with recent theoretical predictions suggesting a zero-field CFL state as the likely ground state at $\nu = -1/2$ in twisted $MoTe_2$ [54, 55].

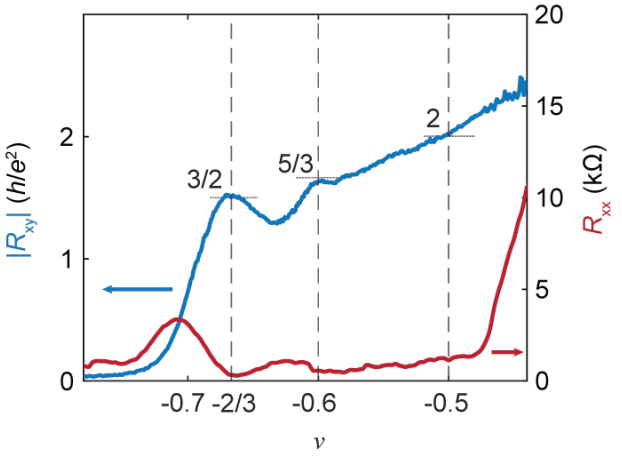

Figure 3.13: Filling factor dependent transport at $D/\varepsilon_0 = 0$. Symmetrized R_{xx} (red) and antisymmetrized R_{xy} (blue) versus filling factor ν, measured at $\mu_0 H = \pm 50$ mT and $T \approx 100$ mK.

3.8 Conclusion and Perspectives

To conclude, our transport measurements offer direct evidence for both integer ($C = -1$) and fractional ($C = -2/3$ and $C = -3/5$) quantum anomalous Hall states in rhombohedral-stacked twisted $MoTe_2$ bilayers. These states were previously inferred through thermodynamic analyses of optical spectroscopy data [11], but our results provide unambiguous electrical confirmation. Moreover, we identify a novel anomalous Hall phase near half-filling, which exhibits a similar electric-field-driven transition as the $C = -2/3$ FQAH state, hinting at underlying similarities in their origin.

Whether this half-filled anomalous Hall state corresponds to a zero-field composite Fermi liquid (CFL) remains an open question. Theoretical work has proposed that such a CFL phase [55] may exhibit intrinsic commensurability oscillations in transport near $\nu = -1/2$, analogous to the magnetoresistance oscillations seen in conventional Landau level systems subjected to external periodic modulations [121, 122]. In moiré materials, these effects would uniquely reflect the superlattice periodicity, offering a potential experimental fingerprint for the CFL regime in zero field.

Looking ahead, continued advancements in material quality and contact engineering should open the door to a deeper exploration of this rich system. Twisted $MoTe_2$ bilayers appear poised to serve as a highly tunable platform for probing the complex interplay between electron correlations, band topology, and spontaneous magnetism. These developments also hold promise for realizing novel topological and spintronic device architectures based on moiré engineering.

Chapter 4

LOCAL PROBE OF FRACTIONAL CHERN INSULATOR EDGE STATES

Fractional quantum Hall (FQH) states are distinguished by an incompressible two-dimensional bulk and chiral edge channels that transport fractionally charged quasiparticles [21, 6, 25, 101, 123]. While indirect signatures of quasiparticle fractionalization have been observed through charge-sensing [124, 125, 126], shot noise measurements [127, 27], and scanning gate microscopy [128], direct spatial visualization of FQH edge modes and the surrounding insulating bulk remains a major experimental challenge. Such imaging is essential for probing the microscopic nature of edge conduction [129] and may play a key role in advancing platforms for topological quantum computing via anyonic braiding [130].

Earlier studies using magnetoplasmon resonance [131] provided indirect insight into edge dynamics, and more recently, synthetic quantum systems have enabled real-space imaging of chiral edge transport [132, 133, 134, 135]. However, these bosonic analogs lack the fully gapped bulk necessary to test bulk-boundary correspondence in electron-based FQH systems.

Microwave impedance microscopy (MIM) has emerged as a powerful local technique capable of mapping conductivity with nanoscale spatial resolution [136]. MIM has been used to image edge conduction in several topological phases, including integer quantum Hall systems [137, 138, 139, 140], quantum spin Hall insulators [141], and quantum anomalous Hall states [142]. Nonetheless, imaging edge states in *fractional* regimes remains experimentally prohibitive due to the stringent requirements for realizing FQH states—namely high magnetic fields and ultra-low temperatures.

The recent discovery of the fractional quantum anomalous Hall effect (FQAHE) [11, 12, 13, 14, 143] provides a promising new route to access fractional edge physics under more accessible experimental conditions. In particular, FQAHE systems such as twisted bilayer $MoTe_2$ (t-$MoTe_2$) display nearly quantized Hall resistance and strongly suppressed longitudinal resistance in the $v = -2/3$ FCI phase at temperatures exceeding 2 K and without external magnetic fields [13]. These characteristics make FQAHE platforms ideal candidates for real-space imaging of fractional

edge conduction.

Yet several fundamental questions remain unanswered. While R_{xx} is greatly suppressed in transport, it remains finite—likely due to intrinsic disorder such as moiré inhomogeneity [144]. Signatures of topological phase transitions have been inferred from global transport [13, 14], but their microscopic origins remain poorly understood. Furthermore, the existence, morphology, and coherence of fractional edge modes have not yet been confirmed locally.

In this work, we address these open questions using a scanning microwave impedance microscope with spatial resolution better than 100 nm. This technique allows us to directly visualize edge conduction in a zero-field FCI, revealing how disorder, topological phase transitions, and edge structure manifest in real space.

4.1 Exciton-Resonant MIM for Dual-Gated Moiré Devices

To probe local conductivity in dual-gated twisted $MoTe_2$ (t-$MoTe_2$) devices, we developed an exciton-resonant microwave impedance microscopy (ER-MIM) technique, designed to overcome limitations associated with conventional MIM in gated structures. In standard setups, the presence of a metallic or thick dielectric top gate often screens the microwave signal, significantly reducing sensitivity to the underlying sample. Our approach mitigates this issue through both instrumental advancements and careful sample architecture.

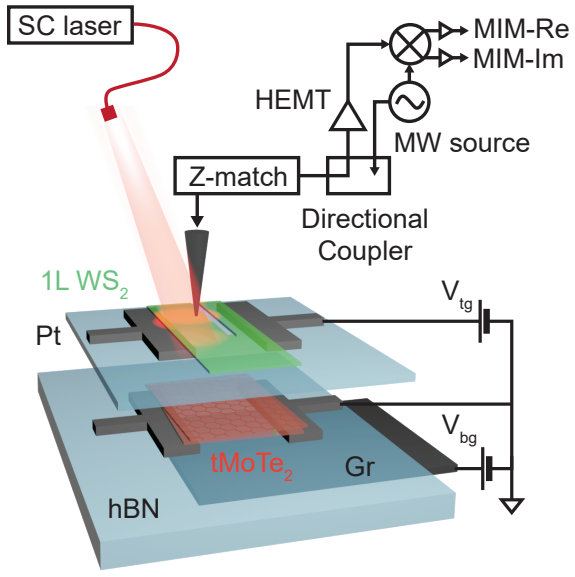

Figure 4.1: Exciton-resonant microwave impedance microscopy setup. The device is partitioned into dual-gated regions 1 (left) and 2 (right), with an ungated central region lacking a top gate.

The measurement schematic is illustrated in Fig. 4.1a. A microwave signal is delivered through a transmission line impedance-matched to a metallic scanning probe tip [145, 136, 146, 71], enabling high-sensitivity, near-field imaging. The sample comprises a 3.2°-twisted $MoTe_2$ homobilayer encapsulated between hexagonal

boron nitride (hBN) layers, with a graphite bottom gate and an optically transparent top gate.

Crucially, the top gate is realized using a monolayer of tungsten disulfide (WS_2), which is both atomically thin and optically active. When illuminated with light near the WS_2 A-exciton resonance ($\sim$2.2 eV), photoexcitation induces a local photogating and photoconductive effect [147], thereby tuning the electrostatic potential of the underlying device without significantly attenuating the microwave field. This design enables direct MIM sensing of the $MoTe_2$ layer even in the presence of a top gate.

As shown in Fig. 4.2a, we use atomic force microscopy (AFM) lithography to etch a narrow trench through the WS_2 top gate, creating two spatially distinct regions—region 1 (left) and region 2 (right)—with independently addressable gate potentials.

All measurements are conducted at zero magnetic field using a 6.5 GHz excitation frequency. Our analysis focuses on the imaginary component of the reflected microwave signal (MIM-Im), which is sensitive to local dielectric screening and sample conductivity. This contrast channel is particularly well suited for detecting edge modes and inhomogeneous conductivity in correlated electron systems.

4.2 Sample Fabrication

Single crystals of 2H-phase $MoTe_2$ were synthesized via a tellurium self-flux method. High-purity Mo powder (pre-annealed under H_2) and elemental Te were mixed at a molar ratio of approximately 1:200, then sealed under vacuum in a quartz ampoule. The sealed tube was heated to 750 °C in a box furnace, followed by slow cooling to 500 °C at a controlled rate of 1 K/hour. Residual Te flux was removed by vacuum annealing the resulting crystals at 500 °C for 24 hours.

For device assembly, hexagonal boron nitride (hBN) and graphite flakes were mechanically exfoliated onto Si/SiO_2 substrates and identified using contrast-enhanced optical microscopy and atomic force microscopy (AFM). The bottom gate structure was assembled using a poly(bisphenol A carbonate) (PC)-based dry transfer method. First, an hBN flake (serving as the bottom gate dielectric) was picked up, followed by a graphite flake (bottom gate electrode), then transferred onto a high-resistivity Si substrate. After transfer, the PC film was removed by successive rinses in chloroform and dichloromethane.

The bottom gate pattern was defined using electron beam lithography. Electrical contacts were

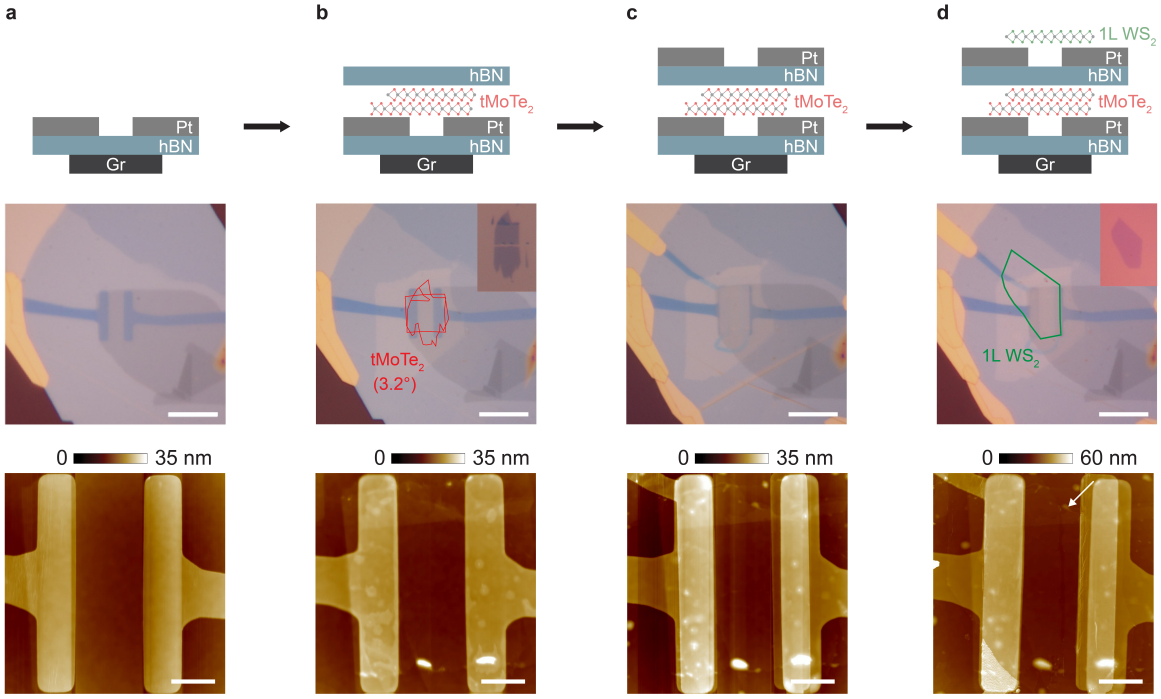

Figure 4.2: Device fabrication workflow. Each row shows, from top to bottom: schematic, optical image, and AFM image. Scale bars: 10 μm (optical), 2 μm (AFM).

deposited by e-beam evaporation: Ti/Pt (2/5 nm) for electrodes, and Cr/Au (5/60 nm) for contact pads.

Monolayer $MoTe_2$ flakes were exfoliated inside a glovebox under low O_2 and H_2O conditions (<0.1 ppm). To minimize strain, a single $MoTe_2$ monolayer was split into two halves using an AFM tip prior to stacking. The twisted bilayer structure was fabricated by sequentially picking up one half with a hBN flake (serving as the top dielectric), rotating the stage by a controlled twist angle ($\sim$3.2°), and then picking up the second half. The entire heterostructure was deposited onto the prepatterned bottom gate.

Top gate metallization was completed in a subsequent lithography step, followed by metal evaporation (Ti/Pt and Cr/Au) to define electrodes and contact pads. A monolayer WS_2 flake was then picked up and transferred onto the device as the top gate layer. Notably, the use of monolayer WS_2 enables optical gating without screening microwave signals, a key requirement for

exciton-resonant MIM imaging.

Throughout the fabrication process, contact-mode AFM was used extensively to clean the sample surface and eliminate polymer residue and interfacial bubbles. During the final cleaning step, the AFM tip was used to etch a narrow channel through the WS_2 top gate, spatially separating domains with different local gate potentials and enabling the stabilization of distinct Chern insulating phases within a single device.

4.3 Bulk Conductivity Mapping with ER-MIM

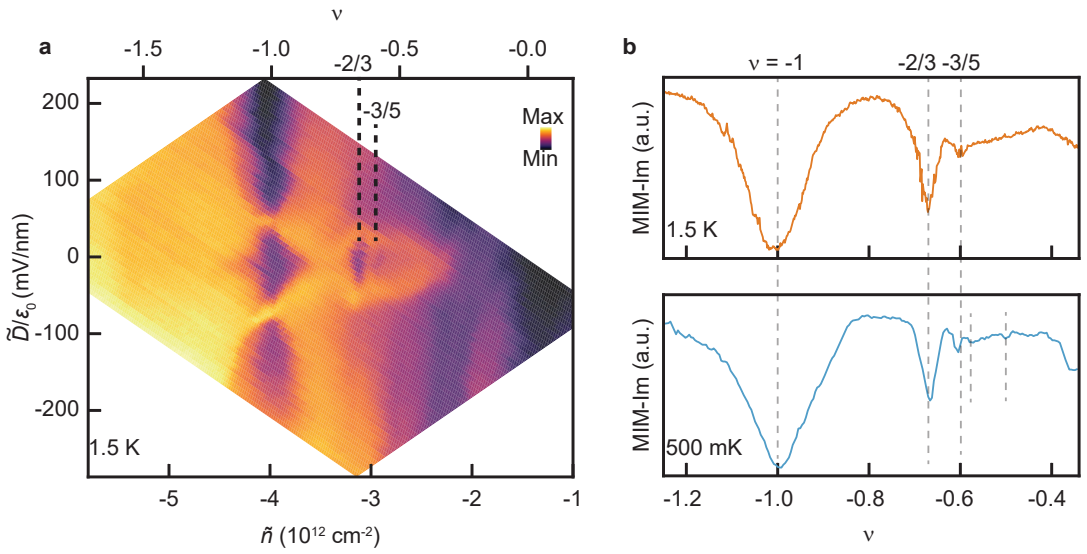

Figure 4.3: Dual gate map of MIM. **a**, MIM-Im signal measured at 1.5 K as a function of electric field $\tilde{D}/\varepsilon_0$ and carrier density $\tilde{n}$ in region 1. **b**, MIM-Im signal versus ν at 1.5 K (orange, top) and at 500 mK with zero displacement field (blue, bottom).

The high spatial resolution of ER-MIM enables direct measurement of the bulk conductivity in fractional Chern insulators (FCIs), independent of edge contributions—an inherently challenging task for conventional transport techniques. Figure 4.3a displays the MIM-Im signal as a function of carrier density $\tilde{n}$ and interlayer displacement field $\tilde{D}/\epsilon_0$, both of which are estimated using a geometric capacitance model. These data were acquired in region 1 of the device (marked by the white star in Fig. 4.4a) at a temperature of 1.5 K.

In this color map, darker tones indicate insulating behavior (weaker microwave screening), while brighter regions correspond to higher local conductivity. The resulting phase diagram reveals a complex interplay of correlated states. Near zero interlayer field, where the system approximates a symmetric honeycomb moiré potential, we observe prominent insulating features centered at filling factors $\nu = -1$, $-2/3$, and $-3/5$, consistent with the formation of Chern and fractional Chern insulating phases. In contrast, near $\nu = -1/2$, the system remains relatively conductive, likely reflecting a metallic state. At even lower fillings, such as $\nu = -1/3$, insulating behavior re-emerges.

At large values of $|\tilde{D}/\epsilon_0|$, carriers are polarized into a single layer, transforming the moiré potential from a honeycomb to a triangular lattice. This results in re-entrant insulating behavior, particularly at commensurate fillings such as $\nu = -1$, and with additional insulating regions near $\nu = -2/3$ and $-1/2$. An intermediate bright band of conductivity appears at moderate displacement fields, separating the insulating states in the symmetric and polarized limits—indicative of a phase transition involving electronic delocalization.

The bulk phase diagram obtained from ER-MIM closely mirrors the Chern insulator signatures previously identified via longitudinal resistance (R_{xx}) measurements [13]. In transport studies, both the QAH state at $\nu = -1$ and the $-2/3$ FCI exhibit significant suppression of R_{xx}, suggesting dissipationless edge transport atop an insulating bulk. Our local conductivity maps directly confirm this picture. At $\nu = -1/2$, transport reveals finite but reduced R_{xx}, consistent with the moderately enhanced MIM-Im signal here, indicative of a partially conducting, likely metallic bulk. This regime has been linked to composite Fermi liquid behavior in moiré flat bands [54, 55].

As the interlayer field is increased, R_{xx} rises sharply at $\nu = -1$, $-2/3$, and $-1/2$, suggesting transitions to charge-ordered states such as Mott or generalized Wigner crystals [62, 63, 67]. Our MIM measurements not only corroborate this insulating behavior but also resolve an intermediate, conducting regime, consistent with gap closing during a topological-to-trivial phase transition.

Beyond phase mapping, ER-MIM allows spatially resolved spectroscopy in regions less affected by disorder. Figure 4.3b shows the MIM-Im signal as a function of ν at zero displacement field, taken at 1.5 K (orange) and 500 mK (blue). Well-defined dips in conductivity are observed at $\nu = -1$, $-2/3$, and $-3/5$, signaling the presence of robust insulating phases. Notably, at the lower temperature of 500 mK, an additional dip emerges near $\nu = -4/7$, which is absent at higher temperatures, suggesting a smaller gap and enhanced thermal fragility of this state.

A shallow but discernible dip also appears at $\nu = -1/2$, hinting at possible incipient ordering. These weaker features—particularly those near $\nu = -4/7, -1/2$, and at lower fillings—are found to vary spatially across the sample, and are only resolved in cleaner regions. These position-dependent signatures point to the critical role of disorder and motivate further studies using devices with improved uniformity.

4.4 Imaging of Edge States in the Integer Chern Insulator Regime

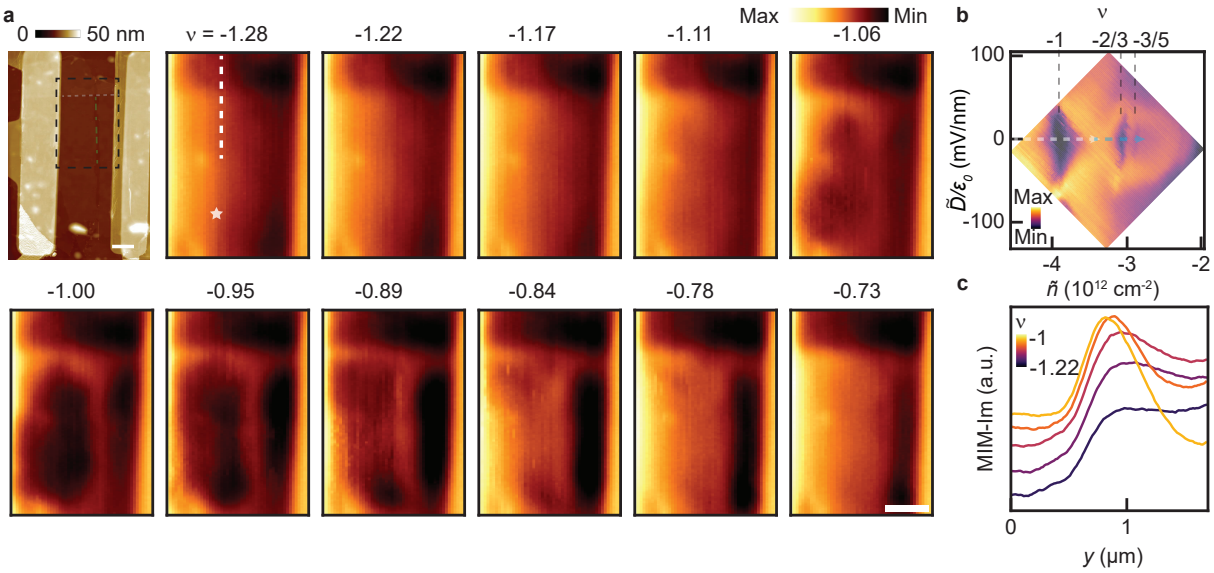

Figure 4.4: Microwave imaging of QAH edge states. **a**, AFM image of the device (left), with etched edges (gray dashed line), interface (green dashed line), and MIM scan area (black rectangle). Scale bar: 1 μm. Right: MIM-Im maps at selected filling factors ν, showing increasing bulk-edge contrast near $\nu = -1$. Scale bar: 1 μm. **b**, MIM-Im signal versus $\tilde{D}/\varepsilon_0$ and $\tilde{n}$ at 1.5 K, measured at the white star in panel a. **c**, MIM-Im line profiles (vertically offset) averaged over 0.7 μm along the dashed line in panel **a**.

By scanning the metallic microwave probe across the sample surface, ER-MIM allows spatial mapping of local conductivity, enabling direct visualization of edge conduction in Chern insulating phases. Figure 4.4a presents spatial MIM-Im maps taken at a sequence of filling factors ranging from $\nu = -1.28$ to -0.73. The measurement trajectory in parameter space is indicated by the white arrow in Fig. 4.4b, corresponding to a fixed location in region 1 (marked by the white star

in Fig. 4.4a). The topmost panel of Fig. 4.4a shows an atomic force microscopy (AFM) topograph of the scanned area, with the black dashed square outlining the field of view. The lower portion of this scan, demarcated by a grey dashed line, covers the t-$MoTe_2$ device area.

At high doping ($\nu = -1.28$), the MIM-Im signal is bright and spatially uniform across the scanned region, consistent with a metallic bulk. As the filling factor approaches $\nu = -1$, the MIM-Im signal in the interior diminishes while bright, conductive features emerge along the sample boundary—hallmarks of a quantum anomalous Hall (QAH) state [142]. The spatial profile indicates an insulating bulk surrounded by one-dimensional conducting edge channels. Reducing the doping further beyond $\nu = -1$ results in a reappearance of the metallic state across the bulk. Comparable behavior is observed in region 2 of the sample. A consistently bright feature along the boundary between regions 1 and 2 is attributed to the absence of the WS_2 top gate in that interface, resulting in a local variation in carrier density.

To quantitatively assess the evolution of edge conduction with doping, we extract spatial line profiles of the MIM-Im signal across the sample edge. These cuts, shown in Fig. 4.4c, are taken along the dashed line indicated in the second panel of Fig. 4.4a. Two key observations emerge: first, the width of the edge-localized MIM-Im peak narrows as ν approaches -1, consistent with the emergence of localized chiral edge states. Notably, the full width at half maximum (FWHM) remains $\sim$500 nm—substantially broader than the spatial resolution of the tip, indicating a physical broadening rather than instrumental limitation.

Second, the MIM-Im amplitude at the edge is maximized near the QAH state, exceeding that of the bulk metallic phase. This enhancement and broadening are consistent with the excitation of gapless edge magnetoplasmon (EMP) modes [148], which arise from collective charge oscillations confined to the one-dimensional edge channel. The observed spatial extent of the MIM-Im peak matches well with the expected EMP decay length, which can approach the system size in low-dissipation chiral edge states.

4.5 Imaging Edge Modes in Fractional Chern Insulators

To investigate the edge conduction behavior in fractional Chern insulating (FCI) phases, we perform spatially resolved MIM-Im measurements across a range of filling factors within the Chern band. Figure 4.5a displays spatial MIM-Im maps taken along the trajectory indicated by the blue arrow in

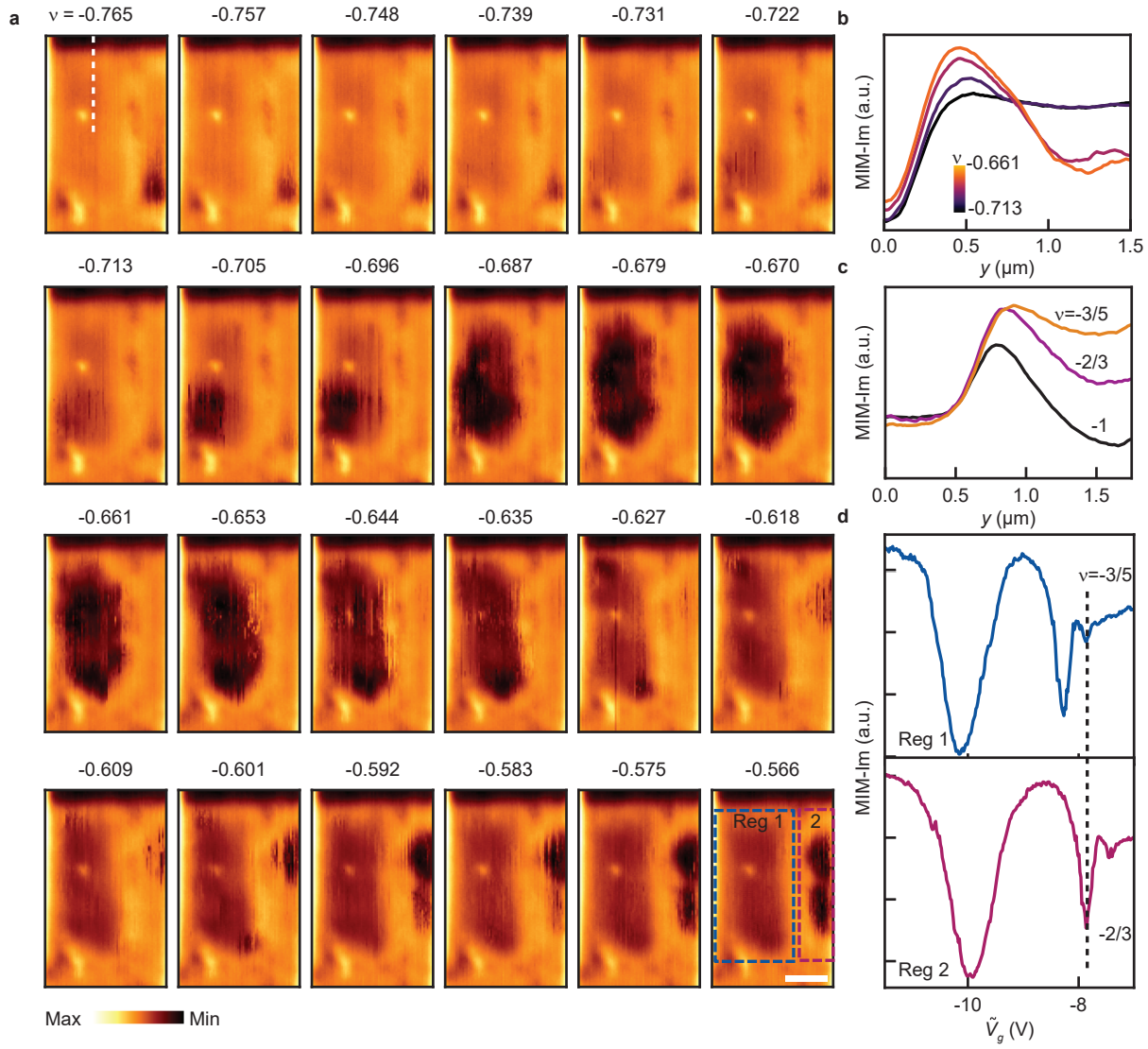

Figure 4.5: Imaging fractional edge states. **a**, MIM-Im maps at selected filling factors, showing emerging edge-bulk contrast near $\nu = -2/3$ and $-3/5$. Scale bar: 1 μm. **b**, MIM-Im linecuts averaged over 0.3 μm along the dashed line in previous figure (Region 1), across $\nu = -0.661$ to -0.713. **c**, Edge linecuts at $\nu = -1$, $-2/3$, and $-3/5$, averaged over 0.5 μm. **d**, MIM-Im signal versus effective gate voltage at two locations in distinct regions at 1.5 K, revealing coexistence of $\nu = -2/3$ and $-3/5$ FCI states.

Fig. 4.4b. Starting from slight underdoping of the QAH state ($\nu \lesssim -1$), the entire sample exhibits bright MIM-Im contrast, indicative of metallic conductivity. As the system approaches fractional fillings, such as $\nu = -2/3$, the interior becomes dark while the edges remain bright, revealing an insulating bulk coexisting with conductive boundary channels—direct evidence of an edge state associated with the $-2/3$ FCI. A similar contrast pattern is observed at $\nu = -3/5$, reinforcing its identification as a distinct fractional phase with edge conduction.

To analyze the evolution of edge localization with doping, Fig. 4.5b shows spatial MIM-Im line profiles extracted along the same edge region for different filling factors, ranging from $\nu = -0.71$ (black) to $-2/3$ (orange). As the system transitions into the $-2/3$ FCI regime, the bulk signal diminishes and the edge response becomes more pronounced, resembling the behavior seen in QAH states [149, 150]. These results demonstrate the formation of well-localized, conductive edge states even in the absence of an external magnetic field.

We compare the structure and strength of the edge signals across several topological phases. Figure 4.5c plots MIM-Im profiles for $\nu = -1$ (black), $-2/3$ (purple), and $-3/5$ (yellow) under identical measurement conditions. All three states display comparable spatial widths of the edge peak, on the order of hundreds of nanometers, suggesting the presence of collective edge magnetoplasmon (EMP) modes [148]. Notably, the peak amplitudes differ between states, hinting at differences in edge charge dynamics and internal structure.

The frequency and strength of EMP resonances are governed by the Hall conductance (σ_{xy}), edge confinement potential, and the characteristic length scale of edge localization. At the fixed probe frequency of 6.5 GHz, MIM-Im is primarily sensitive to the lowest-order EMP mode. In a single-channel model, one expects MIM-Im$_{\nu=-1}$ < MIM-Im$_{-2/3}$ < MIM-Im$_{-3/5}$, based on both decreasing σ_{xy} and increasing σ_{xx} screening. However, our data show that the MIM-Im amplitudes for $-2/3$ and $-3/5$ are nearly identical, deviating from this simple ordering. This discrepancy suggests the inadequacy of a non-interacting single-edge picture.

Given the sharp physical edge in our device, strong inter-channel coupling and disorder-induced scattering are expected [151, 152]. These effects are well captured by the Kane-Fisher-Polchinski (KFP) model [153], which describes fractional edges as a composite of counterpropagating charge and neutral modes. In the case of $\nu = -2/3$, this corresponds to a downstream charge channel with conductance $2e^2/3h$ and an upstream neutral mode. The presence of this neutral mode could

explain the absence of a compressible stripe detectable by MIM (which has ∼100 nm resolution), as well as the altered edge amplitude.

Our ability to detect edge states with high spatial fidelity is enabled by the uniformity and large thermodynamic gaps in twisted $MoTe_2$ [154], which support robust bulk-edge correspondence. Interestingly, we observe spatial coexistence of distinct FCI phases in different sample regions. As shown in Fig. 4.5d, gate sweeps from two nearby areas (dashed boxes in Fig. 4.4a) reveal that one region hosts the $-3/5$ FCI while the other stabilizes the $-2/3$ state, likely due to slight variations in gate coupling. The interface between these regions exhibits complex MIM-Im contrast, consistent with a strongly scattered interfacial state.

These observations highlight the potential for engineering sharp domain boundaries between different anyonic orders at zero magnetic field. With future device designs, such as split top gates enabling local control of filling, it may be possible to intentionally stabilize topologically distinct FCI regions and probe the 1D interface states between them [155]. Such interfaces open exciting opportunities to study inter-edge scattering between Laughlin and Halperin states, topological entanglement, and even engineer non-Abelian anyon braiding schemes in moiré materials [26].

4.6 Electric-Field-Driven Evolution of Edge States

To explore the behavior of edge conduction across topological phase transitions, we examine the effect of a perpendicular electric field on the microwave response of various Chern and fractional Chern insulator states. Figure 4.6a presents the MIM-Im amplitude as a function of displacement field D/ϵ_0 for the $\nu = -1$ (purple), $-2/3$ (orange), and $-3/5$ (red) states. In all cases, the MIM signal is suppressed at both small and large values of $|D/\epsilon_0|$, but exhibits a distinct enhancement in the intermediate field regime.

This non-monotonic behavior reflects the sequence of transitions from a topologically nontrivial insulating state (QAH or FCI), to a metallic phase as the gap closes, and finally into a correlated trivial insulator at high fields. These field-induced transitions reflect changes in layer polarization and moiré symmetry, which alter the effective band topology and electron correlations.

Figure 4.6b shows representative spatial MIM-Im images at selected electric fields for the $\nu = -2/3$ FCI state. In the FCI regime near $D/\epsilon_0 = 0$, the bulk is dark while the edges appear bright, consistent with an incompressible interior supporting chiral boundary conduction. As the

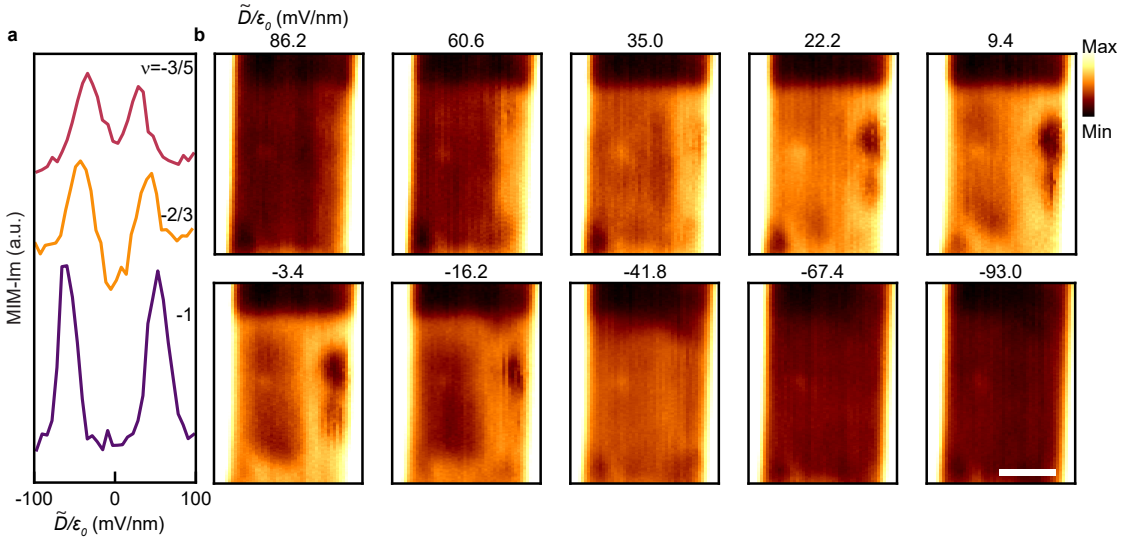

Figure 4.6: **Edge state evolution across an electric field-driven topological transition.** **a**, MIM-Im signal versus effective displacement field $\tilde{D}/\epsilon_0$ at $T = 1.5$ K for the $\nu = -1$ (purple), $-2/3$ (yellow), and $-3/5$ (red) Chern insulator states. Curves are vertically offset for clarity. **b**, Spatial MIM-Im maps at $\nu = -2/3$ taken at varying D/ϵ_0, showing progressive development of edge-localized contrast as the FCI state forms. Scale bar: 1 μm.

field increases, the signal brightens across the device, indicating entry into a metallic phase with enhanced bulk conductivity. At even larger field magnitudes, the signal becomes uniformly dim again, signifying a re-entrant correlated insulator in the layer-polarized regime.

This sequence of bright–dim–bright–dim contrast in MIM-Im provides a direct, spatially resolved fingerprint of topological and symmetry-breaking phase transitions. The stark difference between the localized edge signal in the FCI regime and the fully insulating high-field phase highlights the topological origin of the edge conduction. In particular, the edge-localized MIM response disappears in the trivial insulator, affirming that the observed fractional edge states arise from bulk-boundary correspondence, rather than trivial edge accumulation.

A similar electric field evolution is observed for the $\nu = -1$ QAH state, where sharp edge features persist until the system transitions to a fully layer-polarized insulator. In contrast, at $\nu = -1/2$, the system behaves differently. At $T = 1.5\,\mathrm{K}$, the MIM signal transitions from a compressible or weakly compressible state at low field to an incompressible phase at large $|D/\epsilon_0|$, consistent with

emergent charge ordering in the triangular lattice limit.

These measurements demonstrate the utility of ER-MIM in tracking the evolution of bulk and edge states through topological and correlation-driven transitions. The ability to resolve such changes spatially provides powerful evidence for bulk-boundary correspondence and highlights the distinct field-tunable nature of FCIs and their metallic or insulating counterparts in moiré platforms.

4.7 Conclusion

By combining exciton-resonant microwave impedance microscopy (ER-MIM) with a monolayer WS_2 top gate, we demonstrate the first MIM-compatible platform for dual-gated moiré devices operating entirely at zero magnetic field. This technical advance allows spatial imaging of correlated topological phases—specifically, quantum anomalous Hall (QAH) and fractional Chern insulator (FCI) states—in twisted bilayer $MoTe_2$. In both regimes, we observe clear signatures of insulating behavior in the bulk coexisting with conducting edge channels, providing direct, real-space evidence of bulk–boundary correspondence in the fractional quantum anomalous Hall regime.

These findings are further reinforced by field-tunable imaging across topological phase transitions. ER-MIM captures the closure and reopening of energy gaps as the system evolves from a Chern insulator to a correlated trivial insulator via an intermediate metallic state, validating the topological origin of the observed edge states.

Comparative analysis between integer and fractional edge responses—along with differences among fractional states—reveals that the FCI edge likely comprises multiple interacting channels, consistent with theoretical models such as the Kane–Fisher–Polchinski picture. Our spatial maps also uncover nuanced features inaccessible to bulk transport, including spatial domains of distinct anyonic order and the presence of weak or fragile fractional states in locally cleaner regions.

Altogether, our results establish ER-MIM as a versatile tool for probing the microscopic structure of topological states in moiré systems and pave the way for future studies of edge reconstruction, domain wall physics, and ultimately the controlled creation of anyonic braiding geometries in fractional quantum anomalous Hall platforms.

Chapter 5

FERROMAGNETISM AND TOPOLOGY OF HIGHER CHERN BANDS

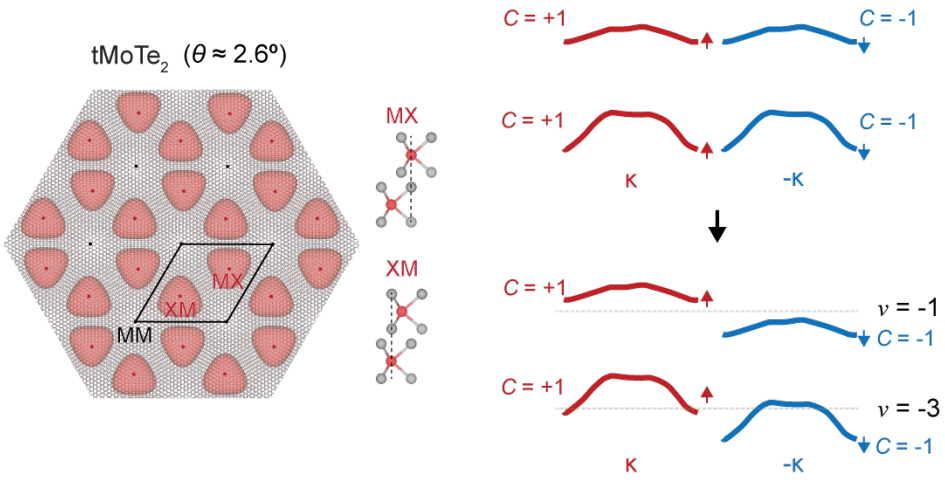

Figure 5.1: Interaction-induced ferromagnetism in the second Chern band. **a,** Moiré lattice of 2.6° twisted $MoTe_2$. At half-filling, holes localize on MX and XM, forming a honeycomb network with direct exchange-driven magnetism. **b,** Top: Non-interacting Chern bands with spin–valley degeneracy and opposite Chern numbers at $+K$ (red) and $-K$ (blue). Bottom: At $\nu = -1$ and -3, interactions lift the degeneracy, yielding spontaneous spin polarization.

In the moiré superlattice of twisted bilayer $MoTe_2$ ($tMoTe_2$), recent theoretical developments have unveiled a rich hierarchy of minibands with nontrivial topology, particularly beyond the lowest Chern band [47, 110, 156, 157, 158, 57, 159]. These higher moiré bands, shaped by the underlying skyrmion-like layer pseudospin textures and electrostatic landscape, exhibit Chern numbers that vary sensitively with twist angle, interaction strength, and band-mixing effects. While the first moiré band is understood to host topological order analogous to the lowest Landau level (LLL), the structure of the second Chern band is qualitatively distinct and opens new possibilities for correlated states, including even-denominator and non-Abelian phases [160, 161, 162, 163, 164, 165, 166, 167, 168, 169].

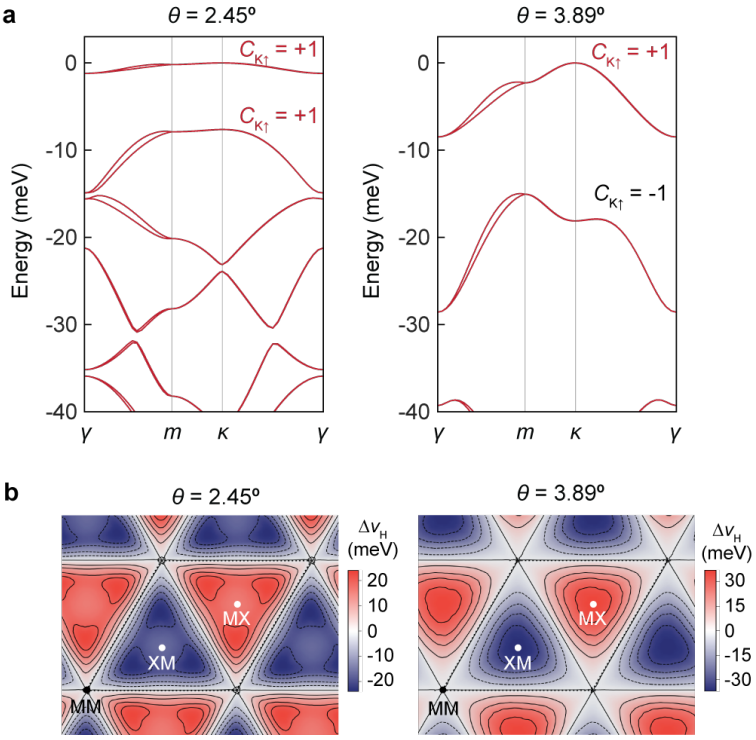

Figure 5.2: DFT band structure and moiré potential evolution with twist angle. **a**, First-principles band structure of $tMoTe_2$ at 2.45° and 3.89°, showing that while the first moiré miniband at the K valley has $C = +1$ in both cases, the second band switches from $C = +1$ to $C = -1$. **b**, Calculated electrostatic potential difference Δv_H between layers. The orbital centers shift from MM to MX/XM sites as θ increases, inverting the Chern number of the second moiré band.

The topological character of these higher bands is a direct consequence of the spatial modulation in the layer pseudospin effective magnetic field $\vec{h}_{\text{eff}}(\vec{r})$, which defines the real-space Berry curvature and controls the emergent band topology. Crucially, in the second moiré miniband, both the quantum geometry and interaction profiles differ significantly from those in the first Chern band, leading to altered energetics for spontaneous symmetry breaking. In particular, the second band often features reduced Berry curvature uniformity and twist-angle-dependent band topology.

Figure 5.1 summarizes the origin of ferromagnetism in the second Chern band and band schematic in $tMoTe_2$. At half-filling of the second Chern band (e.g., $\nu = -3$), carriers predominantly localize on the high-symmetry MX and XM sites of the moiré unit cell, forming an effective honeycomb network. The resulting direct exchange interactions between localized holes yield spontaneous spin polarization and interaction-induced ferromagnetism. Notably, the strength of such ordering is reduced compared to that in the first Chern band (e.g., $\nu = -1$), due to enhanced screening and interband mixing.

A particularly intriguing aspect of the second Chern band is its sensitivity to twist angle. First-principles calculations indicate that while the first moiré miniband retains a consistent topological index ($C = +1$) across a wide range of θ, the second band undergoes a topological inversion as

θ is tuned. Hartree-Fock calculations suggest that such transition occurs due to changes in the interlayer electrostatic potential $\Delta v_H(\vec{r})$, which shifts the orbital center of the wavefunctions from MX/XM sites towards MM sites as the twist angle decreases, as shown in Fig. 5.2.

DFT analysis [157] places the critical twist angle θ_c for this topological transition near 2.6°. At $\theta = 2.45°$, the second moiré band exhibits $C = +1$; at $\theta = 3.89°$, it flips to $C = -1$. Additional calculations at intermediate angles confirm this inversion trend and underscore the tunability of band topology via moiré geometry.

The implications of this twist-angle-driven topological transition are twofold. First, it enables the exploration of opposite-sign Chern bands within a single material platform, thus allowing one to study the dependence of interaction-driven symmetry breaking on band topology. Second, it opens the door to realizing even-denominator FCIs at half-filling of the second Chern band, where the Chern index and flatness ratio can be tuned to optimize the stabilization of non-Abelian phases.

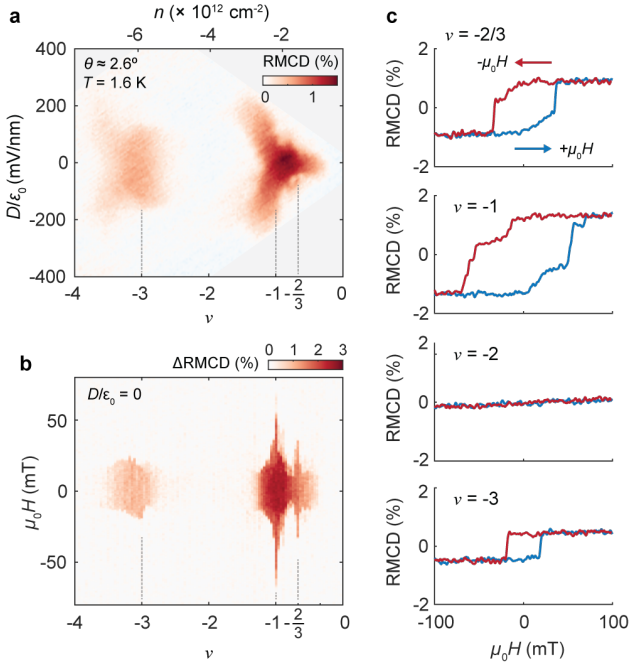

Figure 5.3: Magnetic hysteresis and stability across filling factors. **a,** RMCD signal versus filling factor ν and displacement field D/ε_0 at $\mu_0 H = 50$ mT and $T = 1.6$ K, with carrier density n on the top axis. **b,** Hysteresis amplitude (ΔRMCD) vs. ν and $\mu_0 H$ at zero displacement field. **c,** Field-dependent RMCD at selected ν values, showing hysteresis loops.

The remainder of this chapter focuses on the analysis of the magnetism and topological transitions within the second moiré Chern band. These insights provide the necessary framework to understand experimental observations and guide the search for exotic fractionalized states beyond the Abelian Jain sequence.

5.1 Spontaneous Ferromagnetism in the Higher Flat Band

To probe interaction-driven magnetism in moiré bands, we performed reflective magnetic circular dichroism (RMCD) measurements on a twisted $MoTe_2$ device with a twist angle of 2.6°. Figure 5.3a

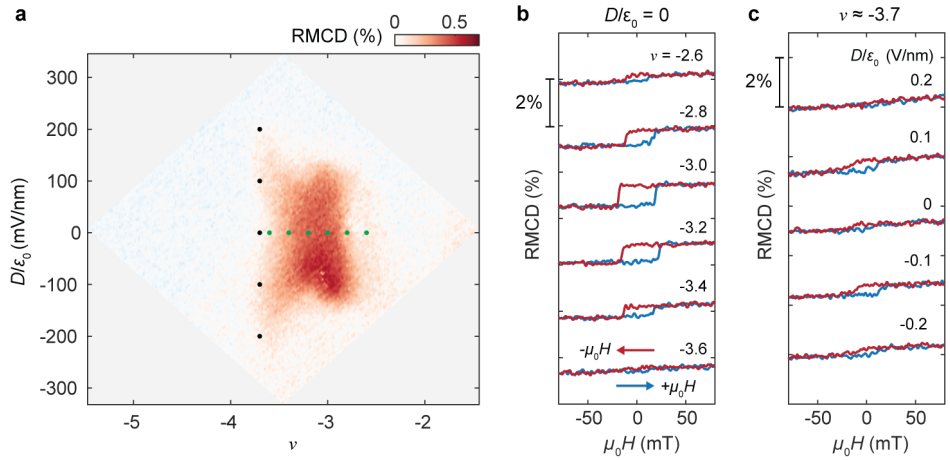

Figure 5.4: Ferromagnetism near $\nu = -3$. **a,** RMCD versus ν and D/ε_0 at $T = 1.6$ K and zero field, showing a wing-like magnetic feature. **b,** RMCD versus $\mu_0 H$ at fixed $D/\varepsilon_0 = 0$ for selected ν (green dots in **a**). **c,** Field sweeps at $\nu \approx -3.7$ for varying D/ε_0 (black dots in **a**).

displays the RMCD signal mapped over carrier filling ν (defined as the negative number of holes per moiré unit cell) and perpendicular displacement field D/ε_0, acquired at a base temperature of $T = 1.6$ K under a weak out-of-plane magnetic field $\mu_0 H = 50$ mT. The applied field stabilizes the RMCD signal, as magnetic fluctuations at zero field lead to erratic switching and hinder reliable density sweeps.

In line with previous studies [11, 12, 53], a pronounced RMCD response is observed at $\nu = -1$, where the lowest Chern band in each valley is half-filled. This state spontaneously breaks time-reversal symmetry through valley polarization. The top two panels of Fig. 5.3c present hysteresis loops of the RMCD signal obtained by cycling $\mu_0 H$ at $\nu = -1$ and $\nu = -2/3$, respectively. The presence of clear hysteresis confirms robust ferromagnetic order at both filling factors. In contrast, at $\nu = -2$, the RMCD signal and its field dependence vanish entirely. This absence is consistent with full occupation of both $\pm K$ Chern bands, where valley degeneracy precludes any symmetry breaking or magnetic ordering.

Strikingly, a second magnetic dome emerges near $\nu = -3$, corresponding to half-filling of the second moiré miniband. A finite RMCD signal develops in this regime, and field sweep measurements (Fig. 5.3c) exhibit clear hysteresis, providing unambiguous evidence of spontaneous ferromagnetism.

This state is stabilized across a broad electric field window and manifests as a pair of "wings" in the ν–D/ε_0 parameter space (Fig. 5.4)—features phenomenologically similar to those previously observed near $\nu = -1$. The recurring structure suggests that both magnetic regimes may arise from a common underlying mechanism.

As mentioned above, doped carriers in this regime predominantly occupy MX and XM high-symmetry sites, forming a honeycomb lattice with direct exchange-mediated magnetism. As the electric field is tuned, the system becomes increasingly layer-polarized. The magnetic phase boundary, including the emergence of the wings, can be understood as arising from the competition between intra-layer Coulomb repulsion and interlayer charge transfer energy. This field-induced modulation reshapes the exchange interactions and sets the boundaries of ferromagnetic stability [53].

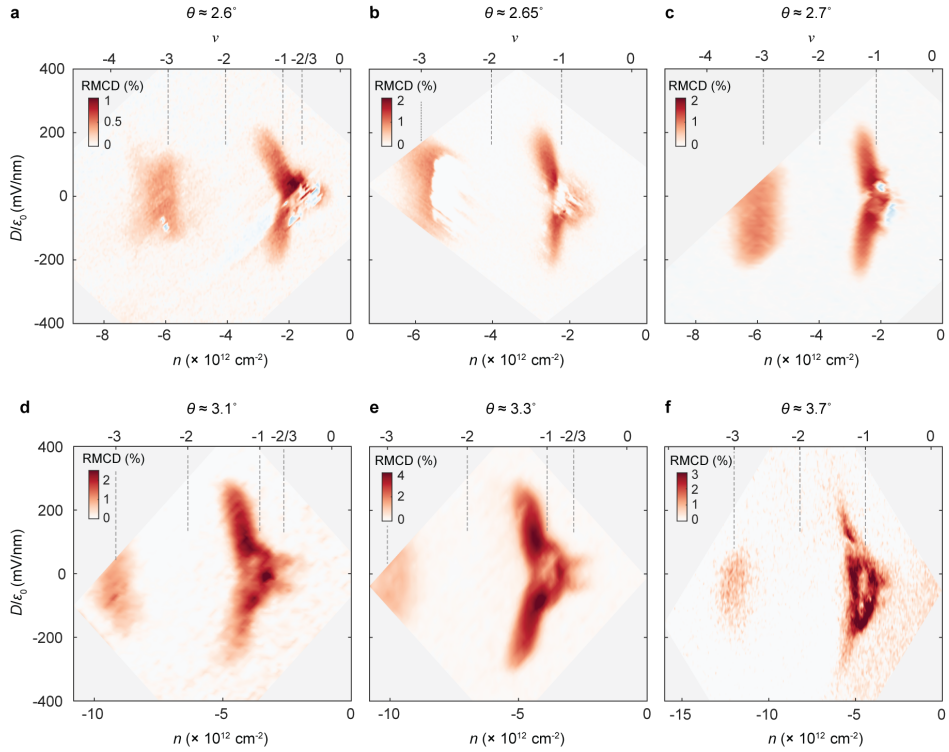

Figure 5.5: **a–f,** RMCD measurements vs. ν and D/ε_0, for devices with different twist angles. All data were taken at 1.6 K and zero magnetic field.

To assess the angular dependence of this magnetic state, we performed RMCD measurements

on devices spanning a twist angle range from 2.6° to 3.8°. Fig. 5.5 reveals that the RMCD signal near $\nu = -3$ persists throughout this range, demonstrating that the ferromagnetism is universal across these twist angles.

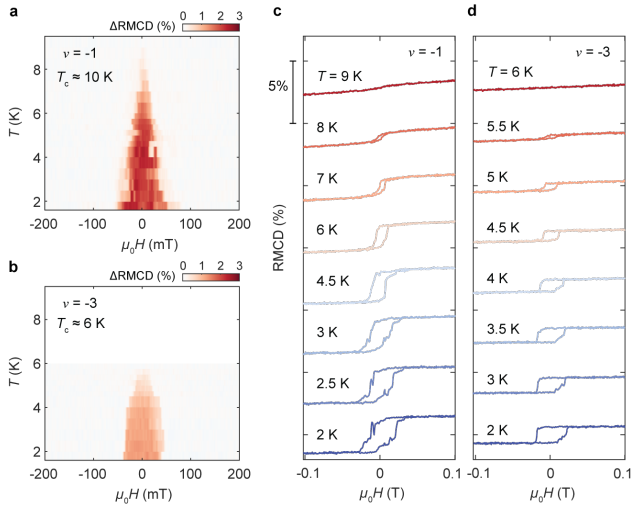

Figure 5.6: Temperature-dependent ferromagnetism at $\nu = -1$ and -3. **a,b,** Hysteresis amplitude (ΔRMCD) versus $\mu_0 H$ and T for $\nu = -1$ and -3, showing Curie temperatures $T_c \approx 10$ K and 6 K, respectively. **c,d,** RMCD field sweeps at $D/\varepsilon_0 = 0$ across temperatures from 2–9 K (**j**) and 2–6 K (**k**), confirming thermal suppression of magnetism.

To quantify the strength and stability of the magnetic states, we examine the coercivity by plotting the hysteresis amplitude, ΔRMCD (defined as the difference in RMCD between increasing and decreasing field sweeps), as a function of filling ν (Fig. 5.3b). Peaks in ΔRMCD are found at $\nu = -1$ and $\nu = -2/3$, which correspond to integer and fractional Chern insulating states, respectively. By contrast, the coercive field near $\nu = -3$ is relatively constant, approximately 25 mT, and does not show significant dependence on filling. This suggests that the magnetic phase at $\nu = -3$ is comparatively less rigid and may be more susceptible to thermal or quantum fluctuations.

Further insight comes from temperature-dependent RMCD measurements. Figures 5.6 and 5.7 show the evolution of the ferromagnetism at $\nu = -1$ and -3, respectively, as temperature is varied. The extracted Curie temperatures T_c are approximately 10 K for $\nu = -1$ and 6 K for $\nu = -3$. The reduced T_c at $\nu = -3$ reinforces the conclusion of weaker exchange interactions, potentially due to increased dielectric screening at higher carrier densities, larger band dispersion, or stronger hybridization with nearby energy bands.

It is also worth noting that the measured T_c at $\nu = -1$ in the 2.6° device is lower than the previously reported value of ∼14 K in devices with larger twist angles (e.g., $\theta \approx 3.6°$) [53]. This trend is consistent with expectations: as the moiré wavelength increases with decreasing twist angle, the real-space extent of the Wannier orbitals increases, thereby weakening exchange interactions and reducing the overall magnetic transition temperature.

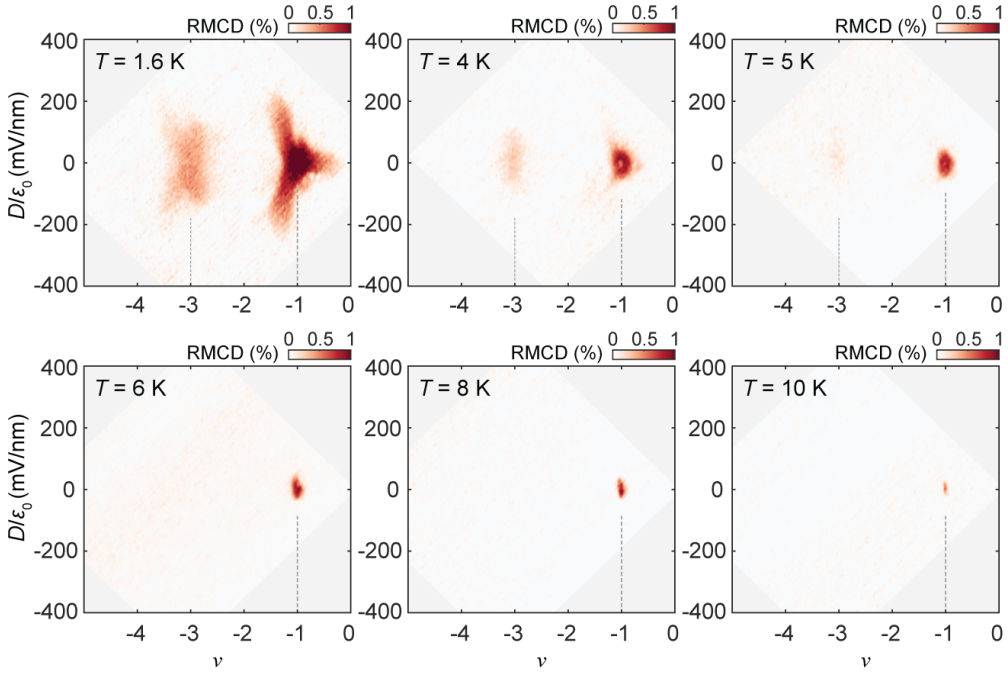

Figure 5.7: RMCD maps versus ν and D/ε_0 at various temperatures under $\mu_0 H = 50$ mT. Magnetic order near $\nu = -3$ vanishes around 6 K, while the $\nu = -1$ signal persists up to ∼9–10 K.

5.2 Topological Characterization and Anomalous Hall Effects

To explore the emergent topology of the second moiré miniband, we conducted four-terminal magneto-transport measurements on a twisted $MoTe_2$ device with twist angles of $\theta \approx 2.6°, 3.1°$, and 3.8°. Figures 5.8 display the longitudinal resistance R_{xx} and Hall resistance R_{xy}, respectively, measured as functions of the filling factor ν and vertical displacement field D/ε_0 at a base temperature of 15 mK. The temperature-dependent traces at fixed $D/\varepsilon_0 = 0$ for the 2.6° device are shown in Fig. 5.9. To correct for slight mixing between longitudinal and transverse signals, and to mitigate effects from low-field magnetic fluctuations, the data in panels a–b were symmetrized and antisymmetrized using measurements at $\mu_0 H = \pm 0.5$ T.

Near $\nu = -1$, we observe nearly vanishing R_{xx} accompanied by a quantized Hall plateau at $R_{xy} \approx -h/e^2$ (see Fig. 5.9), consistent with the formation of a robust integer quantum anomalous Hall (QAH) state. At $\nu = -2/3$, a clear dip in R_{xx} coincides with $R_{xy} \approx -3h/2e^2$, indicating the emergence of a fractional Chern insulator (FCI) phase. While this signal is somewhat degraded

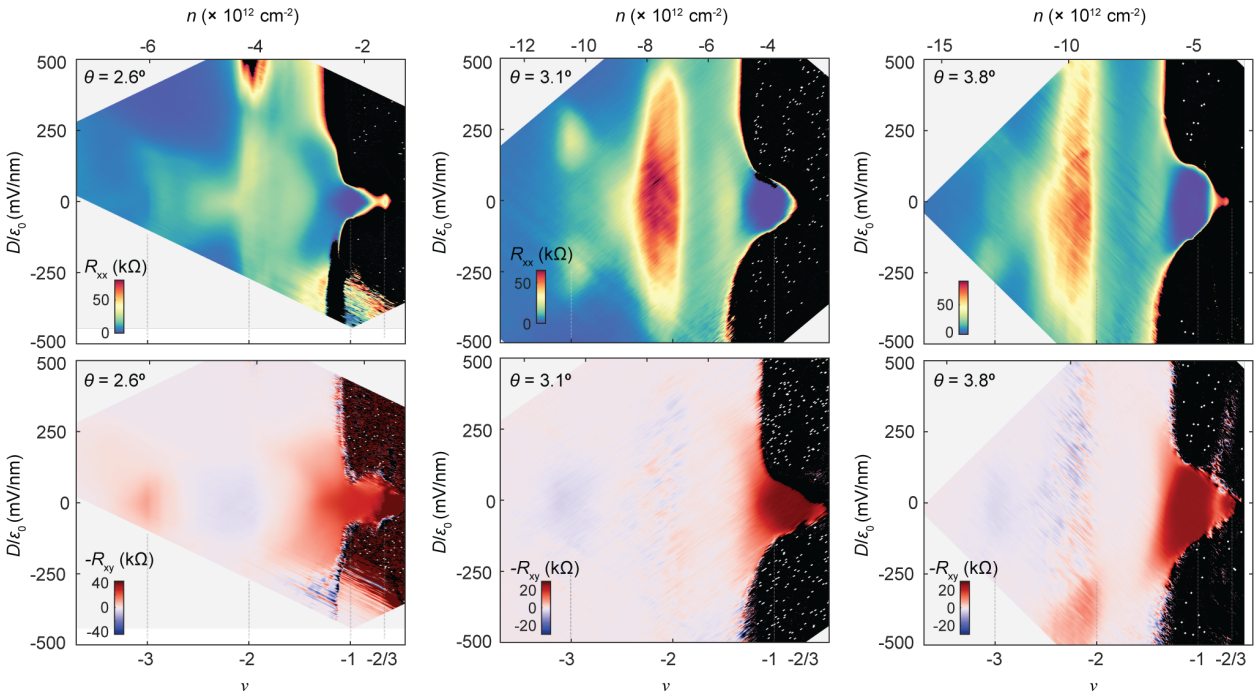

Figure 5.8: Transport phase diagram for different twist angles. Longitudinal resistance R_{xx} (top row) and Hall resistance $-R_{xy}$ (bottom row) versus filling factor ν and displacement field D/ε_0 at 15 mK, symmetrized and antisymmetrized at $|\mu_0 H| = 100$ mT.

due to increased contact resistance at low carrier density, these signatures at both $\nu = -1$ and $-2/3$ agree with earlier experimental observations [13, 14] and establish the presence of correlated topological states in the system.

Additionally, we identify a distinct anomalous Hall response near $\nu = -3$, where R_{xx} exhibits a shallow minimum around $\sim$7 kΩ and R_{xy} reaches a peak value of approximately -12 kΩ. Though R_{xy} is sizable, it is not quantized, and R_{xx} remains finite, suggesting an incipient Chern insulating state where the topological gap is not fully opened. As the temperature increases from 50 mK to 6 K, R_{xx} at $\nu = -3$ initially increases while R_{xy} decreases but remains non-zero. Upon crossing the estimated Curie temperature $T_c \approx 6$ K, R_{xx} begins to drop again, indicating a transition out of the ferromagnetic regime.

These findings support the band structure scenario depicted in Fig. 5.1. At $\nu = -1$, strong exchange interactions between spin-valley-split bands fully lift the degeneracy, opening a clear Chern

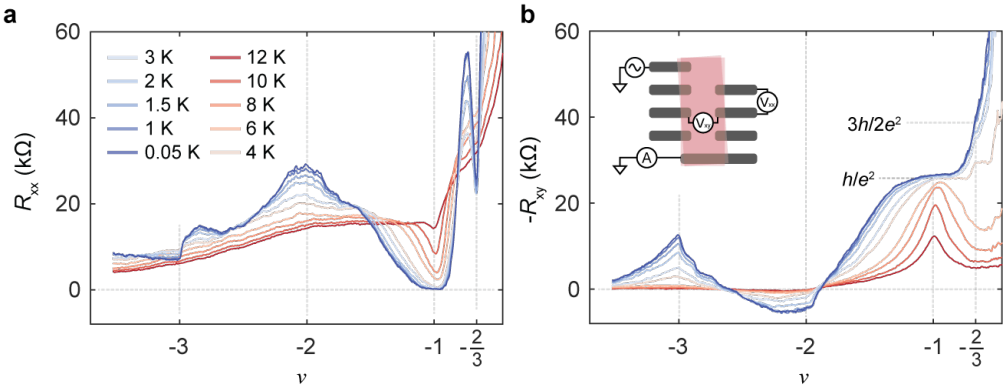

Figure 5.9: Temperature-dependent transport. **a,b,** Symmetrized R_{xx} (**a**) and antisymmetrized $-R_{xy}$ (**b**) versus ν at fixed $|\mu_0 H| = 500$ mT across temperatures. R_{xx} minima and quantized R_{xy} plateaus mark Chern insulator ($\nu = -1$) and FCI ($\nu = -2/3$) states. At $\nu = -3$, a dip in R_{xx} and non-quantized R_{xy} suggest an incipient Chern phase. Inset: measurement configuration.

gap and enabling the QAH phase. However, at $\nu = -3$, the second moiré miniband exhibits a broader bandwidth, leading to overlap between Chern bands as the Fermi level crosses across both $\pm K$ bands. This interpretation is corroborated by Hartree-Fock band calculations, which suggest that band overlap and reduced density of states play critical roles in suppressing full quantization. Additionally, at $\nu = -2$, the Hall response vanishes at zero field, consistent with balanced occupation of $+K$ and $-K$ valleys. However, with increasing magnetic field, R_{xy} rapidly rises and saturates around 7–8 kΩ, hinting at field-driven valley polarization. The precise nature of this intermediate state remains to be fully understood and warrants further investigation.

To investigate the twist-angle dependence of the anomalous Hall response, we compare magnetotransport data from two devices with twist angles $\theta = 2.6°$ and $3.8°$. As shown in Fig. 5.10, R_{xy} exhibits clear hysteresis as a function of out-of-plane magnetic field at both $\nu = -1$ and $\nu = -3$. While the $\nu = -1$ state in both devices displays a negative Hall resistance approaching the quantized value $-h/e^2$ after positive field initialization—consistent with spontaneous valley polarization in the first Chern band—the behavior at $\nu = -3$ is markedly different between the two samples.

In the $3.8°$ device, the Hall signal at $\nu = -3$ reverses sign relative to that at $\nu = -1$, yielding a positive R_{xy} of approximately $+7$ kΩ following the same magnetization protocol. This sign reversal is also apparent in the corresponding dual gate maps shown in Fig. 5.8, highlighting a change in

the topological character of the second Chern band. By contrast, in the 2.6° device, the $\nu = -3$ state exhibits a negative Hall response of roughly -12 kΩ, aligning in sign with the $\nu = -1$ state and suggesting identical Chern indices for both bands. Taken together, these observations suggest a twist-angle-driven inversion of the second Chern band's topology near $\theta_c \approx 3°$.

5.3 Magnetic Field-Induced Topological Phase Transition

An effective approach to experimentally probe the topological character of Chern bands is to study their evolution under applied magnetic fields. In particular, the Chern number of gapped states can be extracted from the slope of their carrier density trajectories in a magnetic field using the Středa formula [11, 170, 108, 109]. To this end, we carried out magneto-transport measurements on twisted $MoTe_2$ devices with twist angles of 3.8° and 2.6°, tracking the longitudinal (R_{xx}) and transverse (R_{xy}) resistances as a function of perpendicular magnetic field $\mu_0 H$ and filling factor ν.

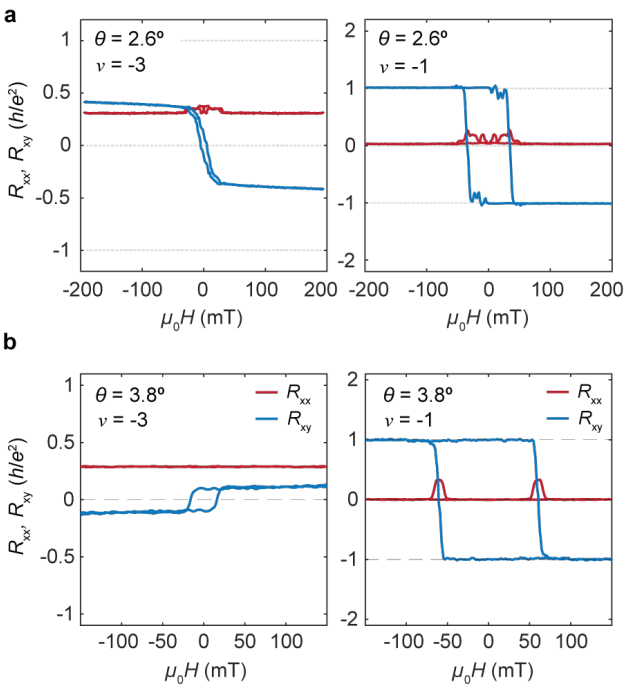

Figure 5.10: Anomalous Hall effect at $\nu = -1$ and -3. **a**, R_{xx} (red) and $-R_{xy}$ (blue) vs. magnetic field for $\nu = -1$ and -3 in the 2.6° device at 15 mK. **b**, Same for the 3.8° device. The sign reversal of the $\nu = -3$ Hall signal implies an opposite Chern number relative to the 2.6° device.

Figures 5.11a,b and 5.11e,f present the resulting fan diagrams for the 3.8° and 2.6° samples, respectively. These measurements were performed at base temperatures below 30 mK and zero displacement field ($D/\varepsilon_0 = 0$). In each panel, R_{xx} and R_{xy} have been symmetrized and antisymmetrized, respectively, to eliminate spurious mixing.

The resulting fan diagrams reveal a rich hierarchy of magnetic-field-induced states, which are summarized in the Wannier plots of Figs. 5.11c and 5.11g. Annotated labels in the form of (C, ν) denote the Chern number C and the associated filling factor ν extracted via Středa analysis. Con-

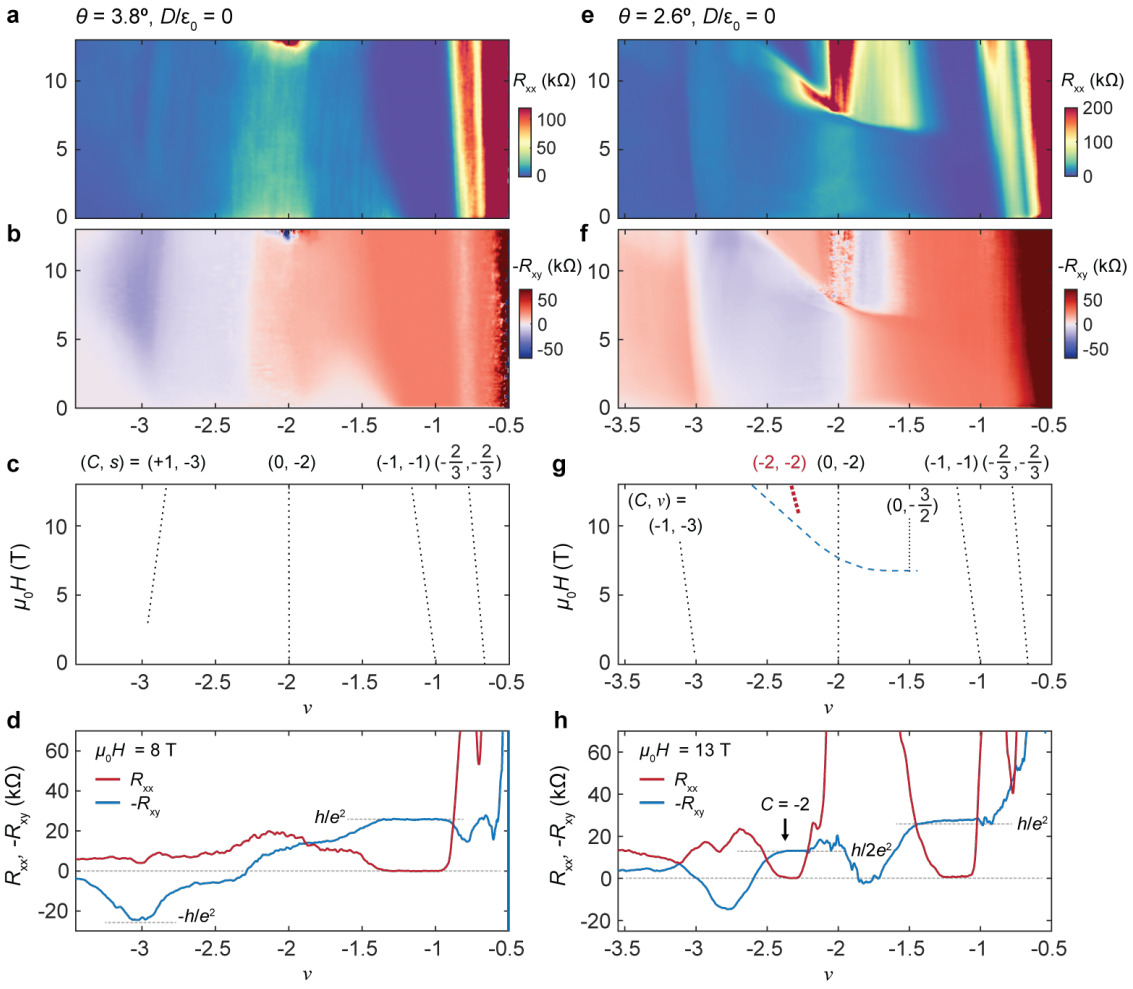

Figure 5.11: Topological band inversion and Chern transitions at $\nu = -2$. **a,b,** Landau fan diagrams of symmetrized R_{xx} (**a**) and antisymmetrized $-R_{xy}$ (**b**) at $T < 30$ mK for a 3.8° $tMoTe_2$ device at $D/\varepsilon_0 = 0$. **c,** Corresponding Wannier diagram showing extracted Chern numbers C and intercepts ν. **d,** Line cuts of R_{xx} and $-R_{xy}$ versus ν at $\mu_0 H = 8$ T; a nearly quantized $-R_{xy} \approx -h/e^2$ is seen at $\nu = -3$ with a sign opposite to the $\nu = -1$ QAH state. **e–g,** Same as **a–c**, but for the 2.6° device. The dashed blue line marks a high-field topological transition; the dotted red line traces a $C = -2$ state. **h,** R_{xx} and $-R_{xy}$ at 13 T showing a $C = -2$ Chern insulator near $\nu = -2$, with vanishing R_{xx} and quantized $-R_{xy} \approx h/2e^2$.

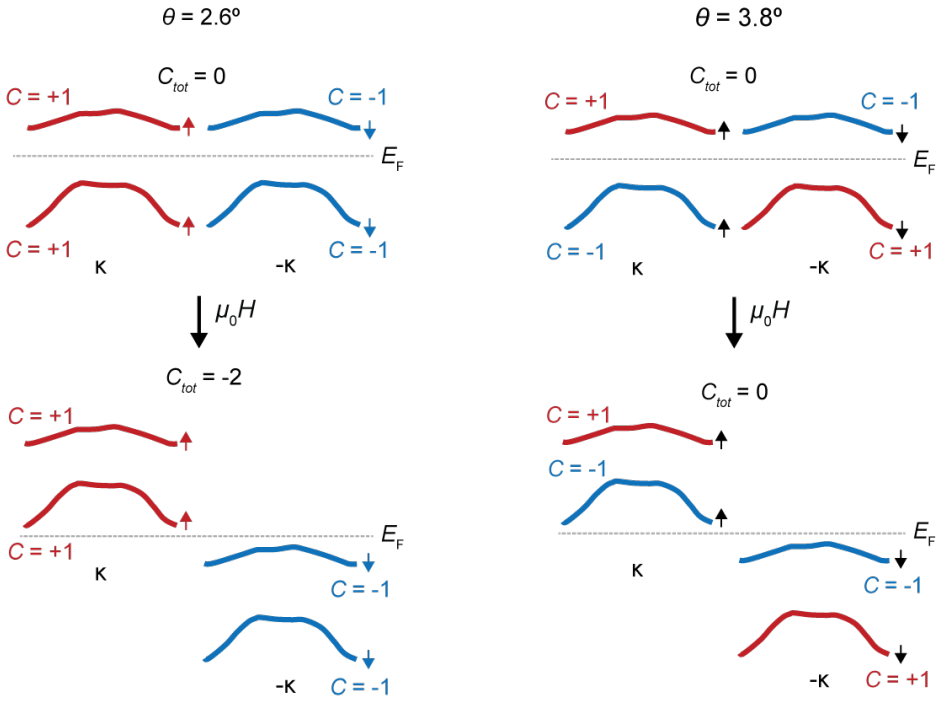

Figure 5.12: Zeeman-induced band inversion at $\nu = -2$. Spin- and valley-resolved band structure for the 2.6° device, with Fermi level E_F indicated. At zero magnetic field, both valleys are equally filled, yielding a net Chern number $C_{\text{tot}} = 0$. At high field, Zeeman coupling drives a band inversion between the first $-K$ and second $+K$ bands, resulting in $C_{\text{tot}} = -2$ at $\nu = -2$. For the 3.8° device, a similar inversion is expected, but the net Chern number remains zero.

sistent with previous studies [11, 13, 14], we observe dispersing signatures of the integer QAH state at $(C, \nu) = (-1, -1)$ and a fractional Chern insulator at $(-2/3, -2/3)$. In the 3.8° device, the $\nu = -3$ state is characterized by a Středa slope $C = +1$, with $R_{xy} \approx h/e^2$ and R_{xx} strongly suppressed at high fields (Fig. 5.11 d). In contrast, the same $\nu = -3$ state in the 2.6° device exhibits a negative slope $C = -1$, aligning with the topological reversal in the second Chern band discussed earlier. This confirms that the Středa slope reflects the cumulative Chern number up to the Fermi level, and its sign is sensitive to twist angle.

For the 2.6° device, additional topological states appear at magnetic fields above ∼7 T in the vicinity of $\nu = -2$ (Figs. 5.11e–g). At lower fields, R_{xx} remains finite (∼28 kΩ) and shows little field dependence, while R_{xy} saturates near 7–8 kΩ. However, above $\mu_0 H = 7$ T, a new gapped phase emerges just above $\nu = -2$, where R_{xx} drops to near-zero and R_{xy} stabilizes at $-h/2e^2$. This

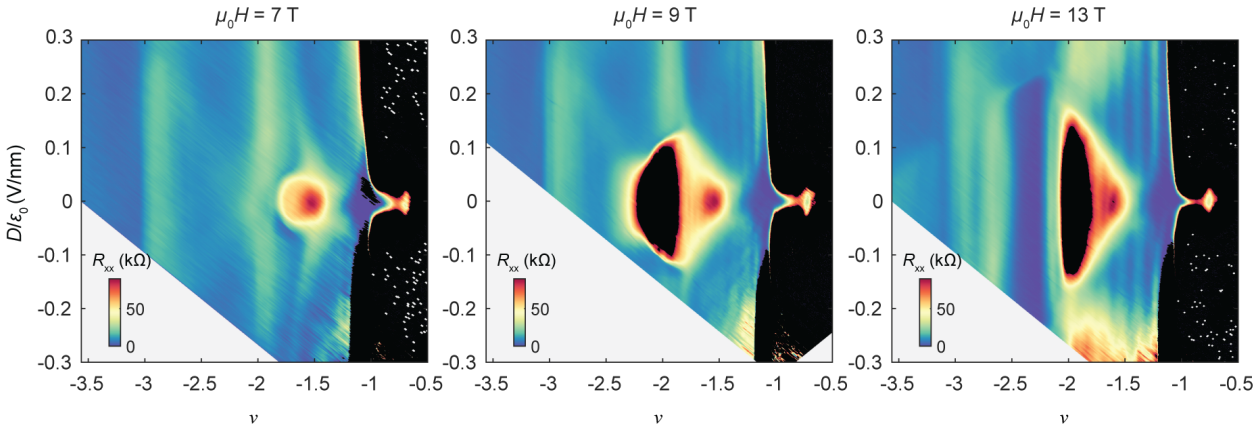

Figure 5.13: High-field dual-gate maps. Longitudinal resistance R_{xx} versus filling factor ν and displacement field D/ε_0 at $\mu_0 H = 7$ T (**a**), 9 T (**b**), and 13 T (**c**). A distinct insulating feature appears near $\nu = -3/2$ and $D/\varepsilon_0 = 0$.

state is clearly resolved in Fig. 5.11h, which shows line cuts of R_{xx} and R_{xy} versus ν at $\mu_0 H = 13$ T. The corresponding Středa slope indicates a Chern number $C = -2$ with an intercept at $\nu = -2$, confirming the emergence of a magnetic-field-induced $C = -2$ Chern insulator.

The microscopic origin of this phase can be understood as a Zeeman-driven crossing between flat bands from opposite valleys. As depicted schematically in Fig. 5.12, at $\nu = -2$ and low field, both $+K$ and $-K$ valleys are equally populated, each contributing opposite Chern numbers and resulting in a net topological index of $C = 0$. Upon increasing $\mu_0 H$, the upper flat band in the $-K$ valley shifts upward while the lower flat band in the $+K$ valley moves downward. Once the two bands cross, both filled bands originate from the same valley, each carrying a Chern number $C = +1$. This reconfiguration leads to a net $C = -2$ insulating state, as observed experimentally. In contrast, the 3.8° device exhibits a similar incompressible feature at $\nu = -2$ but remains topologically trivial even after band crossing, as can be seen in Fig. 5.12.

Additional temperature-dependent transport measurements indicate that this field-induced phase has an activation gap of approximately 13 K at 13 T. Moreover, abrupt changes in transport suggest that the topological phase transition at the band crossing point is first-order in nature.

Beyond the Chern insulator states, the fan diagram also reveals a distinct insulating phase near $\nu = -3/2$ above $\mu_0 H = 7$ T (Fig. 5.11g). This state is prominent in Fig. 5.13, where

R_{xx} is mapped as a function of ν and D/ε_0 at various fixed fields. The insulating feature is non-dispersive with magnetic field, implying that it is topologically trivial and originates from electronic correlations. We interpret this state as a charge-ordered insulator stabilized at half-filling of a valley-polarized Chern band, following the Zeeman-induced band crossing. While theoretical proposals have predicted non-Abelian FCI phases at comparable fillings [160, 171, 169, 172, 173, 174, 175], our observations suggest that, under the current conditions in 2.6° $tMoTe_2$, a charge-ordered state is energetically favored over topological liquid phases at $\nu = -3/2$.

5.4 Conclusion and Outlook

In summary, our experimental characterization of the second moiré flat band in $tMoTe_2$ highlights significant phenomena such as spontaneous ferromagnetism, angle-dependent topological transitions, and magnetic field-induced topological phase transitions. These insights form a foundation for future theoretical and experimental efforts directed towards realizing and manipulating higher-order fractional Chern insulating states and exploring their potential non-Abelian anyonic excitations. Our findings particularly underline the subtle interplay between topological band structures and strong electron-electron interactions in moiré systems.

The emergence of spontaneous ferromagnetism and signatures of a developing Chern insulating state at $\nu = -3$, together with the clear identification of a Zeeman-driven topological phase transition, establish a promising platform for realizing even-denominator fractional Chern insulator (FCI) phases in higher Chern number bands. Recent theoretical and experimental studies have suggested the possibility of a time-reversal-invariant fractional quantum spin Hall state at the same filling in 2.1° twisted $MoTe_2$ [176].

Our findings offer important empirical constraints for these proposals, and provide a detailed phase landscape for future efforts aimed at understanding correlated topological phases in this setting. The coexistence and interplay of interaction-driven magnetism, tunable band topology, and high-field Chern insulating states position twisted $MoTe_2$ as a rich and versatile platform for engineering novel many-body quantum states.

Chapter 6

DISSIPATIONLESS FRACTIONAL CHERN INSULATORS

Fractional Chern insulators (FCIs) exhibit a fractionally quantized Hall conductance, even in the absence of an external magnetic field. These phases represent lattice counterparts of the fractional quantum Hall (FQH) states [21, 6], which traditionally emerge in two-dimensional electron gases subjected to strong magnetic fields. In both platforms, the emergence of fractional quasiparticles is rooted in strong Coulomb interactions, but they exhibit key differences.

In conventional FQH systems, this length scale is set by the magnetic length $l_B \approx 26\,\mathrm{nm}/\sqrt{B[\mathrm{T}]}$, where B denotes the applied magnetic field in teslas. By contrast, in FCIs realized on a crystalline lattice, the relevant length scale is the moiré or lattice constant λ, which is independent of external fields. In moiré superlattices such as twisted bilayer transition metal dichalcogenides (TMDs), λ typically falls near 5 nm—substantially smaller than magnetic lengths attainable under common experimental conditions. Combined with the intrinsically reduced dielectric screening in atomically thin layers [177], this suggests that FCI platforms could, in principle, support larger many-body energy gaps than their FQH counterparts.

In twisted bilayers of $MoTe_2$ ($tMoTe_2$), robust fractional states such as the $\nu = -2/3$ phase have been observed to persist at elevated temperatures up to 1.5 K—nearly 40% of the material's ferromagnetic transition temperature [13]. Thermodynamic magnetometry measurements [154] estimate an activation gap of approximately 2.3 meV ($\sim$27 K) for this state, implying substantial room for further enhancement via improved material synthesis and device engineering.

A defining experimental signature of quantum Hall states is the coexistence of quantized Hall resistance (R_{xy}) and vanishing longitudinal resistance (R_{xx}), indicating edge-dominated, dissipationless transport. While R_{xy} quantization has been reported in both $tMoTe_2$ and rhombohedral graphene FCIs, the persistence of finite R_{xx} suggests residual dissipative channels, likely stemming from disorder or imperfect contact engineering.

This situation echoes early observations in the FQH regime. For instance, in the initial discovery

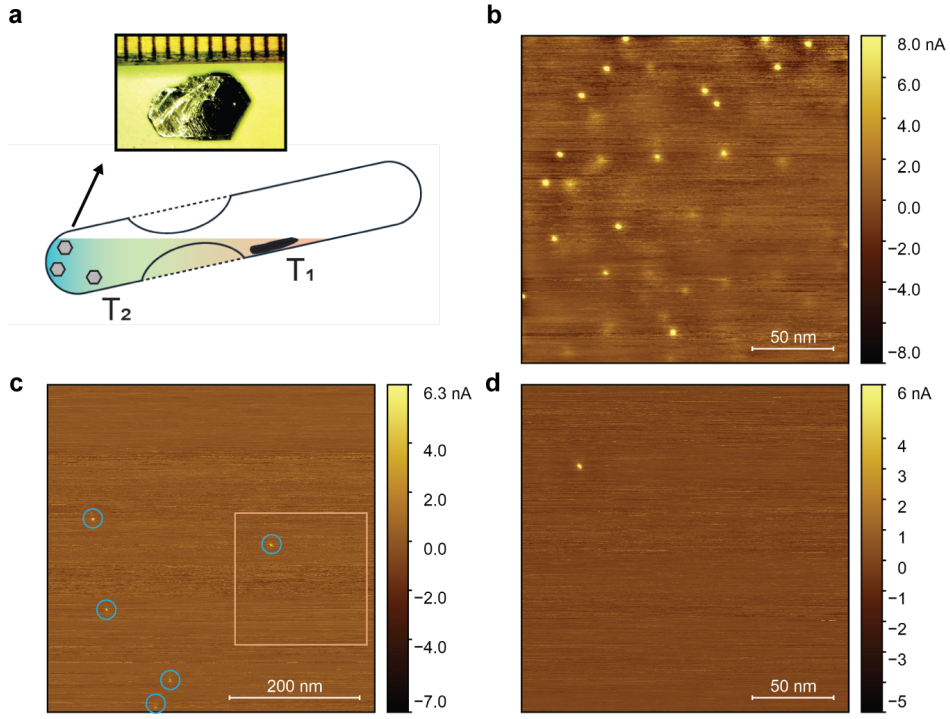

Figure 6.1: Horizontal flux growth and defect characterization. **a**, Schematic of horizontal flux transport growth in Te flux. **b**, Conductive AFM (c-AFM) image of commercial $MoTe_2$ showing various unidentified defects with density $\sim 10^{11}$ cm^{-2}. **c**, c-AFM image of flux-grown $MoTe_2$ with a dominant defect type (blue circles), density $\sim 2 \times 10^9$ cm^{-2}. **d**, Zoom-in image of the orange box in **c**.

of the $\nu = 1/3$ state in GaAs quantum wells [21], quantization of R_{xy} was accompanied by a non-zero R_{xx} on the order of several kΩ, in samples with electron mobilities around $10^5\,\mathrm{cm}^2/\mathrm{Vs}$. It was only with subsequent improvements—pushing mobilities above $5 \times 10^7\,\mathrm{cm}^2/\mathrm{Vs}$—that R_{xx} was effectively quenched and a zoo of additional fractional states emerged [178, 179, 180]. This historical precedent suggests that the development of FCIs is likely to follow a similar trajectory, where ongoing refinement in materials and device interfaces will be key to achieving fully dissipationless transport.

In this chapter, we present transport measurements on an optimized t$MoTe_2$ device that reveals several new features of the FCI regime, including fractional quantization with negligible R_{xx} at elevated temperatures. To realize such high-quality performance, we sourced bulk $MoTe_2$ crystals grown via a horizontal flux technique, which significantly reduces structural disorder. Conductive

atomic force microscopy performed on these as-grown crystals indicates a two-order-of-magnitude reduction in defect density compared to commercially available $MoTe_2$ used in earlier studies [13] (Fig. 6.1).

Device fabrication was further refined through advanced atomic force microscopy (AFM) cleaning procedures, designed to expel buried hydrocarbon residues beyond the active Hall bar region (Fig. 6.2). The resulting van der Waals heterostructure features a dual-gated architecture with patterned local gates [13] to simultaneously reduce contact resistance and electrostatically define sharp sample edges (Fig. 6.3). The $MoTe_2$ homobilayer is configured in an AA-stacked geometry with a twist angle of approximately 3.7° (Fig. 6.3), yielding a moiré periodicity conducive to strong electronic correlations.

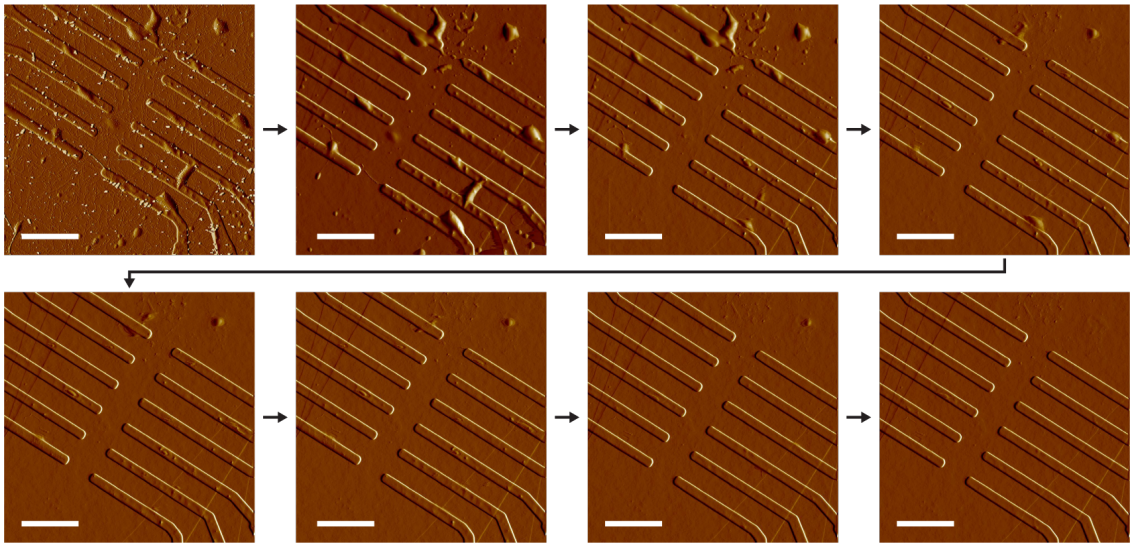

Figure 6.2: Contact-mode AFM images after hBN/t$MoTe_2$ transfer. Progressive removal of bubbles outside the Hall bar region is shown. Scale bars: 2 μm.

6.1 FQAH Phase Diagram

We explore the fractional quantum anomalous Hall (FQAH) regime through low-temperature transport measurements performed at a base temperature of 10 mK. A schematic of the measurement setup is presented in Fig. 6.3b.

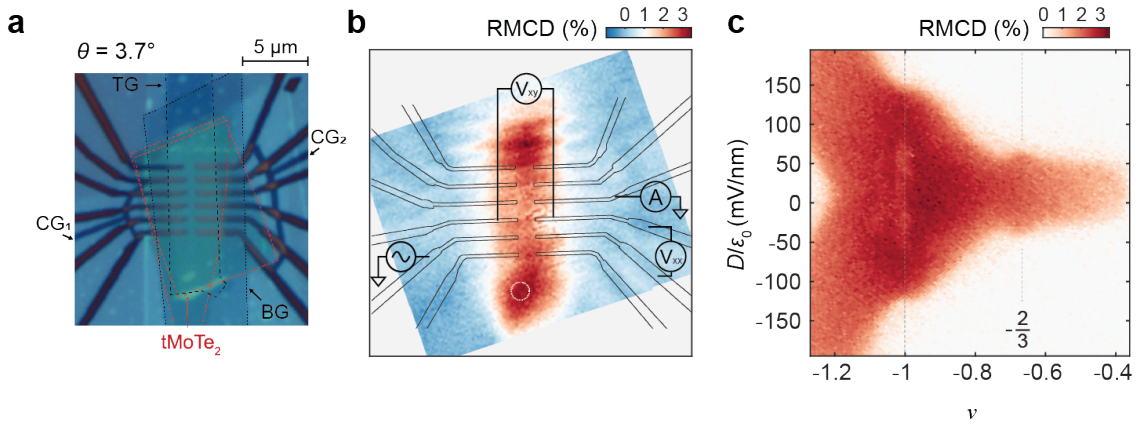

Figure 6.3: Device geometry and RMCD measurements. **a,** Optical image of the device with $MoTe_2$ flake outlines marked in red; the top gate (TG) defines the active region. **b,** RMCD spatial map at $\nu = -1$ and $D/\varepsilon_0 = 0$ shows localized magnetic response within the top-gated region. **c,** RMCD intensity as a function of ν and D/ε_0, taken at $T = 1.6$ K and $\mu_0 H = 5$ mT at the position indicated by the white circle in **b**.

Figure 6.3c shows the reflective magnetic circular dichroism (RMCD) response plotted against the moiré filling factor v and the electric field D/ε_0. The magnetic phase boundaries extracted from RMCD are consistent with prior studies [11, 53] and delineate a ferromagnetic regime spanning several fractional fillings.

The corresponding longitudinal and transverse resistances, R_{xx} and R_{xy}, are shown in Figs. 6.4a and b, respectively, as functions of v and D/ε_0. To minimize the influence of magnetic domain fluctuations, all transport data were acquired under a weak perpendicular field of $\mu_0 H = \pm 200\,\mathrm{mT}$ and symmetrized/antisymmetrized, respectively.

Near-zero electric fields reveal distinct resistance signatures associated with both integer and fractional Chern insulating states. Specifically, we observe suppressed or vanishing R_{xx} in conjunction with elevated values of $|R_{xy}|$ at fillings $v = -1$, $-2/3$, $-3/5$, and $-4/7$, corresponding to topological states with quantized Hall conductance.

To validate the Chern nature of these phases, we analyze the field-dependent evolution of R_{xx} in Fig. 6.5, where the resistance minima are plotted versus magnetic field $\mu_0 H$ and carrier density n. The trajectory of these minima exhibits linear dependence, characteristic of quantized Chern bands. Overlaid dashed lines represent expected trajectories based on the Středa relation, $C = \phi_0\, \partial n/\partial B$,

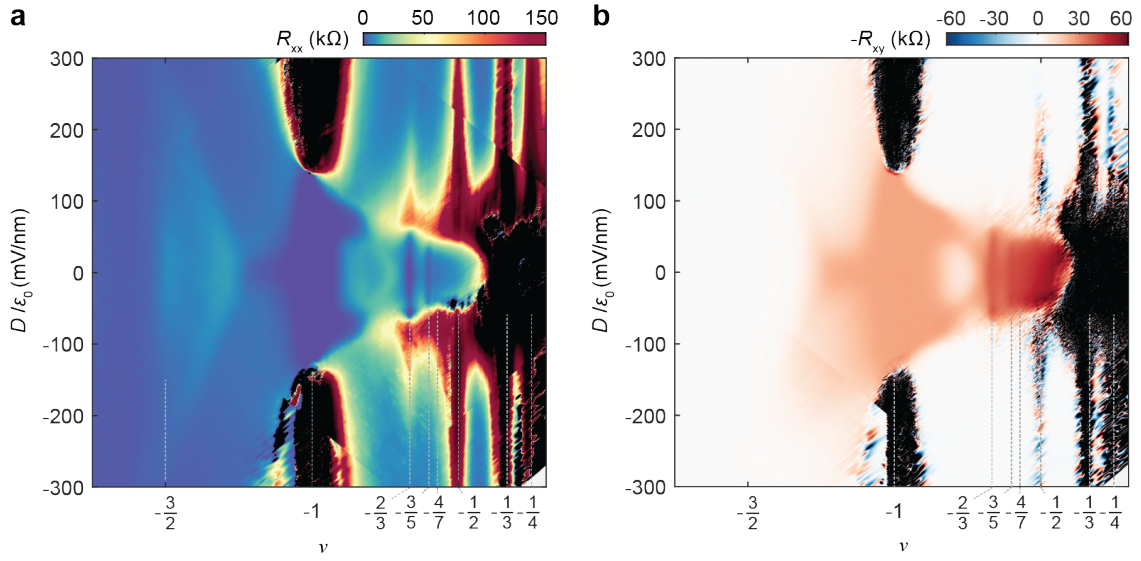

Figure 6.4: Transport phase diagram of improved device. **a,** Longitudinal resistance R_{xx} and **b,** transverse resistance $-R_{xy}$ plotted versus filling factor ν and displacement field D/ε_0, measured at 10 mK. Data are symmetrized and antisymmetrized at $\mu_0 H = \pm 0.2$ T.

where ϕ_0 is the magnetic flux quantum. The agreement between experiment and theory provides strong evidence that these states carry Chern numbers $C = -1$, $-2/3$, $-3/5$, and $-4/7$.

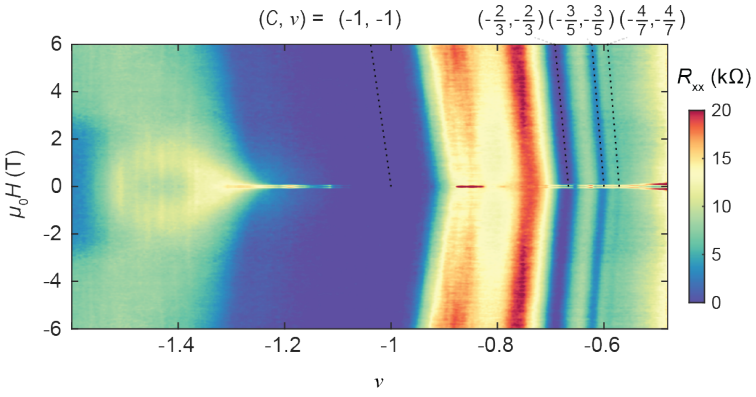

Figure 6.5: Landau fan of longitudinal resistance. R_{xx} plotted versus magnetic field $\mu_0 H$ and filling factor ν reveals integer ($C = -1$) and fractional ($C = -2/3$, $-3/5$, $-4/7$) Chern insulators.

Although the overall structure resembles earlier results [13], the present measurements exhibit marked improvements attributed to superior sample quality. In the earlier study [13], only the $-2/3$ FCI phase was distinctly resolved, and its corresponding density plateau extended over $\sim 2.5 \times 10^{11}\,\mathrm{cm}^{-2}$. In contrast, our optimized device reveals additional fractional states at $\nu = -3/5$ and $-4/7$, while the $-2/3$ state exhibits a much narrower plateau

width—only $\sim 1.25 \times 10^{11}\,\mathrm{cm}^{-2}$—indicating reduced disorder.

Moreover, enhanced device cleanliness and electrostatic control allow access to previously uncharted low-filling regimes. At high displacement fields ($D/\varepsilon_0 > 100\,\mathrm{mV/nm}$), we uncover a series of incompressible, insulating states at commensurate fillings $\nu = -2/3$, $-1/2$, $-1/3$, and $-1/4$. These phases likely arise from interaction-driven charge ordering on the triangular moiré lattice, particularly in the layer-polarized regime [181, 182].

6.2 Realization of Dissipationless Fractional States

A key observation here is the suppression—and in some cases, complete vanishing—of the longitudinal resistance R_{xx} across fractional Chern insulating phases. Figure 6.6a displays line traces of R_{xx} (red) and $-R_{xy}$ (blue) as functions of filling factor ν at fixed electric field $D/\varepsilon_0 = 0$. The data have been symmetrized and antisymmetrized at $\mu_0 H = \pm 100\,\mathrm{mT}$.

Within the filling range $\nu \in [-1.2, -0.9]$, the longitudinal resistance R_{xx} falls to zero, while the Hall resistance $|R_{xy}|$ remains quantized at h/e^2, confirming a robust quantum anomalous Hall (QAH) phase. At fractional filling $\nu = -2/3$, R_{xx} again completely vanishes, and the Hall resistance approaches $3h/2e^2$ within 0.3%, signaling a nearly ideal, dissipationless fractional Chern insulator state.

To take a closer look at these fractional phases, Fig. 6.6b presents a high-resolution sweep of R_{xx} across fractional fillings. Slight deviations from the commensurate value $\nu = -2/3$ induce a sharp increase in R_{xx}, reaching 10–20 kΩ, accompanied by a reduction in $|R_{xy}|$ (inset, Fig. 6.6a). This behavior—where R_{xy} decreases rather than increases upon detuning—differs from what is typically observed in FQH systems and has been consistently noted not only in $tMoTe_2$ [13], but also in rhombohedral graphene [143, 183]. Its microscopic origin remains an open theoretical question.

At $\nu = -3/5$, R_{xx} displays a pronounced dip to $\sim 3\,\mathrm{k\Omega}$, while $|R_{xy}|$ reaches approximately 97% of $5h/3e^2$, providing further evidence of a fractional Chern insulating state at this filling. Additional local minima in R_{xx} are also observed at $\nu = -4/7$ and $-5/9$, though these are weaker; their thermal activation behavior will be discussed in a later section.

As the system approaches $\nu = -1/2$, R_{xx} rises to $\sim 10\,\mathrm{k\Omega}$, and the Hall resistance transitions smoothly with doping, trending toward $2h/e^2$—the expected value for half-filling of a topologically nontrivial flat band. This linear ν-dependence of R_{xy} near half-filling mirrors observations in earlier

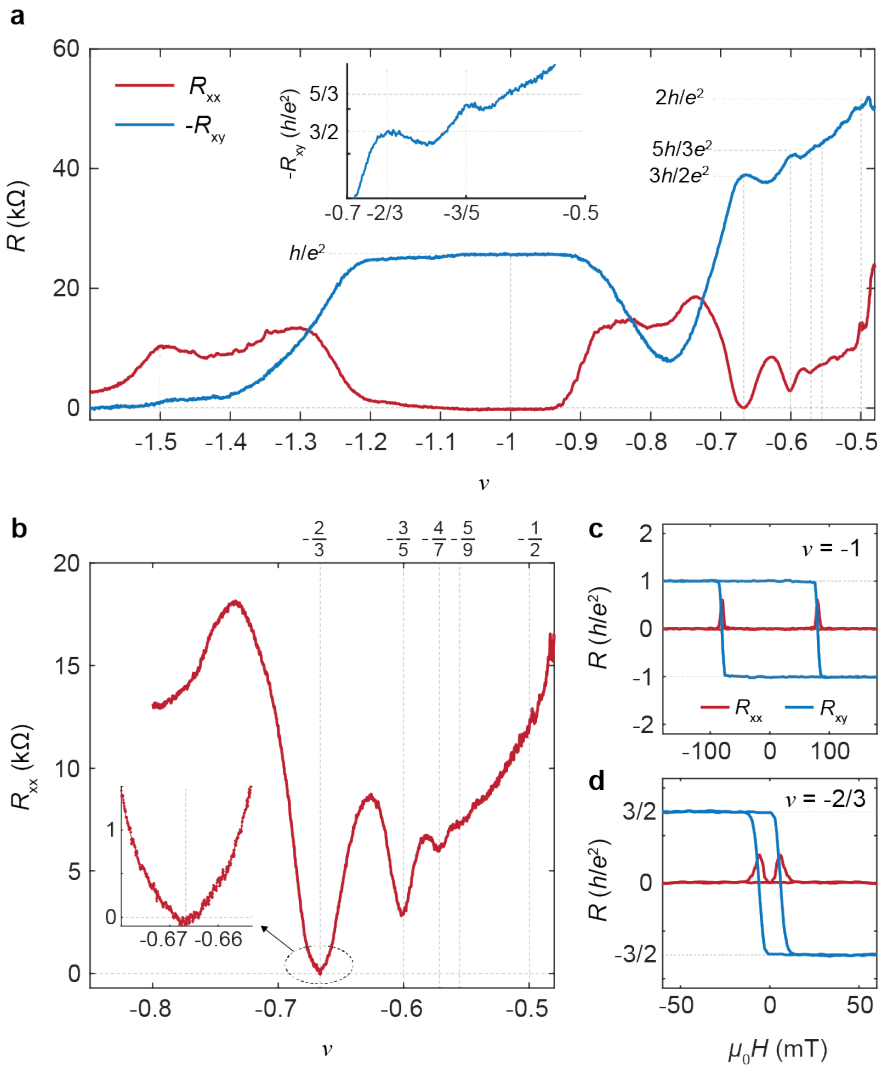

Figure 6.6: Dissipationless transport in fractional Chern insulator states. **a,** Symmetrized R_{xx} (red) and antisymmetrized $-R_{xy}$ (blue) measured at $\mu_0 H = \pm 100$ mT and $T = 10$ mK as a function of filling factor ν. Clear signatures of the QAH state at $\nu = -1$ and a sequence of FCIs at $\nu = -p/(2p-1)$ ($p = 2$–5) are identified by quantized R_{xy} (inset) and suppressed R_{xx}. **b,** Doping dependence of R_{xx} across fractional fillings, with pronounced minima at the FCI states. (Inset) Magnified view near $\nu = -2/3$ shows vanishing R_{xx}. **c, d,** Magnetic hysteresis of R_{xx} (red) and R_{xy} (blue) at $\nu = -1$ (c) and $\nu = -2/3$ (d)

studies [13], and is consistent with theoretical expectations for an anomalous composite Fermi liquid state [54, 55].

To further validate the quantized anomalous Hall character of these states, we performed magnetic hysteresis measurements by sweeping the magnetic field at fixed filling. Figures 6.6c and d show representative results for $v = -1$ and $-2/3$, respectively. In both cases, clear hysteresis loops are observed in R_{xy}, along with quantized plateaus at $|R_{xy}| = h/|C|e^2$, consistent with Chern numbers $C = -1$ and $C = -2/3$.

The coercive field, which characterizes the width of the hysteresis loop, exhibits a strong dependence on filling. At $v = -1$, the coercivity peaks near $\sim$100 mT, while it diminishes to $\sim$15 mT at $v = -2/3$. This doping-dependent evolution is in line with previous studies [13, 11, 53], and reflects the interplay between interaction strength, magnetic anisotropy, and topological band structure across the FQAH phase diagram.

6.3 Interplay Between FCI States, Metallic Phases, and Charge Order

Beyond the robust FCI and QAH plateaus, our data unveil several additional transport signatures that offer insight into competing many-body phases. Figure 6.6a reveals a distinct peak in R_{xx} at $v = -3/2$, where the longitudinal resistance rises to approximately 10 kΩ, and the Hall response R_{xy} vanishes. This peak remains prominent at low magnetic fields and shows negligible dispersion with increasing field strength. These features are consistent with a topologically trivial, pinned charge density wave (CDW) phase. At higher fields, the expanding Chern insulator regime near $v = -1$ encroaches into the $v = -3/2$ region, weakening the CDW signature.

Within the intermediate range $v \in [-0.85, -0.74]$, both R_{xx} and $|R_{xy}|$ decline, with R_{xx} exceeding $|R_{xy}|$, a hallmark of an anomalous Hall metallic phase [184]. This behavior is attributed to partial filling of a Chern band, where dissipative transport coexists with finite Hall response. While R_{xy} exhibits a dip across this filling range, RMCD measurements (Fig. 6.3c and Figs. 6.13b) reveal a smooth, monotonic reduction in magnetization. This contrast underscores the emergence of a valley-polarized, spin-polarized metallic phase, where bulk conduction dominates even as spontaneous symmetry breaking remains intact.

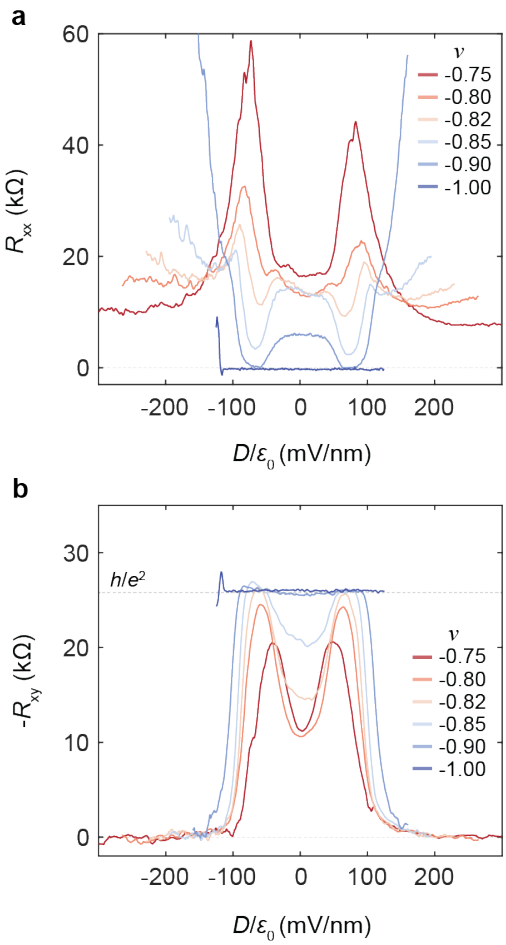

Figure 6.7: Anomalous Hall metal phase. **a-b,** Symmetrized R_{xx} (a) and antisymmetrized $-R_{xy}$ (b) versus D/ε_0 at selected ν. For ν just below -1, the system remains in a QAH state up to $D/\varepsilon_0 \approx 75$ mV/nm, but as ν increases, it transitions into a ferromagnetic metal.

The electric field dependence of different FCI states reveals further subtleties in their phase stability and associated lattice symmetry. For the $\nu = -2/3$ FCI (Fig. 6.8a), R_{xy} maintains quantization over a broad range of D/ε_0 near zero field. Upon exceeding a critical field threshold, R_{xx} increases sharply and remains elevated across a wide field window. This abrupt transition signals a crossover from a hybridized honeycomb regime—where electrons delocalize between layers—to a layer-polarized triangular moiré lattice. Continued increase in displacement field eventually suppresses the quantized Hall state, giving way to a metallic regime, likely reflecting the breakdown of charge order and delocalization of fractionalized carriers.

In contrast, the $\nu = -3/5$ FCI state (Fig. 6.8b) behaves differently under electric field tuning. Here, a broad resistance peak in R_{xx} emerges upon entering the layer-polarized regime, but unlike the $-2/3$ state, R_{xx} rapidly declines again at larger $|D/\varepsilon_0|$, transitioning into a metallic phase (see also Fig. 6.4). This suggests that the underlying charge order associated with the $-3/5$ filling is less robust than that of the $-2/3$ state.

Temperature-dependent measurements and corresponding Arrhenius fits (Figs. 6.8c–e) reinforce this interpretation, revealing a smaller activation gap for the $-3/5$ FCI relative to $-2/3$. These distinctions underscore how subtle changes in filling, symmetry, and electric field tuning can drive transitions between distinct many-body phases—including FCIs, charge-ordered states, and ferromagnetic metals—within the same moiré flat band framework.

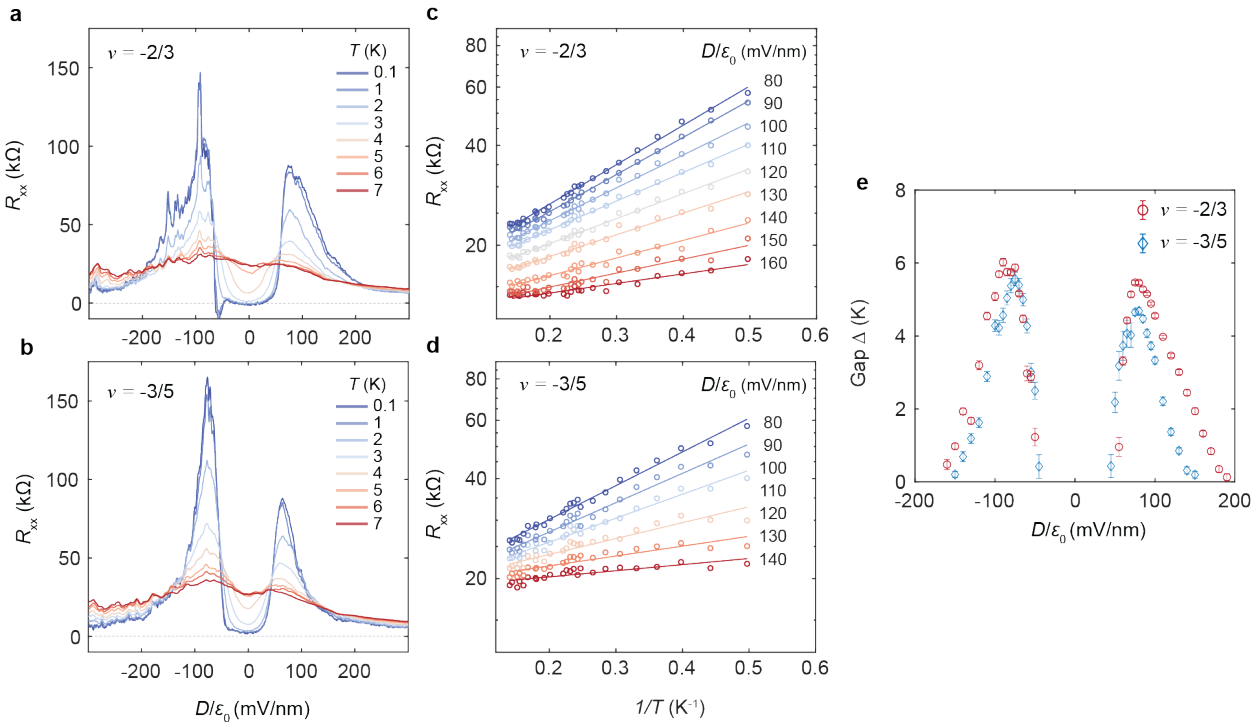

Figure 6.8: Electric-field dependent phase transition. **a-b,** Temperature-dependent R_{xx} versus D/ε_0 at $\nu = -2/3$ (a) and $\nu = -3/5$ (b). Both states show vanishing R_{xx} at low D/ε_0, signaling incompressible FCI phases. Increasing $|D/\varepsilon_0|$ induces transitions to insulating and then metallic regimes. **c-d,** Arrhenius plots of R_{xx} at fixed D/ε_0 for $\nu = -2/3$ (c) and $\nu = -3/5$ (d), fitted to $R_{xx} \propto R_0 \exp(-\Delta/2k_BT)$ to extract activation gaps. **e,** Extracted energy gaps Δ versus D/ε_0 for both fillings.

6.4 Temperature Dependence and Energy Gap Extraction of FCI States

To quantify the excitation gaps of various fractional Chern insulator (FCI) phases, we performed temperature-dependent transport measurements across a wide range of carrier fillings. Figures 6.9a and b display the evolution of R_{xx} and $-R_{xy}$, respectively, as functions of temperature and moiré filling factor v. The measurements were symmetrized and antisymmetrized at $\mu_0 H = \pm 150\,\mathrm{mT}$.

Figures 6.9c and d present representative line cuts at selected temperatures. In the quantum anomalous Hall (QAH) state at $v = -1$, R_{xx} remains notably suppressed at $\sim 5\,\mathrm{k\Omega}$ even at 14 K—the upper temperature bound of our dilution refrigerator. Simultaneously, the Hall resistance $|R_{xy}|$ stays near $15\,\mathrm{k\Omega}$, corresponding to a large Hall angle $\tan(\theta_H) \approx 3$. The thermal robustness of

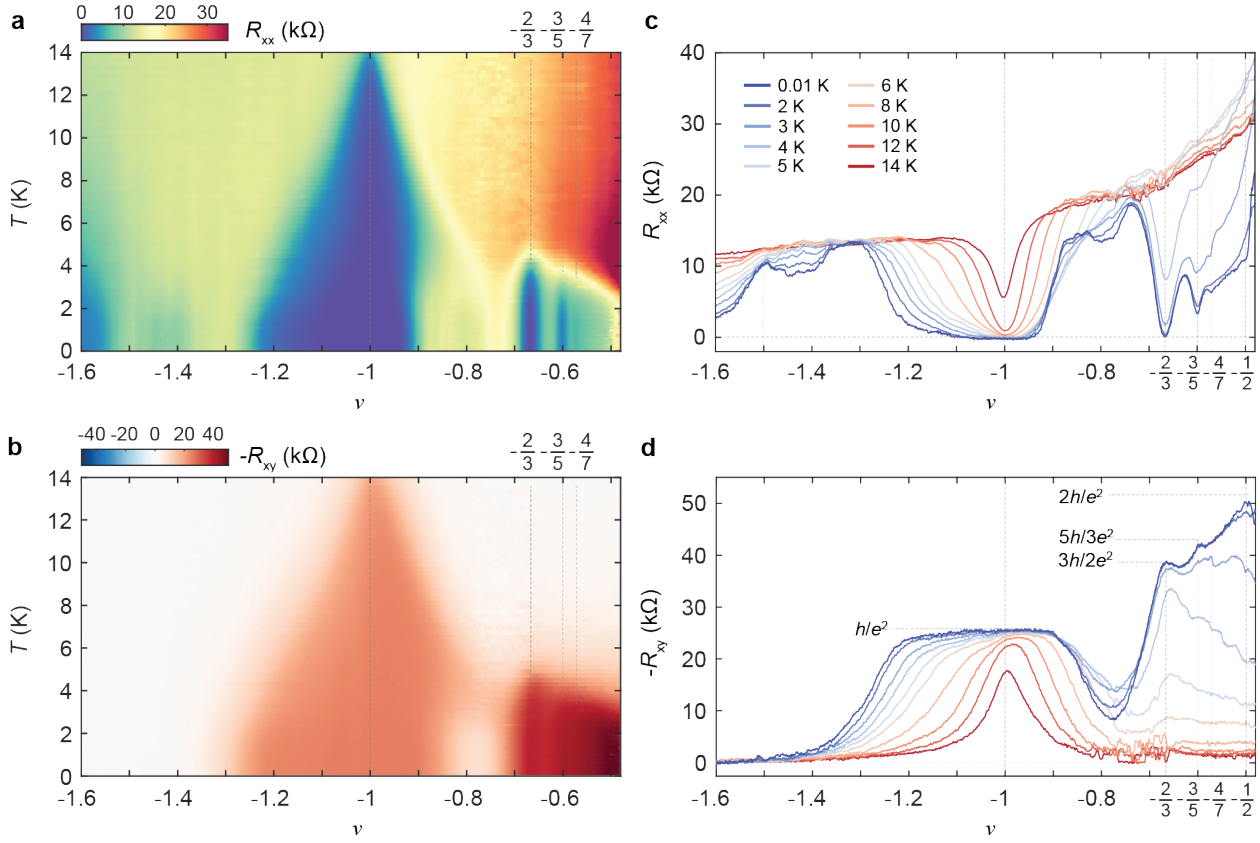

Figure 6.9: Temperature evolution of longitudinal and Hall resistances. **a-b,** Color maps of symmetrized R_{xx} (a) and antisymmetrized $-R_{xy}$ (b) versus filling factor ν and temperature T from 10 mK to 14 K, measured under $\mu_0 H = \pm 150$ mT. **c-d,** Linecuts of R_{xx} (c) and R_{xy} (d) extracted from panels (a) and (b), respectively, at selected temperatures.

fractional states follows a Jain-like hierarchy with filling factors matching $|p/(2p-1)|$ for integers $p = 2, 3, 4$. These fractional states persist up to ∼5 K, where $\tan(\theta_H)$ remains around unity, marking the upper thermal limit for quantized behavior.

We extract the longitudinal and Hall resistances for the $\nu = -2/3$ and $-3/5$ states and plot them in Figs. 6.10. For the $-2/3$ FCI, R_{xx} is negligible and $|R_{xy}|$ remains quantized from the base temperature of 10 mK up to ∼2.5 K, showing robust quantization over two decades in temperature. This stands in contrast to behaviors seen in rhombohedral pentalayer graphene [183], where a crossover occurs from a fractional Hall state with $|R_{xy}| \approx \frac{3}{2} h/e^2$ at 400 mK to a fully quantized QAH regime at ∼40 mK—interpreted as a transition between FQAH and a spin-polarized integer phase.

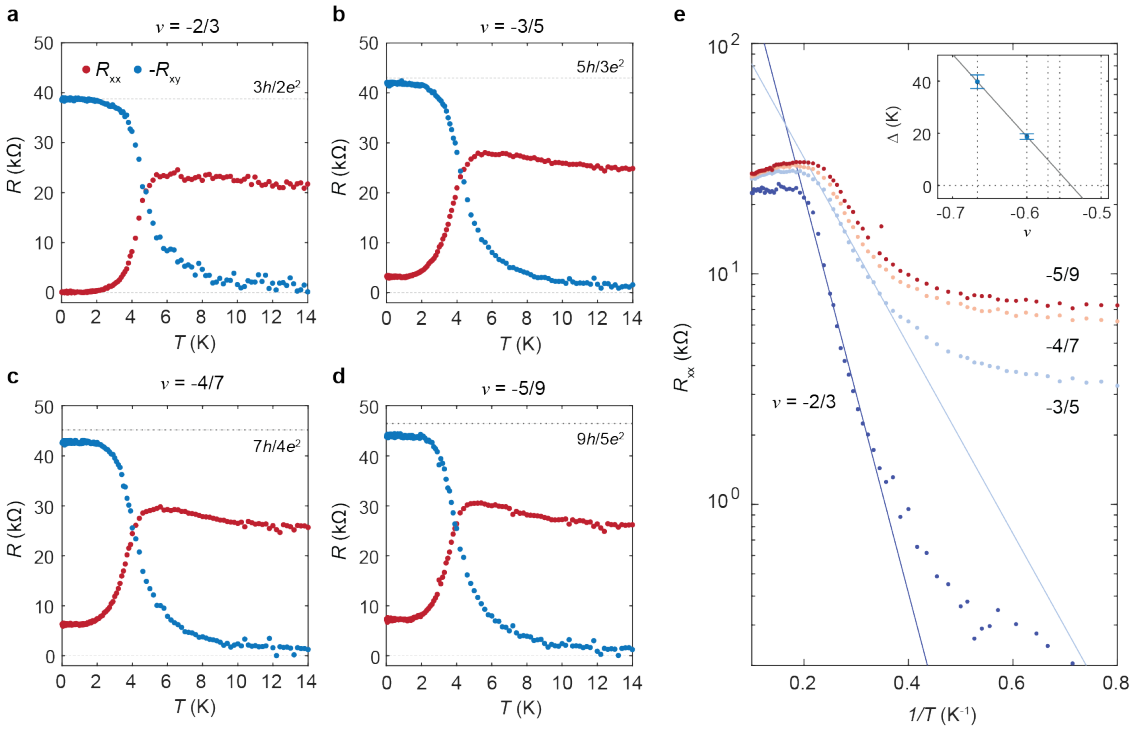

Figure 6.10: Thermal activation analysis of FCI states. **a**, Longitudinal resistance R_{xx} (symmetrized) and transverse resistance $-R_{xy}$ (antisymmetrized) measured at $\mu_0 H = \pm 150$ mT for the $\nu = -2/3$ state. **b**–**d**, Corresponding data for the $\nu = -3/5$, $-4/7$, and $-5/9$ fractional states, respectively, taken under similar conditions. **e**, Arrhenius plots of R_{xx} as a function of inverse temperature $1/T$ for the four fractional states. The activation gaps Δ are extracted from fits using $R_{xx} \sim \exp(-\Delta/2k_BT)$. Inset shows the extracted gaps for $\nu = -2/3$ and $-3/5$, overlaid with a guide to the eye illustrating the expected scaling trend.

No such crossover is observed in our twisted $MoTe_2$ samples, where all FCIs remain topologically quantized throughout the temperature range examined.

To probe the nature of the excitation gap and its field dependence, we carried out temperature sweeps at multiple magnetic fields. Figure 6.11a shows R_{xx} as a function of temperature and ν at magnetic fields $\mu_0 H = 0$, 0.15, 0.5, and 2 T. For each field, we extract the thermally activated transport gap by fitting $R_{xx}(T)$ to the standard Arrhenius form:

$$R_{xx}(T) = R_0 \exp\left(-\frac{\Delta}{2k_BT}\right),$$

where R_0 is a prefactor, Δ is the energy gap, and k_B is Boltzmann's constant.

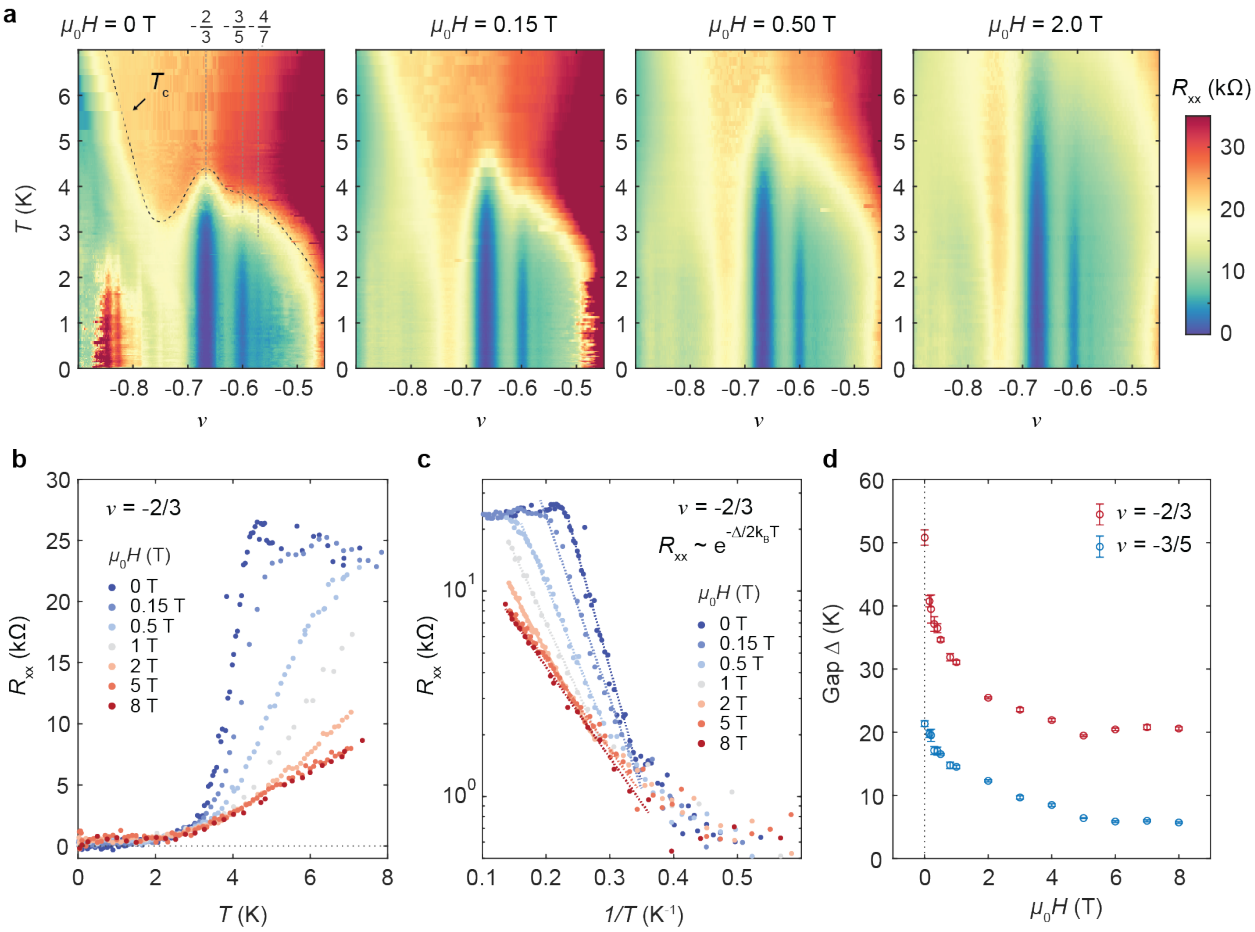

Figure 6.11: Magnetic field dependence of FCI activation gaps. **a,** Temperature-dependent longitudinal resistance R_{xx} across filling factor ν for magnetic fields $\mu_0 H = 0$, 0.15 T, 0.5 T, and 2 T. Dashed lines mark the Curie temperatures T_C determined from RMCD. **b,** R_{xx} versus T at $\nu = -2/3$ for each field, showing a decreasing trend in resistance with increasing T. **c,** Arrhenius analysis of the $-2/3$ state using $R_{xx} \sim \exp(-\Delta/2k_B T)$; fits show that the slope (and thus the activation gap Δ) diminishes with field. **d,** Extracted activation gaps Δ as a function of $\mu_0 H$ for both $\nu = -2/3$ (red) and $-3/5$ (blue).

Our analysis focuses on the $v = -2/3$ FCI state, for which R_{xx} vanishes over an extended temperature range, facilitating more reliable fitting. Figures 6.11b and c present the raw $R_{xx}(T)$ traces and the corresponding Arrhenius plots at different fields, respectively. The extracted gap Δ exhibits a pronounced dependence on magnetic field strength: at zero field, we find $\Delta = (52 \pm 4)\,\mathrm{K}$. This value steadily decreases to $\sim$30 K by $B \approx 1\,\mathrm{T}$, and saturates near 20 K at fields exceeding $\sim$4 T, as summarized in Fig. 6.11d.

6.5 Discussion

The observed reduction of the transport gap Δ with increasing magnetic field reveals a fundamental difference between fractional Chern insulators (FCIs) and conventional fractional quantum Hall (FQH) systems. In FQH states, the many-body energy gap typically scales as $\Delta \propto \sqrt{B}$ [178, 179, 185], due to its inverse dependence on the magnetic length $l_B \sim 26\,\mathrm{nm}/\sqrt{B}$. In contrast, FCIs are realized on periodic moiré lattices, where the interaction length is set by the lattice periodicity λ, making their energy scales largely independent of l_B and external magnetic field.

A hallmark of FCIs is the emergence of interaction-driven ferromagnetism that stabilizes their topological order [11]. This introduces a richer excitation spectrum than in spin-polarized FQH systems, especially at low fields where spin degrees of freedom are only weakly constrained by Zeeman energy. Our data show a strong field sensitivity of Δ at small B, which suggests the presence of multiple transport channels involving spin-flip (spinful) excitations [186].

Additional insight comes from comparing transport behavior with optical measurements of magnetic ordering. The dashed curve in Fig. 6.12 and Fig. 6.13 denotes the Curie temperature T_C extracted from RMCD. For the $\nu = -2/3$ state, we find $T_C \approx 4.2\,\mathrm{K}$, well below the transport gap Δ estimated from Arrhenius fits. Near T_C, $R_{xx}(T)$ rises sharply and saturates at $\sim$20–30 kΩ for $T > T_C$, consistent with the breakdown of long-range magnetic order and increased spin fluctuations.

These observations motivate a distinction between three energy scales that govern FCI physics:

- Δ_{FCI}: the intrinsic charge excitation gap associated with spin-conserving quasiparticles,

- Δ_S: a spin-flip activation gap, reflecting the energy cost of generating spinful charged excitations,

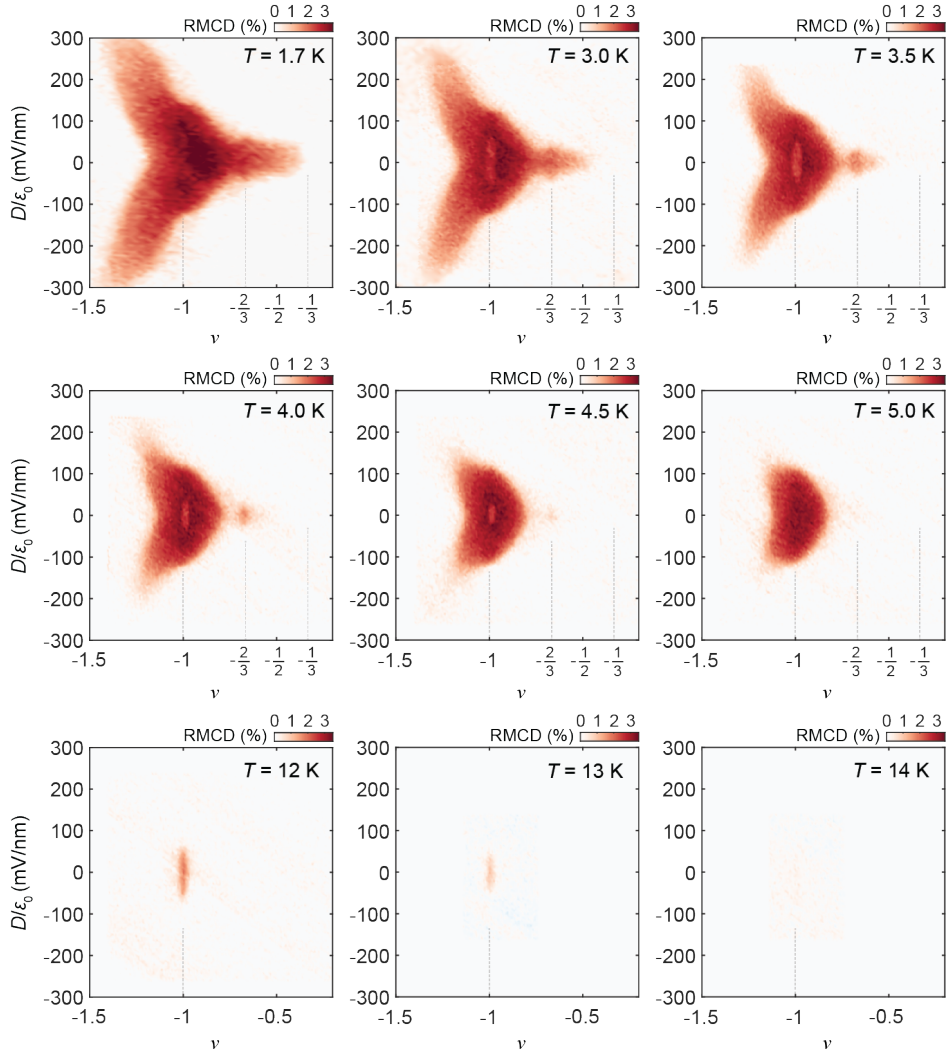

Figure 6.12: Temperature dependence of RMCD maps. RMCD signal as a function of ν and D/ε_0, measured under a small external magnetic field of 5 mT at various temperatures T.

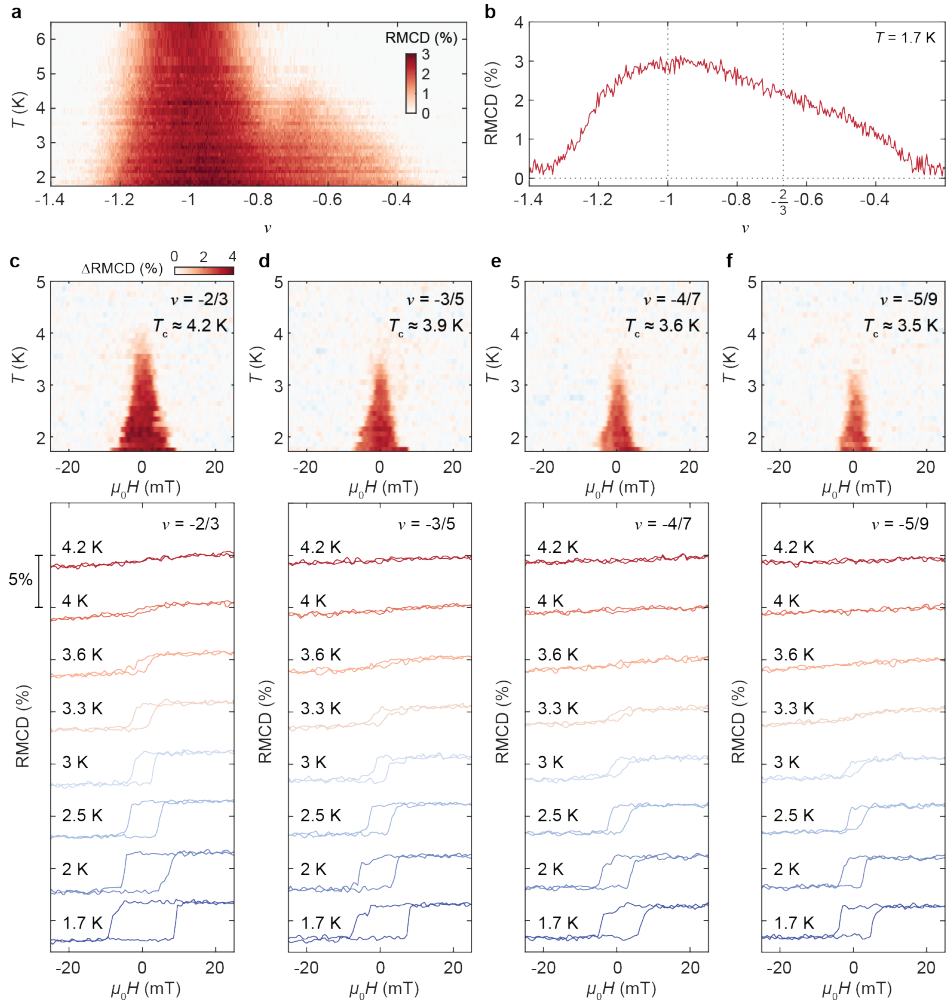

Figure 6.13: Extraction of Curie temperature. **a**, RMCD as a function of ν and temperature T at fixed displacement field $D/\varepsilon_0 = 0$ and external magnetic field $\mu_0 H = 30$ mT. **b**, RMCD linecut at $T = 1.6$ K, displaying a gradual decline in signal strength from $\nu = -1$ to $-2/3$. **c**–**f** (top), Hysteretic RMCD signal, ΔRMCD, plotted versus magnetic field and temperature for $\nu = -2/3$, $-3/5$, $-4/7$, and $-5/9$, corresponding to fractional Chern insulator states along the Jain sequence. **c**–**f** (bottom), Magnetic field sweeps at selected temperatures, extracted from the top panels.

- T_C: the magnetic ordering temperature determined by spontaneous valley/spin polarization.

At low magnetic fields, spinful excitations—possibly bound to magnons or involving internal spin texture—can dominate thermally activated transport. As B increases, Zeeman energy penalizes such excitations, reducing their contribution and allowing spinless, charge-only quasiparticles to dominate transport. This transition manifests as a saturation of the extracted transport gap Δ at high fields, converging to $\sim$20 K ($\approx$ 1.7 meV), consistent with prior local magnetometry estimates using nanoSQUID-on-tip techniques [154], which report $\sim$27 K, and theoretical calculations of the charge gap [186], which suggest $\sim$3.2 meV.

It is important to differentiate transport gaps—associated with the activation energy for dissociating individual charged quasiparticles—from *neutral* excitation gaps, which involve bound quasi-electron/quasi-hole pairs. While transport gaps control the dissipation onset in R_{xx}, neutral modes such as magnetorotons [187] or spin-wave-like collective excitations [188, 189] may influence the behavior of R_{xy} and set the temperature scale for quantized Hall transport. These neutral excitations mediate edge-bulk coupling and contribute to thermal broadening of quantization, even in the absence of charge dissipation.

A more comprehensive understanding of these excitations—particularly their dispersion and coupling to lattice or valley degrees of freedom—will require further experimental efforts, including high-resolution tunneling, microwave spectroscopy, or inelastic light scattering, as well as complementary theoretical modeling in strongly interacting topological flat bands.

We now examine how the energy gaps of fractional Chern insulators (FCIs) vary with filling factor. In the fractional quantum Hall (FQH) framework, composite fermion (CF) theory [119] predicts that excitation gaps scale approximately as $1/(2p+1)$, where p indexes the Jain sequence. However, establishing quantitative agreement between theory and experiment has proven challenging [190, 191, 192]. Empirically observed FQH gaps are often substantially lower than theoretical predictions, a discrepancy typically attributed to finite quantum well width and residual disorder [193, 194, 195, 196]. Nevertheless, in ultraclean GaAs quantum wells, recent experiments have confirmed the expected gap hierarchy with remarkable fidelity [197].

This raises a natural question: do FCIs follow a similar scaling behavior?

In our system, extracting a consistent hierarchy of gaps is complicated by the finite dissipation

observed in higher-order FCI states. For example, at fillings $v = -4/7$ and $-5/9$, R_{xx} remains appreciable even at the lowest temperatures (Fig. 6.10), which prevents reliable gap fitting using Arrhenius analysis. As a result, we focus on the more well-developed $v = -3/5$ state, where $R_{xx} \approx 2.5\,\mathrm{k}\Omega$ at base temperature allows a reasonable estimate of the activation gap.

From high-field data, we extract an energy gap $\Delta_{-3/5} \approx 6\,\mathrm{K}$, compared to $\Delta_{-2/3} \approx 20\,\mathrm{K}$ (see Fig. 6.11d). The ratio of these gaps, $\Delta_{-2/3}/\Delta_{-3/5} \approx 3.3$, is moderately larger than the 5/3 ratio suggested by the composite fermion scaling rule. This deviation may reflect enhanced sensitivity to disorder, lattice effects, or the breakdown of CF assumptions in strongly correlated moiré systems.

Future efforts aimed at improved sample quality—along with more direct probes of excitation gaps, such as compressibility or chemical potential measurements—will be essential for determining whether a universal FCI gap-scaling law emerges in the moiré context. As demonstrated historically in FQH systems, the resolution of fragile fractional states often hinges on eliminating extrinsic effects. Our results show that twisted $MoTe_2$ is capable of supporting multiple well-formed FCI phases, and continued refinement may unlock deeper insight into the interplay between topology, magnetism, and electron correlations in engineered flat bands.

Chapter 7

CONCLUDING REMARKS

The central goal of this thesis has been to uncover how strong electron–electron interactions, when combined with nontrivial band topology, give rise to new quantum phases in moiré transition metal dichalcogenides (TMDs). Over the course of my Ph.D., I have investigated both bosonic and fermionic manifestations of correlation, developed novel device architectures and measurement strategies, and applied these to explore a range of correlated and topological states—from excitonic lattices to dissipationless fractional Chern insulators.

The first part of this thesis focused on WSe_2/WS_2 moiré heterobilayers, where interlayer excitons experience a periodic moiré potential. Using optical spectroscopy, we probed interaction-driven shifts in excitonic resonances, connecting these to models of bosonic particles in a Hubbard-like lattice. This provided an experimental framework for studying strongly interacting bosonic systems in a clean, gate-tunable setting.

The subsequent chapters turned to twisted $MoTe_2$ bilayers as a platform for realizing fractional quantum anomalous Hall (FQAH) states. By engineering flat Chern bands and tuning them into strongly interacting regimes, we achieved the first observation of an FQAH effect at zero magnetic field. This constituted direct evidence of a fractional Chern insulator (FCI) phase emerging from purely interaction-driven physics in a lattice Chern band.

To confirm the topological character of these states beyond transport signatures, we employed cryogenic scanning microwave impedance microscopy to image their edge structure in real space. This provided the first spatially resolved visualization of fractional edge channels in any condensed matter system, revealing their confinement and continuity around device boundaries.

The thesis then expanded to explore higher Chern number minibands in twisted $MoTe_2$, motivated by analogies to higher Landau levels. These experiments uncovered interaction-driven ferromagnetism and topological behavior distinct from the $C = \pm 1$ regime, offering insight into how band geometry and Berry curvature influence correlated phases.

Finally, we realized a dissipationless FCI in twisted $MoTe_2$, combining robust fractional quantization with vanishing longitudinal resistance. By systematically mapping the activation gaps as a function of displacement field, filling factor, and magnetic field, we identified both spinful and spinless quasiparticle excitations, shedding light on the internal structure of the fractional phase.

Taken together, these results present a coherent experimental narrative that links bosonic and fermionic correlation physics, local and global probes, and integer and fractional topological order. In the sections that follow, I will outline the open questions that remain for zero-field FCIs—ranging from the dynamics of their quasiparticles to the interplay between FCIs and other correlated phases—and discuss how future experiments might address them.

7.1 Open Questions and Future Directions

The results presented in this thesis establish twisted $MoTe_2$ as a fertile platform for realizing fractional Chern insulators (FCIs) and other exotic correlated phases at zero magnetic field. Yet, many fundamental questions remain, both at the conceptual level and in terms of experimental verification. In this section, I outline several pressing directions for future investigation.

How Do FCIs Differ Fundamentally from FQH States?

FCIs share many phenomenological features with FQH states—such as fractionally quantized Hall conductance and anyonic quasiparticles—but they arise from a fundamentally different microscopic setting. In the FQH regime, electrons occupy perfectly flat Landau levels with translational symmetry in momentum space, resulting in uniform Berry curvature and quantum metric. This homogeneity simplifies the many-body problem and maximizes the stability of fractional states.

By contrast, FCIs are realized in lattice Chern bands that generally retain finite bandwidth and exhibit nonuniform quantum geometry. The Berry curvature and quantum metric can vary strongly across the Brillouin zone, introducing an additional energy scale that competes with electron–electron interactions. These inhomogeneities can alter excitation spectra, energy gaps, and change the relative stability of competing phases compared to their Landau-level counterparts.

Another key distinction lies in the breaking of time-reversal symmetry. In FQH systems, this symmetry is explicitly broken by the external magnetic field. In FCIs—such as those in moiré

TMDs—time-reversal symmetry is broken spontaneously, often through interaction-driven ferromagnetism. This mechanism can lead to different scaling behavior of the many-body gap and distinct quasiparticle properties.

The lattice setting also offers tuning knobs absent in conventional FQH systems. In moiré TMD FCIs, an applied displacement field can continuously modify the band structure and Berry curvature distribution, driving transitions between FCI phases, metallic Fermi liquids, and charge-ordered states. Furthermore, moiré superlattices can host higher-Chern-number bands with multiple chiralities, opening the door to correlated phases with no direct analog in a single Landau level.

In essence, FCIs and FQH states occupy the same topological framework but differ in their geometric, symmetry, and tunability landscape. Understanding how these differences shape quasiparticle structure, stability, and phase competition remains an open problem—and addressing it will be key to both refining the theoretical description of lattice fractionalization and identifying new experimental pathways for engineering exotic quantum phases in moiré materials.

What is the nature of the zero-Field composite Fermi liquid phase?

Recent theoretical work [54, 55] has predicted the possibility of a composite Fermi liquid (CFL) phase in half-filled Chern bands at zero magnetic field. In conventional FQH systems, composite fermions emerge by binding electrons to an even number of flux quanta, effectively neutralizing the external magnetic field and forming a Fermi surface [22]. This picture is supported experimentally in GaAs-based 2DEGs through magnetic focusing [198, 199], surface acoustic wave measurements [120], and antidot lattice resonances [121].

The zero-field case poses a conceptual challenge: in the absence of an applied field, what is the microscopic mechanism by which holes in a half-filled Chern band bind to vortices? Preliminary optical spectroscopy in twisted $MoTe_2$ [200] has shown suppression of photoluminescence helicity not only in integer and fractional Chern insulators but also at $\nu = -1/2$, consistent with a pseudogap expected for a CFL. Ferromagnetism appears to persist across much of the fractional filling range $-1 < \nu < -1/3$, suggesting a spin–valley–polarized Fermi liquid at half filling. Yet, key questions remain—such as the role of trion excitations and the relaxation pathways of fractionally charged

carriers.

Microwave impedance microscopy (MIM) measurements provide an additional clue: a subtle conductivity dip at $\nu = -1/2$ is observed in certain regions of the sample at $T \approx 500$ mK. Future MIM studies at dilution temperatures will be critical for determining whether this feature is an intrinsic property of a zero-field CFL.

Toward Zero-Field Non-Abelian Anyons

One of the most exciting motivations for studying zero-field FCIs is the possibility of realizing non-Abelian anyons for topologically protected quantum computation [201]. In such schemes, quantum information is encoded in the ground-state manifold of a non-Abelian phase and manipulated through braiding operations, making the system inherently fault-tolerant against local perturbations.

Analogous to the Moore–Read state at $\nu = 5/2$ and the Read–Rezayi state at $\nu = 12/5$ in GaAs, non-Abelian zero-field states could be engineered in twisted $MoTe_2$ by two main routes. The first is to stabilize even-denominator FCIs in higher-Chern-number minibands, as explored in Chapter 5. The second is to emulate bilayer quantum well systems [202] by fabricating two twisted $MoTe_2$ bilayers separated by a thin hBN spacer, thereby creating coupled $C = 1$ bands whose half-filled state may realize a Pfaffian-like phase.

Hybridizing FCIs with Superconductivity

An alternative pathway to non-Abelian excitations is to interface an Abelian FCI with a superconductor, potentially giving rise to parafermionic bound states [203, 204, 205]. This is particularly appealing for zero-field systems, where superconductivity can survive without being quenched by large magnetic fields. In twisted $MoTe_2$, one approach is to use Pd contacts that react with Te to form superconducting $PdTe_x$ [206], enabling proximity-induced superconductivity in edge channels. Achieving this will require careful optimization of interface quality, work function alignment, and the preservation of topological edge modes under superconducting proximity.

Beyond proximity effects, the idea of anyon superconductivity [207, 208]—where doping away from a commensurate fractional filling induces a superconducting condensate of anyons—is another

tantalizing prospect. Recent experiments have hinted at superconductivity in twisted $MoTe_2$ [209] and even possible chiral superconductivity with time-reversal symmetry breaking [210], although these findings require further confirmation and systematic study.

7.2 Final Remarks

In just a few years, twisted $MoTe_2$ has transformed from a theoretically intriguing proposal to a leading experimental platform for exploring interaction-driven topological phases in zero magnetic field. The pace of discovery has been remarkable, supported not only by established techniques but also by a growing suite of experimental approaches. Ongoing efforts include the application of scanning single-electron transistors, SQUID magnetometry, diamond-NV magnetometry, terahertz spectroscopy, angle-resolved photoemission, and millikelvin optics to probe the microscopic properties of moiré systems with unprecedented resolution. This diversity of perspectives is essential: each technique reveals a different facet of the underlying physics, and together they provide the understanding required to tackle the most challenging open questions.

Looking ahead, the convergence of high-quality material growth, precision device engineering, and increasingly sophisticated local probes promises to take the field into uncharted territory. With persistence—and perhaps a measure of good fortune—moiré TMDs may yet provide the long-sought platform that unites all four pillars of condensed matter physics: strong correlations, nontrivial topology, magnetism, and superconductivity.

BIBLIOGRAPHY

[1] M Zahid Hasan and Charles L Kane. Colloquium: topological insulators. *Reviews of modern physics*, 82(4):3045–3067, 2010.

[2] Bernhard Keimer and Joel E Moore. The physics of quantum materials. *Nature Physics*, 13(11):1045–1055, 2017.

[3] Charles L Kane and Eugene J Mele. Quantum spin hall effect in graphene. *Physical review letters*, 95(22):226801, 2005.

[4] Xiao-Liang Qi and Shou-Cheng Zhang. Topological insulators and superconductors. *Reviews of modern physics*, 83(4):1057–1110, 2011.

[5] Philip W Anderson. More is different: broken symmetry and the nature of the hierarchical structure of science. *Science*, 177(4047):393–396, 1972.

[6] Robert B Laughlin. Anomalous quantum hall effect: an incompressible quantum fluid with fractionally charged excitations. *Physical Review Letters*, 50(18):1395, 1983.

[7] Assa Auerbach. *Interacting electrons and quantum magnetism*. Springer Science & Business Media, 2012.

[8] Bevin Huang, Genevieve Clark, Efrén Navarro-Moratalla, Dahlia R Klein, Ran Cheng, Kyle L Seyler, Ding Zhong, Emma Schmidgall, Michael A McGuire, David H Cobden, et al. Layer-dependent ferromagnetism in a van der waals crystal down to the monolayer limit. *Nature*, 546(7657):270–273, 2017.

[9] Cheng Gong, Lin Li, Zhenglu Li, Huiwen Ji, Alex Stern, Yang Xia, Ting Cao, Wei Bao, Chenzhe Wang, Yuan Wang, et al. Discovery of intrinsic ferromagnetism in two-dimensional van der waals crystals. *Nature*, 546(7657):265–269, 2017.

[10] Yuan Cao, Valla Fatemi, Shiang Fang, Kenji Watanabe, Takashi Taniguchi, Efthimios Kaxiras, and Pablo Jarillo-Herrero. Unconventional superconductivity in magic-angle graphene superlattices. *Nature*, 556(7699):43–50, 2018.

[11] Jiaqi Cai, Eric Anderson, Chong Wang, Xiaowei Zhang, Xiaoyu Liu, William Holtzmann, Yinong Zhang, Fengren Fan, Takashi Taniguchi, Kenji Watanabe, et al. Signatures of fractional quantum anomalous hall states in twisted mote2. *Nature*, 622(7981):63–68, 2023.

[12] Yihang Zeng, Zhengchao Xia, Kaifei Kang, Jiacheng Zhu, Patrick Knüppel, Chirag Vaswani, Kenji Watanabe, Takashi Taniguchi, Kin Fai Mak, and Jie Shan. Thermodynamic evidence of fractional chern insulator in moiré mote2. *Nature*, 622(7981):69–73, 2023.

[13] Heonjoon Park, Jiaqi Cai, Eric Anderson, Yinong Zhang, Jiayi Zhu, Xiaoyu Liu, Chong Wang, William Holtzmann, Chaowei Hu, Zhaoyu Liu, et al. Observation of fractionally quantized anomalous hall effect. *Nature*, 622(7981):74–79, 2023.

[14] Fan Xu, Zheng Sun, Tongtong Jia, Chang Liu, Cheng Xu, Chushan Li, Yu Gu, Kenji Watanabe, Takashi Taniguchi, Bingbing Tong, et al. Observation of integer and fractional quantum anomalous hall effects in twisted bilayer mote 2. *Physical Review X*, 13(3):031037, 2023.

[15] K v Klitzing, Gerhard Dorda, and Michael Pepper. New method for high-accuracy determination of the fine-structure constant based on quantized hall resistance. *Physical review letters*, 45(6):494, 1980.

[16] Bertrand I Halperin. Quantized hall conductance, current-carrying edge states, and the existence of extended states in a two-dimensional disordered potential. *Physical review B*, 25(4):2185, 1982.

[17] David J Thouless, Mahito Kohmoto, M Peter Nightingale, and Marcel den Nijs. Quantized hall conductance in a two-dimensional periodic potential. *Physical review letters*, 49(6):405, 1982.

[18] F Duncan M Haldane. Model for a quantum hall effect without landau levels: Condensed-matter realization of the" parity anomaly". *Physical review letters*, 61(18):2015, 1988.

[19] Cui-Zu Chang, Jinsong Zhang, Xiao Feng, Jie Shen, Zuocheng Zhang, Minghua Guo, Kang Li, Yunbo Ou, Pang Wei, Li-Li Wang, et al. Experimental observation of the quantum anomalous hall effect in a magnetic topological insulator. *Science*, 340(6129):167–170, 2013.

[20] Markus Konig, Steffen Wiedmann, Christoph Brune, Andreas Roth, Hartmut Buhmann, Laurens W Molenkamp, Xiao-Liang Qi, and Shou-Cheng Zhang. Quantum spin hall insulator state in hgte quantum wells. *Science*, 318(5851):766–770, 2007.

[21] D. C. Tsui, H. L. Stormer, and A. C. Gossard. Two-dimensional magnetotransport in the extreme quantum limit. *Phys. Rev. Lett.*, 48:1559–1562, 1982.

[22] Jainendra K Jain. Composite-fermion approach for the fractional quantum hall effect. *Physical review letters*, 63(2):199, 1989.

[23] Jon M Leinaas and Jan Myrheim. On the theory of identical particles. *Il Nuovo Cimento B (1971-1996)*, 37(1):1–23, 1977.

[24] Frank Wilczek. Quantum mechanics of fractional-spin particles. *Physical review letters*, 49(14):957, 1982.

[25] Bertrand I Halperin. Statistics of quasiparticles and the hierarchy of fractional quantized hall states. *Physical Review Letters*, 52(18):1583, 1984.

[26] James Nakamura, Shuang Liang, Geoffrey C Gardner, and Michael J Manfra. Direct observation of anyonic braiding statistics. *Nature Physics*, 16(9):931–936, 2020.

[27] Hugo Bartolomei, Manohar Kumar, Rémi Bisognin, Arthur Marguerite, J-M Berroir, Erwann Bocquillon, Bernard Placais, Antonella Cavanna, Quan Dong, Ulf Gennser, et al. Fractional statistics in anyon collisions. *Science*, 368(6487):173–177, 2020.

[28] DN Sheng, Zheng-Cheng Gu, Kai Sun, and L Sheng. Fractional quantum hall effect in the absence of landau levels. *Nature communications*, 2(1):389, 2011.

[29] Titus Neupert, Luiz Santos, Claudio Chamon, and Christopher Mudry. Fractional quantum hall states at zero magnetic field. *Physical review letters*, 106(23):236804, 2011.

[30] Evelyn Tang, Jia-Wei Mei, and Xiao-Gang Wen. High-temperature fractional quantum hall states. *Physical review letters*, 106(23):236802, 2011.

[31] Nicolas Regnault and B Andrei Bernevig. Fractional chern insulator. *Physical Review X*, 1(2):021014, 2011.

[32] Di Xiao, Wenguang Zhu, Ying Ran, Naoto Nagaosa, and Satoshi Okamoto. Interface engineering of quantum hall effects in digital transition metal oxide heterostructures. *Nature communications*, 2(1):596, 2011.

[33] Kostya S Novoselov, Andre K Geim, Sergei V Morozov, De-eng Jiang, Yanshui Zhang, Sergey V Dubonos, Irina V Grigorieva, and Alexandr A Firsov. Electric field effect in atomically thin carbon films. *science*, 306(5696):666–669, 2004.

[34] Kostya S Novoselov, Da Jiang, F Schedin, TJ Booth, VV Khotkevich, SV Morozov, and Andre K Geim. Two-dimensional atomic crystals. *Proceedings of the National Academy of Sciences*, 102(30):10451–10453, 2005.

[35] Andre K Geim and Irina V Grigorieva. Van der waals heterostructures. *Nature*, 499(7459):419–425, 2013.

[36] Fengcheng Wu, Timothy Lovorn, Emanuel Tutuc, and Allan H MacDonald. Hubbard model physics in transition metal dichalcogenide moiré bands. *Physical review letters*, 121(2):026402, 2018.

[37] Cory R Dean, Andrea F Young, Inanc Meric, Chris Lee, Lei Wang, Sebastian Sorgenfrei, Kenji Watanabe, Takashi Taniguchi, Phillip Kim, Kenneth L Shepard, et al. Boron nitride substrates for high-quality graphene electronics. *Nature nanotechnology*, 5(10):722–726, 2010.

[38] Daniil Domaretskiy, Zefei Wu, Van Huy Nguyen, Ned Hayward, Ian Babich, Xiao Li, Ekaterina Nguyen, Julien Barrier, Kornelia Indykiewicz, Wendong Wang, et al. Proximity screening greatly enhances electronic quality of graphene. *arXiv preprint arXiv:2507.21997*, 2025.

[39] Qi Zhang, Xue-Feng Wang, Shu-Hong Shen, Qi Lu, Xiaozhi Liu, Haoyi Li, Jingying Zheng,

Chu-Ping Yu, Xiaoyan Zhong, Lin Gu, et al. Simultaneous synthesis and integration of two-dimensional electronic components. *Nature Electronics*, 2(4):164–170, 2019.

[40] Chunsen Liu, Huawei Chen, Shuiyuan Wang, Qi Liu, Yu-Gang Jiang, David Wei Zhang, Ming Liu, and Peng Zhou. Two-dimensional materials for next-generation computing technologies. *Nature nanotechnology*, 15(7):545–557, 2020.

[41] Rafi Bistritzer and Allan H MacDonald. Moiré bands in twisted double-layer graphene. *Proceedings of the National Academy of Sciences*, 108(30):12233–12237, 2011.

[42] Yuan Cao, Valla Fatemi, Ahmet Demir, Shiang Fang, Spencer L Tomarken, Jason Y Luo, Javier D Sanchez-Yamagishi, Kenji Watanabe, Takashi Taniguchi, Efthimios Kaxiras, et al. Correlated insulator behaviour at half-filling in magic-angle graphene superlattices. *Nature*, 556(7699):80–84, 2018.

[43] Hoi Chun Po, Liujun Zou, Ashvin Vishwanath, and T Senthil. Origin of mott insulating behavior and superconductivity in twisted bilayer graphene. *Physical Review X*, 8(3):031089, 2018.

[44] Zhida Song, Zhijun Wang, Wujun Shi, Gang Li, Chen Fang, and B Andrei Bernevig. All magic angles in twisted bilayer graphene are topological. *Physical review letters*, 123(3):036401, 2019.

[45] Aaron L Sharpe, Eli J Fox, Arthur W Barnard, Joe Finney, Kenji Watanabe, Takashi Taniguchi, MA Kastner, and David Goldhaber-Gordon. Emergent ferromagnetism near three-quarters filling in twisted bilayer graphene. *Science*, 365(6453):605–608, 2019.

[46] Marec Serlin, CL Tschirhart, Hryhoriy Polshyn, Yuxuan Zhang, Jiacheng Zhu, Kenji Watanabe, Takashi Taniguchi, L Balents, and AF Young. Intrinsic quantized anomalous hall effect in a moiré heterostructure. *Science*, 367(6480):900–903, 2020.

[47] Fengcheng Wu, Timothy Lovorn, Emanuel Tutuc, Ivar Martin, and AH MacDonald. Topological insulators in twisted transition metal dichalcogenide homobilayers. *Physical review letters*, 122(8):086402, 2019.

[48] Kin Fai Mak, Changgu Lee, James Hone, Jie Shan, and Tony F Heinz. Atomically thin mos 2: a new direct-gap semiconductor. *Physical review letters*, 105(13):136805, 2010.

[49] Andrea Splendiani, Liang Sun, Yuanbo Zhang, Tianshu Li, Jonghwan Kim, Chi-Yung Chim, Giulia Galli, and Feng Wang. Emerging photoluminescence in monolayer mos2. *Nano letters*, 10(4):1271–1275, 2010.

[50] Di Xiao, Gui-Bin Liu, Wanxiang Feng, Xiaodong Xu, and Wang Yao. Coupled spin and valley physics in monolayers of mos 2 and other group-vi dichalcogenides. *Physical review letters*, 108(19):196802, 2012.

[51] Yang Xu, Song Liu, Daniel A Rhodes, Kenji Watanabe, Takashi Taniguchi, James Hone, Veit Elser, Kin Fai Mak, and Jie Shan. Correlated insulating states at fractional fillings of moiré superlattices. *Nature*, 587(7833):214–218, 2020.

[52] Tingxin Li, Shengwei Jiang, Bowen Shen, Yang Zhang, Lizhong Li, Zui Tao, Trithep Devakul, Kenji Watanabe, Takashi Taniguchi, Liang Fu, et al. Quantum anomalous hall effect from intertwined moiré bands. *Nature*, 600(7890):641–646, 2021.

[53] Eric Anderson, Feng-Ren Fan, Jiaqi Cai, William Holtzmann, Takashi Taniguchi, Kenji Watanabe, Di Xiao, Wang Yao, and Xiaodong Xu. Programming correlated magnetic states with gate-controlled moiré geometry. *Science*, 381(6655):325–330, 2023.

[54] Junkai Dong, Jie Wang, Patrick J Ledwith, Ashvin Vishwanath, and Daniel E Parker. Composite fermi liquid at zero magnetic field in twisted mote 2. *Physical Review Letters*, 131(13):136502, 2023.

[55] Hart Goldman, Aidan P Reddy, Nisarga Paul, and Liang Fu. Zero-field composite fermi liquid in twisted semiconductor bilayers. *Physical Review Letters*, 131(13):136501, 2023.

[56] Aidan P Reddy, Faisal Alsallom, Yang Zhang, Trithep Devakul, and Liang Fu. Fractional quantum anomalous hall states in twisted bilayer mote2 and wse2. *Physical Review B*, 108(8):085117, 2023.

[57] Yujin Jia, Jiabin Yu, Jiaxuan Liu, Jonah Herzog-Arbeitman, Ziyue Qi, Hanqi Pi, Nicolas Regnault, Hongming Weng, B Andrei Bernevig, and Quansheng Wu. Moiré fractional chern insulators. i. first-principles calculations and continuum models of twisted bilayer mote2. *Physical Review B*, 109(20):205121, 2024.

[58] Zhurun Ji, Heonjoon Park, Mark E Barber, Chaowei Hu, Kenji Watanabe, Takashi Taniguchi, Jiun-Haw Chu, Xiaodong Xu, and Zhi-Xun Shen. Local probe of bulk and edge states in a fractional chern insulator. *Nature*, 635(8039):578–583, 2024.

[59] Heonjoon Park, Jiayi Zhu, Xi Wang, Yingqi Wang, William Holtzmann, Takashi Taniguchi, Kenji Watanabe, Jiaqiang Yan, Liang Fu, Ting Cao, et al. Dipole ladders with large hubbard interaction in a moiré exciton lattice. *Nature Physics*, 19(9):1286–1292, 2023.

[60] Heonjoon Park, Jiaqi Cai, Eric Anderson, Xiao-Wei Zhang, Xiaoyu Liu, William Holtzmann, Weijie Li, Chong Wang, Chaowei Hu, and Yuzhou Zhao. Ferromagnetism and topology of the higher flat band in a fractional chern insulator. *Nature Physics*, pages 1–7, 2025.

[61] Heonjoon Park, Weijie Li, Chaowei Hu, Christiano Beach, Miguel Gonçalves, Juan Felipe Mendez-Valderrama, Jonah Herzog-Arbeitman, Takashi Taniguchi, Kenji Watanabe, David Cobden, et al. Observation of high-temperature dissipationless fractional chern insulator. *arXiv preprint arXiv:2503.10989*, 2025.

[62] Yanhao Tang, Lizhong Li, Tingxin Li, Yang Xu, Song Liu, Katayun Barmak, Kenji Watanabe, Takashi Taniguchi, Allan H MacDonald, Jie Shan, et al. Simulation of hubbard model physics in wse2/ws2 moiré superlattices. *Nature*, 579(7799):353–358, 2020.

[63] Emma C Regan, Danqing Wang, Chenhao Jin, M Iqbal Bakti Utama, Beini Gao, Xin Wei, Sihan Zhao, Wenyu Zhao, Zuocheng Zhang, Kentaro Yumigeta, et al. Mott and generalized wigner crystal states in wse2/ws2 moiré superlattices. *Nature*, 579(7799):359–363, 2020.

[64] Erfu Liu, Takashi Taniguchi, Kenji Watanabe, Nathaniel M Gabor, Yong-Tao Cui, and Chun Hung Lui. Excitonic and valley-polarization signatures of fractional correlated electronic phases in a wse 2/ws 2 moiré superlattice. *Physical Review Letters*, 127(3):037402, 2021.

[65] Shengnan Miao, Tianmeng Wang, Xiong Huang, Dongxue Chen, Zhen Lian, Chong Wang, Mark Blei, Takashi Taniguchi, Kenji Watanabe, Sefaattin Tongay, et al. Strong interaction between interlayer excitons and correlated electrons in wse2/ws2 moiré superlattice. *Nature communications*, 12(1):3608, 2021.

[66] Xi Wang, Chengxin Xiao, Heonjoon Park, Jiayi Zhu, Chong Wang, Takashi Taniguchi, Kenji Watanabe, Jiaqiang Yan, Di Xiao, Daniel R Gamelin, et al. Light-induced ferromagnetism in moiré superlattices. *Nature*, 604(7906):468–473, 2022.

[67] Hongyuan Li, Shaowei Li, Emma C Regan, Danqing Wang, Wenyu Zhao, Salman Kahn, Kentaro Yumigeta, Mark Blei, Takashi Taniguchi, Kenji Watanabe, et al. Imaging two-dimensional generalized wigner crystals. *Nature*, 597(7878):650–654, 2021.

[68] You Zhou, Jiho Sung, Elise Brutschea, Ilya Esterlis, Yao Wang, Giovanni Scuri, Ryan J Gelly, Hoseok Heo, Takashi Taniguchi, Kenji Watanabe, et al. Bilayer wigner crystals in a transition metal dichalcogenide heterostructure. *Nature*, 595(7865):48–52, 2021.

[69] Tomasz Smoleński, Pavel E Dolgirev, Clemens Kuhlenkamp, Alexander Popert, Yuya Shimazaki, Patrick Back, Xiaobo Lu, Martin Kroner, Kenji Watanabe, Takashi Taniguchi, et al. Signatures of wigner crystal of electrons in a monolayer semiconductor. *Nature*, 595(7865):53–57, 2021.

[70] Yuya Shimazaki, Ido Schwartz, Kenji Watanabe, Takashi Taniguchi, Martin Kroner, and Ataç Imamoğlu. Strongly correlated electrons and hybrid excitons in a moiré heterostructure. *Nature*, 580(7804):472–477, 2020.

[71] Xiong Huang, Tianmeng Wang, Shengnan Miao, Chong Wang, Zhipeng Li, Zhen Lian, Takashi Taniguchi, Kenji Watanabe, Satoshi Okamoto, Di Xiao, et al. Correlated insulating states at fractional fillings of the ws2/wse2 moiré lattice. *Nature Physics*, 17(6):715–719, 2021.

[72] Pasqual Rivera, John R Schaibley, Aaron M Jones, Jason S Ross, Sanfeng Wu, Grant Aivazian, Philip Klement, Kyle Seyler, Genevieve Clark, Nirmal J Ghimire, et al. Observation of long-

lived interlayer excitons in monolayer mose2–wse2 heterostructures. *Nature communications*, 6(1):6242, 2015.

[73] Weijie Li, Xin Lu, Sudipta Dubey, Luka Devenica, and Ajit Srivastava. Dipolar interactions between localized interlayer excitons in van der waals heterostructures. *Nature materials*, 19(6):624–629, 2020.

[74] Malte Kremser, Mauro Brotons-Gisbert, Johannes Knörzer, Janine Gückelhorn, Moritz Meyer, Matteo Barbone, Andreas V Stier, Brian D Gerardot, Kai Müller, and Jonathan J Finley. Discrete interactions between a few interlayer excitons trapped at a mose2–wse2 heterointerface. *npj 2D Materials and Applications*, 4(1):8, 2020.

[75] Pasqual Rivera, Kyle L Seyler, Hongyi Yu, John R Schaibley, Jiaqiang Yan, David G Mandrus, Wang Yao, and Xiaodong Xu. Valley-polarized exciton dynamics in a 2d semiconductor heterostructure. *Science*, 351(6274):688–691, 2016.

[76] Hongyi Yu, Gui-Bin Liu, Jianju Tang, Xiaodong Xu, and Wang Yao. Moiré excitons: From programmable quantum emitter arrays to spin-orbit–coupled artificial lattices. *Science advances*, 3(11):e1701696, 2017.

[77] Niclas Götting, Frederik Lohof, and Christopher Gies. Moiré-bose-hubbard model for interlayer excitons in twisted transition metal dichalcogenide heterostructures. *Physical Review B*, 105(16):165419, 2022.

[78] Matthew R Rosenberger, Hsun-Jen Chuang, Kathleen M McCreary, Aubrey T Hanbicki, Saujan V Sivaram, and Berend T Jonker. Nano-"squeegee" for the creation of clean 2d material interfaces. *ACS applied materials & interfaces*, 10(12):10379–10387, 2018.

[79] Leo J McGilly, Alexander Kerelsky, Nathan R Finney, Konstantin Shapovalov, En-Min Shih, Augusto Ghiotto, Yihang Zeng, Samuel L Moore, Wenjing Wu, Yusong Bai, et al. Visualization of moiré superlattices. *Nature Nanotechnology*, 15(7):580–584, 2020.

[80] Erfu Liu, Jeremiah van Baren, Zhengguang Lu, Takashi Taniguchi, Kenji Watanabe, Dmitry Smirnov, Yia-Chung Chang, and Chun Hung Lui. Exciton-polaron rydberg states in monolayer mose2 and wse2. *Nature communications*, 12(1):6131, 2021.

[81] Xi Wang, Xiaowei Zhang, Jiayi Zhu, Heonjoon Park, Yingqi Wang, Chong Wang, William G Holtzmann, Takashi Taniguchi, Kenji Watanabe, Jiaqiang Yan, et al. Intercell moiré exciton complexes in electron lattices. *Nature Materials*, 22(5):599–604, 2023.

[82] Chenhao Jin, Zui Tao, Tingxin Li, Yang Xu, Yanhao Tang, Jiacheng Zhu, Song Liu, Kenji Watanabe, Takashi Taniguchi, James C Hone, et al. Stripe phases in wse2/ws2 moiré superlattices. *Nature Materials*, 20(7):940–944, 2021.

[83] Jue Wang, Jenny Ardelean, Yusong Bai, Alexander Steinhoff, Matthias Florian, Frank Jahnke, Xiaodong Xu, Mackillo Kira, James Hone, and X-Y Zhu. Optical generation of high carrier densities in 2d semiconductor heterobilayers. *Science Advances*, 5(9):eaax0145, 2019.

[84] Mit H Naik, Emma C Regan, Zuocheng Zhang, Yang-Hao Chan, Zhenglu Li, Danqing Wang, Yoseob Yoon, Chin Shen Ong, Wenyu Zhao, Sihan Zhao, et al. Intralayer charge-transfer moiré excitons in van der waals superlattices. *Nature*, 609(7925):52–57, 2022.

[85] Ouri Karni, Elyse Barré, Vivek Pareek, Johnathan D Georgaras, Michael KL Man, Chakradhar Sahoo, David R Bacon, Xing Zhu, Henrique B Ribeiro, Aidan L O'Beirne, et al. Structure of the moiré exciton captured by imaging its electron and hole. *Nature*, 603(7900):247–252, 2022.

[86] Sandhya Susarla, Mit H Naik, Daria D Blach, Jonas Zipfel, Takashi Taniguchi, Kenji Watanabe, Libai Huang, Ramamoorthy Ramesh, Felipe H da Jornada, Steven G Louie, et al. Hyperspectral imaging of exciton confinement within a moiré unit cell with a subnanometer electron probe. *Science*, 378(6625):1235–1239, 2022.

[87] Mete Atatüre, Dirk Englund, Nick Vamivakas, Sang-Yun Lee, and Joerg Wrachtrup. Material platforms for spin-based photonic quantum technologies. *Nature Reviews Materials*, 3(5):38–51, 2018.

[88] Kha Tran, Galan Moody, Fengcheng Wu, Xiaobo Lu, Junho Choi, Kyounghwan Kim, Amritesh Rai, Daniel A Sanchez, Jiamin Quan, Akshay Singh, et al. Evidence for moiré excitons in van der waals heterostructures. *Nature*, 567(7746):71–75, 2019.

[89] Yang Zhang, Noah FQ Yuan, and Liang Fu. Moiré quantum chemistry: charge transfer in transition metal dichalcogenide superlattices. *Physical Review B*, 102(20):201115, 2020.

[90] Kevin Slagle and Liang Fu. Charge transfer excitations, pair density waves, and superconductivity in moiré materials. *Physical Review B*, 102(23):235423, 2020.

[91] Xi Wang, Jiayi Zhu, Kyle L Seyler, Pasqual Rivera, Huiyuan Zheng, Yingqi Wang, Minhao He, Takashi Taniguchi, Kenji Watanabe, Jiaqiang Yan, et al. Moiré trions in mose2/wse2 heterobilayers. *Nature Nanotechnology*, 16(11):1208–1213, 2021.

[92] C Piermarocchi, Pochung Chen, LJ Sham, and DG Steel. Optical rkky interaction between charged semiconductor quantum dots. *Physical review letters*, 89(16):167402, 2002.

[93] Markus Greiner, Olaf Mandel, Tilman Esslinger, Theodor W Hänsch, and Immanuel Bloch. Quantum phase transition from a superfluid to a mott insulator in a gas of ultracold atoms. *nature*, 415(6867):39–44, 2002.

[94] Nathan Gemelke, Xibo Zhang, Chen-Lung Hung, and Cheng Chin. In situ observation of incompressible mott-insulating domains in ultracold atomic gases. *Nature*, 460(7258):995–998, 2009.

[95] Waseem S Bakr, Amy Peng, M Eric Tai, Ruichao Ma, Jonathan Simon, Jonathon I Gillen, Simon Foelling, Lode Pollet, and Markus Greiner. Probing the superfluid–to–mott insulator transition at the single-atom level. *Science*, 329(5991):547–550, 2010.

[96] Jacob F Sherson, Christof Weitenberg, Manuel Endres, Marc Cheneau, Immanuel Bloch, and Stefan Kuhr. Single-atom-resolved fluorescence imaging of an atomic mott insulator. *Nature*, 467(7311):68–72, 2010.

[97] Camille Lagoin, Utso Bhattacharya, Tobias Grass, RW Chhajlany, Tymoteusz Salamon, Kirk Baldwin, Loren Pfeiffer, Maciej Lewenstein, Markus Holzmann, and François Dubin. Extended bose–hubbard model with dipolar excitons. *Nature*, 609(7927):485–489, 2022.

[98] Camille Lagoin, Stephan Suffit, Kirk Baldwin, Loren Pfeiffer, and François Dubin. Mott

insulator of strongly interacting two-dimensional semiconductor excitons. *Nature Physics*, 18(2):149–153, 2022.

[99] Camille Lagoin, Stephan Suffit, Kirk Baldwin, Loren Pfeiffer, and François Dubin. Dual-density waves with neutral and charged dipolar excitons of gaas bilayers. *Nature Materials*, 22(2):170–174, 2023.

[100] Jie Gu, Liguo Ma, Song Liu, Kenji Watanabe, Takashi Taniguchi, James C Hone, Jie Shan, and Kin Fai Mak. Dipolar excitonic insulator in a moiré lattice. *Nature physics*, 18(4):395–400, 2022.

[101] Daniel Arovas, John R Schrieffer, and Frank Wilczek. Fractional statistics and the quantum hall effect. *Physical review letters*, 53(7):722, 1984.

[102] S C_ Zhang, Th H Hansson, and S Kivelson. Effective-field-theory model for the fractional quantum hall effect. *Physical review letters*, 62(1):82, 1989.

[103] Gregory Moore and Nicholas Read. Nonabelions in the fractional quantum hall effect. *Nuclear Physics B*, 360(2-3):362–396, 1991.

[104] Xiao-Gang Wen. Non-abelian statistics in the fractional quantum hall states. *Physical review letters*, 66(6):802, 1991.

[105] Cui-Zu Chang, Chao-Xing Liu, and Allan H MacDonald. Colloquium: Quantum anomalous hall effect. *Reviews of Modern Physics*, 95(1):011002, 2023.

[106] Yujun Deng, Yijun Yu, Meng Zhu Shi, Zhongxun Guo, Zihan Xu, Jing Wang, Xian Hui Chen, and Yuanbo Zhang. Quantum anomalous hall effect in intrinsic magnetic topological insulator mnbi2te4. *Science*, 367(6480):895–900, 2020.

[107] Benjamin A Foutty, Carlos R Kometter, Trithep Devakul, Aidan P Reddy, Kenji Watanabe, Takashi Taniguchi, Liang Fu, and Benjamin E Feldman. Mapping twist-tuned multiband topology in bilayer wse2. *Science*, 384(6693):343–347, 2024.

[108] Yonglong Xie, Andrew T Pierce, Jeong Min Park, Daniel E Parker, Eslam Khalaf, Patrick Ledwith, Yuan Cao, Seung Hwan Lee, Shaowen Chen, Patrick R Forrester, et al. Fractional chern insulators in magic-angle twisted bilayer graphene. *Nature*, 600(7889):439–443, 2021.

[109] Eric M Spanton, Alexander A Zibrov, Haoxin Zhou, Takashi Taniguchi, Kenji Watanabe, Michael P Zaletel, and Andrea F Young. Observation of fractional chern insulators in a van der waals heterostructure. *Science*, 360(6384):62–66, 2018.

[110] Hongyi Yu, Mingxing Chen, and Wang Yao. Giant magnetic field from moiré induced berry phase in homobilayer semiconductors. *National Science Review*, 7(1):12–20, 2020.

[111] P Streda. Theory of quantised hall conductivity in two dimensions. *Journal of Physics C: Solid State Physics*, 15(22):L717, 1982.

[112] Augusto Ghiotto, En-Min Shih, Giancarlo SSG Pereira, Daniel A Rhodes, Bumho Kim, Jiawei Zang, Andrew J Millis, Kenji Watanabe, Takashi Taniguchi, James C Hone, et al. Quantum criticality in twisted transition metal dichalcogenides. *Nature*, 597(7876):345–349, 2021.

[113] Lei Wang, En-Min Shih, Augusto Ghiotto, Lede Xian, Daniel A Rhodes, Cheng Tan, Martin Claassen, Dante M Kennes, Yusong Bai, Bumho Kim, et al. Correlated electronic phases in twisted bilayer transition metal dichalcogenides. *Nature materials*, 19(8):861–866, 2020.

[114] Taige Wang, Trithep Devakul, Michael P Zaletel, and Liang Fu. Diverse magnetic orders and quantum anomalous hall effect in twisted bilayer mote2 and wse2. *arXiv preprint arXiv:2306.02501*, 2023.

[115] Dan Shahar, DC Tsui, M Shayegan, RN Bhatt, and JE Cunningham. Universal conductivity at the quantum hall liquid to insulator transition. *Physical review letters*, 74(22):4511, 1995.

[116] Cui-Zu Chang, Weiwei Zhao, Jian Li, JK Jain, Chaoxing Liu, Jagadeesh S Moodera, and Moses HW Chan. Observation of the quantum anomalous hall insulator to anderson insulator quantum phase transition and its scaling behavior. *Physical review letters*, 117(12):126802, 2016.

[117] Chong Wang, Xiao-Wei Zhang, Xiaoyu Liu, Yuchi He, Xiaodong Xu, Ying Ran, Ting Cao, and Di Xiao. Fractional chern insulator in twisted bilayer mote2. *Physical Review Letters*, 132(3):036501, 2024.

[118] Robert Willett, James P Eisenstein, Horst L Störmer, Daniel C Tsui, Arthur C Gossard, and JH English. Observation of an even-denominator quantum number in the fractional quantum hall effect. *Physical review letters*, 59(15):1776, 1987.

[119] Bertrand I Halperin, Patrick A Lee, and Nicholas Read. Theory of the half-filled landau level. *Physical Review B*, 47(12):7312, 1993.

[120] RL Willett, RR Ruel, KW West, and LN Pfeiffer. Experimental demonstration of a fermi surface at one-half filling of the lowest landau level. *Physical review letters*, 71(23):3846, 1993.

[121] W Kang, HL Stormer, LN Pfeiffer, KW Baldwin, and KW West. How real are composite fermions? *Physical review letters*, 71(23):3850, 1993.

[122] RW Winkler, JP Kotthaus, and K Ploog. Landau band conductivity in a two-dimensional electron system modulated by an artificial one-dimensional superlattice potential. *Physical review letters*, 62(10):1177, 1989.

[123] Ady Stern. Anyons and the quantum hall effect—a pedagogical review. *Annals of Physics*, 323(1):204–249, 2008.

[124] VJ Goldman and Bo Su. Resonant tunneling in the quantum hall regime: measurement of fractional charge. *Science*, 267(5200):1010–1012, 1995.

[125] Jens Martin, Shahal Ilani, Basile Verdene, Jurgen Smet, Vladimir Umansky, Diana Mahalu, Dieter Schuh, Gerhard Abstreiter, and Amir Yacoby. Localization of fractionally charged quasi-particles. *Science*, 305(5686):980–983, 2004.

[126] Iuliana P Radu, JB Miller, CM Marcus, MA Kastner, LN Pfeiffer, and KW West. Quasi-particle properties from tunneling in the v= 5/2 fractional quantum hall state. *Science*, 320(5878):899–902, 2008.

[127] R De-Picciotto, M Reznikov, Moty Heiblum, V Umansky, G Bunin, and Diana Mahalu. Direct observation of a fractional charge. *Physica B: Condensed Matter*, 249:395–400, 1998.

[128] Nikola Pascher, Clemens Rössler, Thomas Ihn, Klaus Ensslin, Christian Reichl, and Werner Wegscheider. Imaging the conductance of integer and fractional quantum hall edge states. *Physical Review X*, 4(1):011014, 2014.

[129] AM Chang. Chiral luttinger liquids at the fractional quantum hall edge. *Reviews of Modern Physics*, 75(4):1449, 2003.

[130] Chetan Nayak, Steven H Simon, Ady Stern, Michael Freedman, and Sankar Das Sarma. Non-abelian anyons and topological quantum computation. *Reviews of Modern Physics*, 80(3):1083, 2008.

[131] RC Ashoori, HL Stormer, LN Pfeiffer, KW Baldwin, and K West. Edge magnetoplasmons in the time domain. *Physical Review B*, 45(7):3894, 1992.

[132] BK Stuhl, H-I Lu, LM Aycock, D Genkina, and IB Spielman. Visualizing edge states with an atomic bose gas in the quantum hall regime. *Science*, 349(6255):1514–1518, 2015.

[133] Ruixiao Yao, Sungjae Chi, Biswaroop Mukherjee, Airlia Shaffer, Martin Zwierlein, and Richard J Fletcher. Observation of chiral edge transport in a rapidly-rotating quantum gas. *arXiv preprint arXiv:2304.10468*, 2023.

[134] Marco Mancini, Guido Pagano, Giacomo Cappellini, Lorenzo Livi, Marie Rider, Jacopo Catani, Carlo Sias, Peter Zoller, Massimo Inguscio, Marcello Dalmonte, et al. Observation of chiral edge states with neutral fermions in synthetic hall ribbons. *Science*, 349(6255):1510–1513, 2015.

[135] Zheng Wang, Yidong Chong, John D Joannopoulos, and Marin Soljačić. Observation of unidirectional backscattering-immune topological electromagnetic states. *Nature*, 461(7265):772–775, 2009.

[136] Mark E Barber, Eric Yue Ma, and Zhi-Xun Shen. Microwave impedance microscopy and its application to quantum materials. *Nature Reviews Physics*, 4(1):61–74, 2022.

[137] Keji Lai, Worasom Kundhikanjana, Michael A Kelly, Zhi-Xun Shen, Javad Shabani, and Mansour Shayegan. Imaging of coulomb-driven quantum hall edge states. *Physical review letters*, 107(17):176809, 2011.

[138] Yong-Tao Cui, Bo Wen, Eric Y Ma, Georgi Diankov, Zheng Han, Francois Amet, Takashi Taniguchi, Kenji Watanabe, David Goldhaber-Gordon, Cory R Dean, et al. Unconventional correlation between quantum hall transport quantization and bulk state filling in gated graphene devices. *Physical Review Letters*, 117(18):186601, 2016.

[139] A Yacoby, HF Hess, TA Fulton, LN Pfeiffer, and KW West. Electrical imaging of the quantum hall state. *Solid state communications*, 111(1):1–13, 1999.

[140] ME Suddards, A Baumgartner, M Henini, and Christopher J Mellor. Scanning capacitance imaging of compressible and incompressible quantum hall effect edge strips. *New Journal of Physics*, 14(8):083015, 2012.

[141] Yanmeng Shi, Joshua Kahn, Ben Niu, Zaiyao Fei, Bosong Sun, Xinghan Cai, Brian A Francisco, Di Wu, Zhi-Xun Shen, Xiaodong Xu, et al. Imaging quantum spin hall edges in monolayer wte2. *Science advances*, 5(2):eaat8799, 2019.

[142] Monica Allen, Yongtao Cui, Eric Yue Ma, Masataka Mogi, Minoru Kawamura, Ion Cosma Fulga, David Goldhaber-Gordon, Yoshinori Tokura, and Zhi-Xun Shen. Visualization of an axion insulating state at the transition between 2 chiral quantum anomalous hall states. *Proceedings of the National Academy of Sciences*, 116(29):14511–14515, 2019.

[143] Zhengguang Lu, Tonghang Han, Yuxuan Yao, Aidan P Reddy, Jixiang Yang, Junseok Seo, Kenji Watanabe, Takashi Taniguchi, Liang Fu, and Long Ju. Fractional quantum anomalous hall effect in multilayer graphene. *Nature*, 626(8000):759–764, 2024.

[144] Aviram Uri, Sameer Grover, Yuan Cao, John A Crosse, Kousik Bagani, Daniel Rodan-Legrain, Yuri Myasoedov, Kenji Watanabe, Takashi Taniguchi, Pilkyung Moon, et al. Mapping the twist-angle disorder and landau levels in magic-angle graphene. *Nature*, 581(7806):47–52, 2020.

[145] Zhaodong Chu, Chun-Yuan Wang, Jiamin Quan, Chenhui Zhang, Chao Lei, Ali Han, Xuejian Ma, Hao-Ling Tang, Dishan Abeysinghe, Matthew Staab, et al. Unveiling defect-mediated carrier dynamics in monolayer semiconductors by spatiotemporal microwave imaging. *Proceedings of the National Academy of Sciences*, 117(25):13908–13913, 2020.

[146] Yong-Tao Cui, Eric Yue Ma, and Zhi-Xun Shen. Quartz tuning fork based microwave impedance microscopy. *Review of Scientific Instruments*, 87(6), 2016.

[147] Zhurun Ji, Mark E Barber, Ziyan Zhu, Carlos R Kometter, Jiachen Yu, Kenji Watanabe, Takashi Taniguchi, Mengkun Liu, Thomas P Devereaux, Ben Feldman, et al. Harnessing excitons at the nanoscale–photoelectrical platform for quantitative sensing and imaging. *arXiv preprint arXiv:2311.04211*, 2023.

[148] Taige Wang, Chen Wu, Masataka Mogi, Minoru Kawamura, Yoshinori Tokura, Zhi-Xun Shen, Yi-Zhuang You, and Monica T Allen. Probing the edge states of chern insulators using microwave impedance microscopy. *Physical Review B*, 108(23):235432, 2023.

[149] Dung-Hai Lee, Ziqiang Wang, and Steven Kivelson. Quantum percolation and plateau transitions in the quantum hall effect. *Physical review letters*, 70(26):4130, 1993.

[150] Xiao-Gang Wen. Theory of the edge states in fractional quantum hall effects. *International journal of modern physics B*, 6(10):1711–1762, 1992.

[151] U Zülicke, AH MacDonald, and MD Johnson. Observability of counterpropagating modes at fractional quantum hall edges. *Physical Review B*, 58(20):13778, 1998.

[152] Ron Sabo, Itamar Gurman, Amir Rosenblatt, Fabien Lafont, Daniel Banitt, Jinhong Park, Moty Heiblum, Yuval Gefen, Vladimir Umansky, and Diana Mahalu. Edge reconstruction in fractional quantum hall states. *Nature Physics*, 13(5):491–496, 2017.

[153] CL Kane, Matthew PA Fisher, and Joseph Polchinski. Randomness at the edge: Theory of quantum hall transport at filling $\nu = 2/3$. *Physical review letters*, 72(26):4129, 1994.

[154] Evgeny Redekop, Canxun Zhang, Heonjoon Park, Jiaqi Cai, Eric Anderson, Owen Sheekey,

Trevor Arp, Grigory Babikyan, Samuel Salters, and Kenji Watanabe. Direct magnetic imaging of fractional chern insulators in twisted mote2. *Nature*, 635(8039):584–589, 2024.

[155] Bivas Dutta, Wenmin Yang, Ron Melcer, Hemanta Kumar Kundu, Moty Heiblum, Vladimir Umansky, Yuval Oreg, Ady Stern, and David Mross. Distinguishing between non-abelian topological orders in a quantum hall system. *Science*, 375(6577):193–197, 2022.

[156] Trithep Devakul, Valentin Crépel, Yang Zhang, and Liang Fu. Magic in twisted transition metal dichalcogenide bilayers. *Nature communications*, 12(1):6730, 2021.

[157] Xiao-Wei Zhang, Chong Wang, Xiaoyu Liu, Yueyao Fan, Ting Cao, and Di Xiao. Polarization-driven band topology evolution in twisted mote2 and wse2. *Nature Communications*, 15(1):4223, 2024.

[158] Ning Mao, Cheng Xu, Jiangxu Li, Ting Bao, Peitao Liu, Yong Xu, Claudia Felser, Liang Fu, and Yang Zhang. Transfer learning relaxation, electronic structure and continuum model for twisted bilayer mote2. *Communications Physics*, 7(1):262, 2024.

[159] Taige Wang, Minxuan Wang, Woochang Kim, Steven G Louie, Liang Fu, and Michael P Zaletel. Topology, magnetism and charge order in twisted mote2 at higher integer hole fillings. *arXiv preprint arXiv:2312.12531*, 2023.

[160] Chong Wang, Xiao-Wei Zhang, Xiaoyu Liu, Jie Wang, Ting Cao, and Di Xiao. Higher landau-level analogues and signatures of non-abelian states in twisted bilayer mote2. *arXiv preprint arXiv:2404.05697*, 2024.

[161] Yang-Le Wu, B Andrei Bernevig, and Nicolas Regnault. Zoology of fractional chern insulators. *Physical Review B*, 85(7):075116, 2012.

[162] B Andrei Bernevig and N Regnault. Emergent many-body translational symmetries of abelian and non-abelian fractionally filled topological insulators. *Physical Review B*, 85(7):075128, 2012.

[163] Antoine Sterdyniak, Cecile Repellin, B Andrei Bernevig, and Nicolas Regnault. Series

of abelian and non-abelian states in c¿ 1 fractional chern insulators. *Physical Review B*, 87(20):205137, 2013.

[164] Zhao Liu, Emil J Bergholtz, and Eliot Kapit. Non-abelian fractional chern insulators from long-range interactions. *Physical Review B*, 88(20):205101, 2013.

[165] Ching Hua Lee, Ronny Thomale, and Xiao-Liang Qi. Pseudopotential formalism for fractional chern insulators. *Physical Review B*, 88(3):035101, 2013.

[166] Jörg Behrmann, Zhao Liu, and Emil J Bergholtz. Model fractional chern insulators. *Physical Review Letters*, 116(21):216802, 2016.

[167] Feng Chen, Wei-Wei Luo, Wei Zhu, and DN Sheng. Robust non-abelian even-denominator fractional chern insulator in twisted bilayer mote2. *arXiv preprint arXiv:2405.08386*, 2024.

[168] Hui Liu, Zhao Liu, and Emil J. Bergholtz. Non-abelian fractional chern insulators and competing states in flat moiré bands. *arXiv preprint arXiv:2405.08887*, 2024.

[169] Cheng Xu, Ning Mao, Tiansheng Zeng, and Yang Zhang. Multiple chern bands in twisted mote 2 and possible non-abelian states. *Physical Review Letters*, 134(6):066601, 2025.

[170] Kevin P Nuckolls, Myungchul Oh, Dillon Wong, Biao Lian, Kenji Watanabe, Takashi Taniguchi, B Andrei Bernevig, and Ali Yazdani. Strongly correlated chern insulators in magic-angle twisted bilayer graphene. *Nature*, 588(7839):610–615, 2020.

[171] Cheong-Eung Ahn, Wonjun Lee, Kunihiro Yananose, Youngwook Kim, and Gil Young Cho. Non-abelian fractional quantum anomalous hall states and first landau level physics in second moiré band of twisted bilayer mote2. *arXiv preprint arXiv:2403.19155*, 2024.

[172] Ya-Hui Zhang. Vortex spin liquid with fractional quantum spin hall effect in moiré chern bands. *Physical Review Letters*, 133(10):106502, 2024.

[173] Julian May-Mann, Ady Stern, and Trithep Devakul. Theory of half-integer fractional quantum spin hall insulator edges. *arXiv preprint arXiv:2403.03964*, 2024.

[174] Inti Sodemann Villadiego. Halperin states of particles and holes in ideal time reversal invariant pairs of chern bands and the fractional quantum spin hall effect in moiré mote2. *Physical Review B*, 110(4):045114, 2024.

[175] Chao-Ming Jian, Meng Cheng, and Cenke Xu. Minimal fractional topological insulator in half-filled conjugate moiré chern bands. *Physical Review X*, 15(2):021063, 2025.

[176] Kaifei Kang, Bowen Shen, Yichen Qiu, Yihang Zeng, Zhengchao Xia, Kenji Watanabe, Takashi Taniguchi, Jie Shan, and Kin Fai Mak. Evidence of the fractional quantum spin hall effect in moiré mote2. *Nature*, pages 1–5, 2024.

[177] Alexey Chernikov, Timothy C Berkelbach, Heather M Hill, Albert Rigosi, Yilei Li, Burak Aslan, David R Reichman, Mark S Hybertsen, and Tony F Heinz. Exciton binding energy and nonhydrogenic rydberg series in monolayer ws2. *Physical review letters*, 113(7):076802, 2014.

[178] Jainendra K Jain. *Composite fermions*. Cambridge University Press, 2007.

[179] Bertrand I Halperin and Jainendra K Jain. *Fractional quantum hall effects: new developments*. World Scientific, 2020.

[180] Yoon Jang Chung, KA Villegas Rosales, KW Baldwin, PT Madathil, KW West, M Shayegan, and LN Pfeiffer. Ultra-high-quality two-dimensional electron systems. *Nature Materials*, 20(5):632–637, 2021.

[181] Yiyu Xia, Zhongdong Han, Kenji Watanabe, Takashi Taniguchi, Jie Shan, and Kin Fai Mak. Superconductivity in twisted bilayer wse2. *Nature*, 637:833–838, 2024.

[182] Patrick Knüppel, Jiacheng Zhu, Yiyu Xia, Zhengchao Xia, Zhongdong Han, Yihang Zeng, Kenji Watanabe, Takashi Taniguchi, Jie Shan, and Kin Fai Mak. Correlated states controlled by a tunable van hove singularity in moiré wse2 bilayers. *Nature Communications*, 16(1):1959, 2025.

[183] Zhengguang Lu, Tonghang Han, Yuxuan Yao, Zach Hadjri, Jixiang Yang, Junseok Seo, Lihan

Shi, Shenyong Ye, Kenji Watanabe, and Takashi Taniguchi. Extended quantum anomalous hall states in graphene/hbn moiré superlattices. *Nature*, 637:1090–1095, 2025.

[184] Eric Anderson, Heonjoon Park, Kaijie Yang, Jiaqi Cai, Takashi Taniguchi, Kenji Watanabe, Liang Fu, Ting Cao, Di Xiao, and Xiaodong Xu. Magnetoelectric control of helical light emission in a moiré chern magnet. *arXiv preprint arXiv:2503.02810*, 2025.

[185] F Schulze-Wischeler, E Mariani, Frank Hohls, and Rolf J Haug. Direct measurement of the g factor of composite fermions. *Physical review letters*, 92(15):156401, 2004.

[186] Miguel Gonçalves, Juan Felipe Mendez-Valderrama, Jonah Herzog-Arbeitman, Jiabin Yu, Xiaodong Xu, Di Xiao, B Andrei Bernevig, and Nicolas Regnault. Spinless and spinful charge excitations in moiré fractional chern insulators. *arXiv preprint arXiv:2506.05330*, 2025.

[187] SM Girvin, AH MacDonald, and PM Platzman. Magneto-roton theory of collective excitations in the fractional quantum hall effect. *Physical Review B*, 33(4):2481, 1986.

[188] A Pinczuk, BS Dennis, LN Pfeiffer, and K West. Observation of collective excitations in the fractional quantum hall effect. *Physical review letters*, 70(25):3983, 1993.

[189] T Nakajima and H Aoki. Composite-fermion picture for the spin-wave excitation in the fractional quantum hall system. *Physical review letters*, 73(26):3568, 1994.

[190] Ady Stern and Bertrand I Halperin. Singularities in the fermi-liquid description of a partially filled landau level and the energy gaps of fractional quantum hall states. *Physical Review B*, 52(8):5890, 1995.

[191] Chetan Nayak and Frank Wilczek. Non-fermi liquid fixed point in 2+ 1 dimensions. *Nuclear Physics B*, 417(3):359–373, 1994.

[192] RH Morf, N d'Ambrumenil, and S Das Sarma. Excitation gaps in fractional quantum hall states: An exact diagonalization study. *Physical Review B*, 66(7):075408, 2002.

[193] GS Boebinger, HL Stormer, DC Tsui, AM Chang, JCM Hwang, AY Cho, CW Tu, and G Weimann. Activation energies and localization in the fractional quantum hall effect. *Physical Review B*, 36(15):7919, 1987.

[194] RL Willett, HL Stormer, DC Tsui, AC Gossard, and JH English. Quantitative experimental test for the theoretical gap energies in the fractional quantum hall effect. *Physical Review B*, 37(14):8476, 1988.

[195] RR Du, HL Stormer, DC Tsui, LN Pfeiffer, and KW West. Experimental evidence for new particles in the fractional quantum hall effect. *Physical review letters*, 70(19):2944, 1993.

[196] HC Manoharan, M Shayegan, and SJ Klepper. Signatures of a novel fermi liquid in a two-dimensional composite particle metal. *Physical review letters*, 73(24):3270, 1994.

[197] KA Villegas Rosales, PT Madathil, YJ Chung, LN Pfeiffer, KW West, KW Baldwin, and M Shayegan. Fractional quantum hall effect energy gaps: Role of electron layer thickness. *Physical review letters*, 127(5):056801, 2021.

[198] VJ Goldman, Bo Su, and JK Jain. Detection of composite fermions by magnetic focusing. *Physical review letters*, 72(13):2065, 1994.

[199] JH Smet, Dieter Weiss, RH Blick, G Lütjering, K Von Klitzing, R Fleischmann, R Ketzmerick, T Geisel, and G Weimann. Magnetic focusing of composite fermions through arrays of cavities. *Physical review letters*, 77(11):2272, 1996.

[200] Eric Anderson, Jiaqi Cai, Aidan P Reddy, Heonjoon Park, William Holtzmann, Kai Davis, Takashi Taniguchi, Kenji Watanabe, Tomasz Smolenski, and Ataç Imamoğlu. Trion sensing of a zero-field composite fermi liquid. *Nature*, 635(8039):590–595, 2024.

[201] A Yu Kitaev. Fault-tolerant quantum computation by anyons. *Annals of physics*, 303(1):2–30, 2003.

[202] SK Singh, C Wang, CT Tai, CS Calhoun, KA Villegas Rosales, PT Madathil, A Gupta, KW Baldwin, LN Pfeiffer, and M Shayegan. Topological phase transition between jain states and daughter states of the $\nu = 1/2$ fractional quantum hall state. *Nature Physics*, 20(8):1247–1252, 2024.

[203] Netanel H Lindner, Erez Berg, Gil Refael, and Ady Stern. Fractionalizing majorana fermions:

Non-abelian statistics on the edges¡? format?¿ of abelian quantum hall states. *Physical Review X*, 2(4):041002, 2012.

[204] Meng Cheng. Superconducting proximity effect on the edge of fractional topological insulators. *Physical Review B—Condensed Matter and Materials Physics*, 86(19):195126, 2012.

[205] David J Clarke, Jason Alicea, and Kirill Shtengel. Exotic non-abelian anyons from conventional fractional quantum hall states. *Nature communications*, 4(1):1348, 2013.

[206] Yanyu Jia, Tiancheng Song, Zhaoyi Joy Zheng, Guangming Cheng, Ayelet J Uzan, Guo Yu, Yue Tang, Connor J Pollak, Fang Yuan, Michael Onyszczak, et al. Anomalous superconductivity in twisted mote2 nanojunctions. *Science Advances*, 11(5):eadq5712, 2025.

[207] RB Laughlin. The relationship between high-temperature superconductivity and the fractional quantum hall effect. *Science*, 242(4878):525–533, 1988.

[208] RB Laughlin. Superconducting ground state of noninteracting particles obeying fractional statistics. *Physical review letters*, 60(25):2677, 1988.

[209] Fan Xu, Zheng Sun, Jiayi Li, Ce Zheng, Cheng Xu, Jingjing Gao, Tongtong Jia, Kenji Watanabe, Takashi Taniguchi, Bingbing Tong, et al. Signatures of unconventional superconductivity near reentrant and fractional quantum anomalous hall insulators. *arXiv preprint arXiv:2504.06972*, 2025.

[210] Tonghang Han, Zhengguang Lu, Zach Hadjri, Lihan Shi, Zhenghan Wu, Wei Xu, Yuxuan Yao, Armel A Cotten, Omid Sharifi Sedeh, Henok Weldeyesus, et al. Signatures of chiral superconductivity in rhombohedral graphene. *Nature*, pages 1–3, 2025.

VITA

Heonjoon Park grew up in Seoul, South Korea. He began his undergraduate studies at Seoul National University, majoring in Physics. During his undergraduate studies, he found himself interested in strongly-correlated quantum materials while working on spectroscopic techinques. He started research in the Xu group at the University of Washington at 2020. He received a Doctor of Philosophy in Physics following his work on strongly-correlated topological phases in moire materials.